# Investigating the Properties of Gamma Ray Bursts and Gravitational Wave Standard Sirens as High Redshift Distance Indicators

**Fiona Claire Speirits, M.Sci.**

# University *of* Glasgow

Presented for the degree of
Doctor of Philosophy
University of Glasgow
October 2008

This thesis is my own composition except where indicated in the text.

October 31, 2008

# Abstract

In a discipline commonly faulted for *ad hoc* assumptions and models with very little discriminating observational evidence, cosmologists are continually trying, and in many cases succeeding, to improve both the data and models. However, the desire to support currently favoured models often dominates research and may lead to a systematic bias being introduced in favour of a model before a strong body of supporting evidence has been accumulated. This is perhaps most evident in literature supporting the viability of Gamma Ray Bursts as cosmological distance indicators, where aside from subjective data-selection, the basic statistical methods are at best questionable and at worst incorrect.

To this end, we construct a simple cosmology-independent illustration of the effect that the application of these methods has on parameter estimation and discuss the correct method to apply to current data. We also investigate the constraints potential future Gamma Ray Burst data may place on alternatives to the status quo Concordance Model in the shape of Conformal Gravity and Unified Dark Matter through a widely applicable and transferable Bayesian model comparison technique and the development of a representative mock data set.

Finally, we investigate gravitational wave standard sirens as an alternative high-redshift distance indicator. We first illustrate their strong diagnostic potential through a Bayesian model comparison between the standard Unified Dark Matter model and a variant in which the dark component is redshift dependent. By drawing mock data from a known cosmological model, thus fixing the expected values of the model parameters, we find that while 182 Type 1a Supernovae are readily confused between constant and evolving models, just 2 standard sirens are able to successfully identify the correct model.

Having established standard sirens as an effective tool in cosmological model

comparison, we then address the potential confusion of models with dynamical dark energy and intrinsic curvature. We show that currently used distance indicators – Type 1a Supernovae, Baryon Acoustic Oscillations and the Cosmic Microwave Background Radiation – are not reliable enough to identify a small amount of intrinsic curvature, which partly justifies the common practice of assuming flat space in order to reduce the number of free parameters. However, we show that the addition of even a small number of standard sirens greatly reduces this problem. The addition of just two sirens offers a slight improvement, while adding ten sirens to the aforementioned list of indicators halves the range over which there is uncertainty between models.

# Thank you. . .

. . . to everyone I have ever asked for help or advice – mainly the members (past and present) of the Astronomy & Astrophysics Research Group and associated hangers-on. Someone always knew the answer eventually (and it was usually Daphne).

Many people have put up with my ranting and rambling, very little of it remotely work related or even nearly interesting. Mum, Dad, Iain, Euan, Jen, Lynne, Cat, Craig, Gav, Susan and Mike – thanks for at least pretending to listen some of the time.

Lastly, my supervisor Martin Hendry deserves a big chunk of my appreciation. I'm very aware and grateful of the autonomy I've been given over the past three years, and I know from experience that not all research students are this fortunate. Thank you for all your help and advice.

"Space is big – really big – you just won't believe how vastly, hugely, mind-bogglingly big it is."

Douglas Adams [1]

"At 2.27pm on February 13th of the year 2001, the Universe suffered a crisis in self-confidence. Should it go on expanding indefinitely? What was the point?"

Kurt Vonnegut [2]

# Summary

Cosmologists may have accepted Douglas Adams' claim but that hasn't stopped them from attempting to measure it. This task is made all the harder by the Universe's refusal to lead a static existence and the inconvenience of a cosmic speed limit, even if that happens to be rather fast by an average cosmologist's standards. We must therefore rely on ingenious methods to ascertain the spatial and temporal evolution of the Universe, the most common of which is the standard candle – an 'intergalactic lighthouse' of known intrinsic brightness. Current examples of such standard candles include Cepheid variable stars and Type 1a Supernovae. However, these important distance indicators can only be detected relatively nearby; in order to extend our knowledge of the shape and evolution of the Universe it is essential to probe at much larger distances. In this thesis we conduct an appraisal of two potential solutions to this problem – Gamma Ray Bursts and gravitational wave standard sirens. However, before we can understand how to measure the Universe, we must first be able to describe it. To this end, Chapter 1 outlines the basis of modern Cosmology: the theories, assumptions and parameters that are used to describe the evolution of the Universe on large scales. In addition to introducing the current concordance model $\Lambda$CDM, two alternatives are presented in the form of Conformal Gravity and Unified Dark Matter. These models will be used to investigate the diagnostic abilities of Gamma Ray Bursts and standard sirens, but the models themselves are of no particular import (notwithstanding the specific physical motivations for their introduction) and could equally be replaced by any model of interest.

Chapter 2 goes on to describe some of the many astrophysical phenomena employed by cosmologists to get a handle on the 'mind-bogglingly big' distances involved. These include both well-established distance indicators such as Type

1a Supernovae and the Cosmic Microwave Background Radiation (CMBR) along with emerging candidates that include Baryon Acoustic Oscillations (BAO) and the main focus of this thesis: gravitational wave standard sirens and Gamma Ray Bursts (GRB). In Chapter 3 we construct a simple cosmology-independent model to illustrate calibration issues surrounding current attempts to utilise GRBs as distance indicators, and highlight their current inefficacy in constraining cosmological models. Chapter 4 continues this work by challenging attempts in the recent cosmology literature to apply Bayesian statistical techniques to GRB data analysis as one must account for the current cosmology dependency of observational errors. Furthermore, we show that attempts to extend this already incorrect method lead to artificially tight confidence regions around incorrectly identified best-fit parameter values when in reality no more information can be extracted from the data. In recognition of the impressive rate of progress in both the volume and accuracy of data obtained from current and projected missions, we also consider what GRBs may be able to tell us about the Universe, should we be able to solve the calibration issues currently present in the data – a task that may be aided by detection of sufficiently *low*-redshift events. We demonstrate the power that accurate high redshift events will have in order to enhance our ability to discriminate between cosmological models.

Continuing in this vein of future projection, in Chapter 5 we consider what gravitational wave standard sirens may be able to tell us about our Universe. We show that an impressively small number of these sources can place highly precise and accurate constraints on parameter values. Moreover, through Bayesian model comparison we demonstrate that sirens could play an important role in discriminating between models with dynamical dark energy and non-zero curvature. Finally, Chapter 6 provides a discussion of the results presented herein and outlines the scope for continuing the analysis begun in this thesis.

# Contents

# Chapter 1

# Cosmology in a Nutshell

In the days of a geocentric Solar System (perhaps a misnomer in that case) a cosmologist's role would have been restricted to studies of the planets and their motion with respect to the 'fixed' stars. In our slightly more enlightened epoch however, there is significantly wider scope for investigation, with every new discovery presenting even more puzzles to be solved. The challenge now is to discover a single model that governs the entire evolution of the Universe from the initial (formally) infinitely dense singularity to the cooling, expanding speckling of galaxies we observe in the current epoch. While this has not yet been achieved, there does exist a strong mathematical foundation to modern cosmology and in this chapter we introduce the basic theory upon which our subsequent research relies.

## 1.1   The Expanding Universe

Einstein's General Theory of Relativity (GR), developed over several years and published fully in 1916, forms a significant part of the theoretical foundation for modern Cosmology. While the prevailing idea was of a static, infinite Universe, GR provided the mathematical framework and physical motivation for an alternative vision: one in which the Universe is dynamic. The subsequent observations of galaxies receding from our own, published by Edwin Hubble in 1929, were evidence of the viability of this paradigm shift. Although the intricacies of GR are beyond the scope of this thesis, it is necessary to provide a brief overview of the GR foundations on which modern cosmology is built.

## 1.1.1 Einstein's Field Equations

The simple elegance of GR lies in the coordinate-independent nature of its construction. As the laws of physics must hold in any reference frame, they must be invariant under transformations between coordinate systems. Therefore, an interval in spacetime measured by one observer must be the same as when measured by a different observer i.e. the interval is invariant. Invariants are constructed from a set of basis coordinates and a metric, which transforms coordinate distance on a smooth manifold into a physical distance in spacetime. The invariant distance can be written as

$$\mathrm{d}s^2 = g_{\mu\nu}\mathrm{d}x^\mu\mathrm{d}x^\nu, \qquad (1.1)$$

where the repeated indices are summed over as many dimensions as required and the metric $g_{\mu\nu}$ is an $n \times n$ matrix that transforms the vector coordinate distances into a scalar physical distance. For example, the 4-dimensional flat Minkowski spacetime of Special Relativity has coordinates $(\mathrm{d}x^\mu, \mathrm{d}x^\nu) = (\mathrm{d}t, \mathrm{d}x, \mathrm{d}y, \mathrm{d}z)$ and metric $g_{\mu\nu} = \eta_{\mu\nu} = \mathrm{diag}(-1, 1, 1, 1)$.

Equation (1.1) is true for any coordinate system and the corresponding metric. In addition to this, a straight line on a manifold – a *geodesic* – is the shortest path between two points. Einstein then applied these mathematical concepts that hold for any manifold to *our* Universe: the manifold is our 4-dimensional spacetime with a metric encoding its shape; a geodesic is the path a free-falling particle will follow on this manifold unless acted upon by a force. General Relativity then links the contents of the manifold to its shape through the Einstein field equations:

$$G^{\mu\nu} + \Lambda g^{\mu\nu} = 8\pi T^{\mu\nu}, \qquad (1.2)$$

where $G^{\mu\nu}$ is the Einstein tensor, which incorporates the metric $g^{\mu\nu}$ for our spacetime, $T^{\mu\nu}$ is the stress-energy tensor and $\Lambda$ is a scalar constant[1]. In physical terms, the coupled differential field equations represented by Equation (1.2) state that gravity is simply a result of the curvature of spacetime caused by the matter and energy contained within. However, while the interpretation is straightforward to understand, finding a solution is very difficult except under certain simplifying

---

[1] We shall examine the role of this constant in §1.2.2.

assumptions, for example vacuum solutions such as $T^{\mu\nu} = 0$ describe a region with no matter or nongravitational fields present. The myriad solutions to these equations each describe unique universes; the trick is to find the solution that best describes what we can see in our own Universe.

## 1.1.2 Friedmann's Equations

One such solution follows from adopting the physical assumption of the Cosmological Principle, which states that the expanding Universe, on large scales, is statistically *homogeneous* and *isotropic*. As illustrated in Figure 1.1, homogeneity implies that the Universe looks the same to any observer regardless of their position, while isotropy states that you would expect to see the same traits looking in any direction. Local, small-scale structure – planetary systems, galaxies, clusters – are simply small perturbations on a uniform sheet. It is the antithesis to the geocentric Ptolemaic model: there is nothing special about *any* place in the Universe, least of all the patch of spacetime the Milky Way occupies. The Universe is then treated as a perfect fluid, which implies it can be characterised completely by its energy density $\rho$ and isotropic pressure $p$ and the stress-energy tensor in Equation (1.2) becomes

$$T^{\mu\nu} = (\rho + p)u^{\mu}u^{\nu} + pg^{\mu\nu}, \tag{1.3}$$

where **u** is the four-velocity of the fluid element and $g^{\mu\nu}$ is the metric tensor for a general curved spacetime.
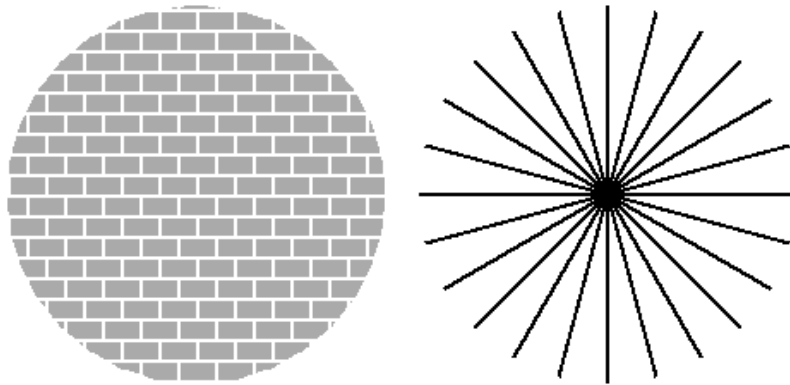


Figure 1.1: An observer within these Universes would see them as homogeneous (left) or isotropic (right) [3].

The most general fluid solution governing the expansion of spacetime under these constraints is then given by the Friedmann-Lemaître-Robertson-Walker (FLRW) metric

$$\mathrm{d}s^2 = -\mathrm{d}t^2 + R^2(t)\left[\frac{\mathrm{d}r^2}{1-kr^2} + r^2\mathrm{d}\Omega^2\right], \tag{1.4}$$

where the invariant 4-dimensional distance $\mathrm{d}s^2$ is a function of the coordinate time interval $\mathrm{d}t^2$ and the time-dependent spatial interval $\mathrm{d}l^2 = R^2(t)\left[\frac{\mathrm{d}r^2}{1-kr^2} + r^2\mathrm{d}\Omega^2\right]$. The curvature constant $k$ can be scaled to take the values $k = \{-1, 0, 1\}$ and describes the geometry of the spacetime manifold and the trajectory of a geodesic traveller: the Universe is open $k = -1$, flat $k = 0$ or closed $k = 1$. As there is no mandatory coordinate system within which to define these distances, the natural choice of *comoving coordinates* can be adopted. In this system, constant coordinate values are assigned to observers moving with the expanding background universe. These observers then see the Universe expanding isotropically around them as they have no peculiar velocity with respect to the background. The scale factor $R(t)$, with current value $R_0$, then relates comoving coordinates to physical coordinates as $r = R(t)s$ where $r$ is the proper distance and $s$ is the comoving distance. Solving the FLRW metric (1.4) and the Einstein field equations (1.2) yields the Friedmann Equations

$$H^2 \equiv \left(\frac{\dot{R}}{R}\right)^2 = \frac{8\pi G\rho}{3} + \frac{\Lambda c^2}{3} - \frac{kc^2}{r^2}, \tag{1.5}$$

$$\frac{\ddot{R}}{R} = -\frac{4\pi G}{3}\left(\rho + \frac{3p}{c^2}\right) + \frac{\Lambda c^2}{3}, \tag{1.6}$$

where $\rho$ and $p$ are the energy density and isotropic pressure and $G$ is the Gravitational constant. $H$ is historically the constant of proportionality in Hubble's empirical formula $v = Hr$ relating the recession velocity $v$ of a galaxy to the proper distance $r$ and as such is related to the proper time derivative of the scale factor $\dot{R}$ as $H = \frac{\dot{R}}{R}$.

The scalar parameter $\Lambda$ can be interpreted as accounting for the contribution of the zero-point energy of the vacuum to the dynamical evolution of the Universe and $k$ is the curvature constant as before. Conventionally, the light speed $c$ is taken to be unity and this will be employed henceforth. Equations (1.5) and (1.6) then fully describe the time evolution and geometry of a universe consisting

of matter with a specified equation of state, characterised by the dimensionless
parameter

$$w = \frac{p}{\rho}. \tag{1.7}$$

Intuitive candidates for this matter include pressureless ($p = 0$) non-relativistic
matter with $w = 0$ and radiation-dominated matter, for which $w = \frac{1}{3}$. The matter
density will evolve over time along with the normalised scale factor $a(t) = \frac{R(t)}{R_0}$
(thus $a_0 = 1$) as $\rho \propto a^{-3(w+1)}$; hence for pressureless matter $\rho \propto a^{-3}$ and for
radiation-dominated matter $\rho \propto a^{-4}$.

However, although the theory of how $a$ universe subject to these simplifying
assumptions will behave over time has been well established, the task for modern
cosmology is to work out how to describe (and perhaps at some point explain)
the Universe as we see it today and as we look back through its history with
ever deeper observations. Many models exist that fit the observations to varying
degrees and no model can yet answer everything. However, in the last decade
several similar models have emerged as potential candidates, the most prominent
of which (due to its simplicity and the wide range of observational evidence that
appears to corroborate it) is ΛCDM.

## 1.2   Concordance Cosmology – ΛCDM

Current observations of the Universe, including large-scale galaxy and supernova
surveys, have enabled the visible matter distribution of the Universe to be estab-
lished more accurately than ever before, as can been seen in Figure 1.2. However,
visible baryonic matter only makes up part of the total energy density of the
Universe. Λ-Cold Dark Matter (ΛCDM) attempts to explain the remainder of
this energy budget and reconcile observational evidence with the models.

### 1.2.1   Observational Evidence

Everyone is familiar with the Big Bang model but observational cosmology is not
concerned with how or indeed why a spacetime singularity decided to spew forth
the Universe. Generally (although by no means exclusively) cosmologists concern
themselves with what happened just after the Planck time up to the present epoch
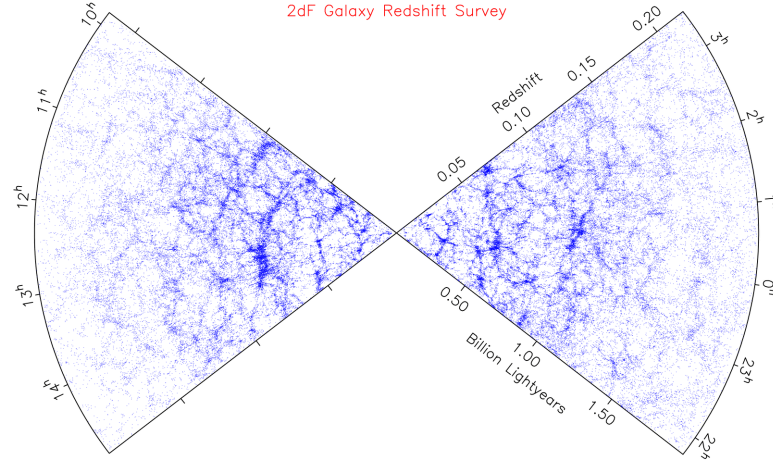
Figure 1.2: The 2dF Galaxy Redshift Survey, showing the redshift position of almost 250,000 galaxies [4].

and let the theoretical quantum physicists worry about the singularity. Aside from the theoretical issues, observations are currently limited by technology and there is a finite observable universe from which to obtain information. In addition to that, until gravitational waves are detected, observations are mainly restricted to electromagnetic (EM) radiation. Direct information can only be obtained for matter that interacts with photons, resulting in the need to infer rather than measure the presence of another type of matter.

There are several key observations that suggest the existence of more exotic matter and energy:

- Galaxy cluster dynamics cannot be accounted for by the mass of visible matter alone [5]

- Galactic rotation curves are flat out to large radii, indicating a large mass-to-light ratio [6]

- Simulations of large scale structure formation including only visible matter cannot replicate the universe observed today [7]

- High-redshift supernovae observations suggest the expansion of the Universe is accelerating, which is counter-intuitive to the concept of a decelerating universe that would originate from an initial hot big bang [8]

For any proposed model to be considered a success, it must therefore address these issues.

## 1.2.2   ΛCDM Parameters

All cosmological models contain a varying number of parameters that are evaluated based on observational data and then further constrained as more data becomes available. In the context of the first Friedmann Equation (1.5), the rate of expansion of the Universe $H$ is currently dependent on three contributions

$$H^2 \equiv \left(\frac{\dot{R}}{R}\right)^2 = \underbrace{\frac{8\pi G\rho}{3}}_{\substack{matter+\\radiation}} + \underbrace{\frac{\Lambda}{3}}_{\substack{vacuum\\energy}} - \underbrace{\frac{k}{r^2}}_{curvature} \ .$$

Recasting in a dimensionless form (adhering to the convention that $c = 1$)

$$\frac{8\pi G\rho}{3H^2} + \frac{\Lambda}{3H^2} + \frac{k}{r^2 H^2} = 1, \tag{1.8}$$

we can then express the left hand side as three dimensionless parameters

$$\Omega_m + \Omega_\Lambda + \Omega_k = 1. \tag{1.9}$$

This equation holds for all times in a matter dominated universe and the relative dominance of each of these constituents has an influence on the structure and subsequent evolution of the Universe. Assuming mass conservation $\rho R^3 = \rho_0 R_0^3$, the value of $H$ at any epoch (i.e. any specified value of scale factor $R$) can be related to the current value $H_0$ at $R = R_0$

$$\frac{H^2}{H_0^2} = \frac{8\pi G\rho_0}{3H_0^2}\left(\frac{R_0}{R}\right)^3 + \frac{\Lambda}{3H_0^2} - \frac{k}{R^2 H_0^2}\frac{R_0^2}{R_0^2}, \tag{1.10}$$

and thus in turn to the current values of the density parameters

$$\frac{H^2}{H_0^2} = \Omega_{m_0}\left(\frac{R_0}{R}\right)^3 + \Omega_{\Lambda_0} + \Omega_{k_0}\left(\frac{R_0}{R}\right)^2. \tag{1.11}$$

Conventionally, cosmologists avoid dealing with absolute values of the scale factor by assigning a redshift $z$ to events, based on the frequency shift between when a photon was emitted and when it is observed due to the cosmic expansion

$$\frac{\nu_{emit}}{\nu_{obs}} \equiv 1 + z. \tag{1.12}$$

As the recession velocity is directly dependent on the scale factor at the time of emission and observation

$$\frac{\nu_{emit}}{\nu_{obs}} \equiv 1 + z = \frac{R(t_{obs})}{R(t_{emit})}, \tag{1.13}$$

we can therefore express the Hubble parameter as a function of redshift – a directly measurable quantity – and Equation (1.11) becomes

$$H(z) = H_0 E(z), \qquad (1.14)$$

where

$$E(z) = \left[\Omega_{m_0}(1 + z)^3 + \Omega_{\Lambda_0} + \Omega_{k_0}(1 + z)^2\right]^{\frac{1}{2}}. \qquad (1.15)$$

The matter density $\Omega_m$ is comprised of contributions from both baryonic and non-baryonic matter. Baryonic matter can interact electromagnetically and consists of all visible matter in the Universe. Contrastingly, non-baryonic matter only interacts gravitationally, hence the moniker 'Dark Matter', and the presence of this exotic matter has not been directly detected, although gravitational lensing of distant galaxies has allowed intervening clumps of dark matter to be reconstructed [9]. The existence of non-luminous matter has been postulated to address the key observations introduced in §1.2.1 regarding galaxy dynamics and large-scale structure formation. It is necessary that this dark matter is 'cold' (i.e. non-relativistic) in order to allow matter-clumping on small scales, something that relativistic 'hot' dark matter would preclude. However, while the gravitational attraction of matter would intuitively slow down the Universal expansion rate, recent data have in fact suggested that it is currently accelerating [8], while at some time in the past it has been decelerating [10].

This cosmic jerk arises when the influence of the matter density $\Omega_m$ in the ever-expanding Universe becomes over-powered by the vacuum energy density $\Omega_\Lambda$ and the rate of expansion changes from decelerating to accelerating. It can be seen from Equation (1.15) that at high redshift $\Omega_m(1 + z)^3$ will dominate the expansion rate, in contrast to the non-redshift dependent $\Omega_\Lambda$. Perhaps in keeping with the Dark Matter nomenclature, this ethereal mechanism driving the cosmic expansion is referred to as 'Dark Energy'. The equation of state of dark energy is the source of much debate. Within ΛCDM, $w_\Lambda \sim \mathcal{O}(-1)$ and is $\Lambda$ is referred to as the Cosmological Constant [10], [11]. There exist many models that consider this option, each with their own parameterisation for Equation (1.15), examples of which are discussed in §1.3.2 and §5.3.

The final contribution to Equation 1.15 comes from the intrinsic curvature of the Universe. Current analysis of the cosmic microwave background radiation (CMBR) and baryon acoustic oscillations (BAO) has placed tight constraints on the curvature parameter, with $\Omega_k = -0.003 \pm 0.010$ [12], [13]. Indeed, the proximity of the curvature constant to zero, together with the strong theoretical motivation for this value, has resulted in the assumption of a flat $\Omega_k = 0$ universe in a significant proportion of the analysis found in current literature. This potential issue is addressed further in §5.3.

See reference in caption for image.

Figure 1.3: Mock galaxy redshift surveys generated for $(\Omega_m, \Omega_\Lambda) = (1, 0)$ (top) and $(\Omega_m, \Omega_\Lambda) = (0.3, 0.7)$ (bottom) [14]. The galaxy distribution is markedly different for varying parameter values, with the large-scale structure visibly 'smeared out' in the simulation with $\Omega_\Lambda = 0$.

Recently published constraints on ΛCDM parameters evaluated from the five-year Wmap data [15] on the CMBR along with BAO and Supernovae data give the baryonic matter density $\Omega_b = 0.0456 \pm 0.0015$, the dark matter density $\Omega_{DM} = 0.228 \pm 0.013$ and the dark energy density $\Omega_\Lambda = 0.726 \pm 0.015$ [16]. Mock galaxy redshift surveys can be simulated under these and many other conditions and Figure 1.3 shows the obvious disparity between universes with varying

contributions from the matter and energy densities. Simulations can be readily compared with the structures seen in real redshift surveys, such as Figure 1.2, in order to precisely constrain the parameters of the cosmological model adopted in generating the simulation data [17].

### 1.2.3 Criticisms of ΛCDM

ΛCDM suffers from being an empirical model. In contrast to mathematical theories, such as GR, it cannot make predictions and seeks only to describe what is observed. It has been accused of consisting of "epicycles on epicycles", analogous to the pre-Kepler universes that required more and more complicated planetary motions to agree with each new observation. Supporters of alternative theories suggest that it should not be necessary to invoke mysterious forms of matter and energy, for which there is no direct evidence, in order to reconcile ΛCDM with observations. Indeed, it does not sit well with most cosmologists that only 4% of the Universe, in the form of baryonic matter, is directly detectable and even partly understood.

In addition to the current gap in knowledge corresponding to 96% of the Universe, measurements of the Cosmic Microwave Background Radiation (CMBR) suggest that the Universe is very nearly flat, with $\Omega_k \simeq 0$. In order to produce a current day value of $\Omega_{k_0} \simeq 0$, the initial conditions of the primordial universe must be fine tuned such that $\Omega_k = 0$ to very high precision. One way to explain this is to assume $\Omega_k = 0$ at all times. Otherwise, any initial deviation from this condition that the Universe was exactly flat would have grown in time as the decelerating Universe expanded. This 'flatness problem' has still not been satisfactorily addressed by ΛCDM. A period of exponential, 'inflationary' expansion is commonly accepted as a potential solution to this problem, as it would 'smooth out' any initial perturbations, thus removing the necessary finely tuned $\Omega_k = 0$ initial condition.

Perhaps the greatest criticism of the concordance model is its inability to provide a physical justification for fine tuning $|\Lambda|$ by $\sim 60$ orders of magnitude from the large expectation value provided by particle physics [18] to a value that allows $\Omega_\Lambda$ to be of the order of 1, as is suggested by current supernovae observations [8].

Particle physicists associate $\Omega_\Lambda$ with the energy-momentum density of a virtual particle's lowest energy (vacuum) state and the cumulative gravitational effect of the virtual particles required by Heisenberg's uncertainty principle results in the vacuum having an energy density $\rho_{vac}$. While there is currently no calculated predicted value for $\rho_{vac}$, theoretical limits suggest estimates that are $\sim 10^{60}$ times larger than suggested by astronomical observations. Until either cosmologists can convincingly measure $\Omega_\Lambda$ and more importantly *explain* its source, or particle physicists prove that $\Lambda$ must be exactly zero, the cosmological constant problem will continue to blight any model that invokes its existence. A more thorough discussion can be found in [18].

As these issues have not yet been (and perhaps cannot be) solved by $\Lambda$CDM, it is therefore of interest to consider what GRBs and standard sirens may have to contribute to this debate by examining some alternative options to the concordance model.

## 1.3   Some Alternative Cosmologies

While $\Lambda$CDM may be peddled as the simplest and most likely model describing the Universe, there exists a plethora of alternatives. Some of these predict aspects of the Universe that are (at least for now) untestable and therefore are uninstructive within a thesis that aims to apply potentially new distance indicators to viable cosmological models. The models subsequently presented have been selected due to their similarity to $\Lambda$CDM at low redshift but measurable differences beyond the limit of current distance indicators. This direct comparison will highlight the importance of developing more accurate and higher redshift indicators while avoiding the need to probe the construction of the models at a theoretically technical level[2].

### 1.3.1   Conformal Gravity

In a manner similar to Modified Newtonian Dynamics (MOND) theories, Conformal Gravity [19] suggests that the attractive nature of gravity as we experience it

---

[2]In other words, they are easily implemented without requiring an expert level of theoretical understanding.

day to day is only the low energy limit of a more complex force that is *repulsive* at cosmological distances [20], with the positive gravitational constant $G$ from Equation (1.5) being replaced with a negative coupling constant $G_{\text{eff}}$ where

$$G_{\text{eff}} = -3c^3/4\pi\hbar S_0^2. \tag{1.16}$$

$|G_{\text{eff}}|$ in conformal gravity is small as it is dependent on the very large expectation value $S_0$ of the scalar field that is required to break the conformal symmetry cosmologically [19]. In addition to this, the theory suggests that the fine tuning problem discussed in §1.2.3 is avoided; under conformal gravity $\Lambda$ originates from the phase transitions of elementary particles from an unbroken symmetry phase with $\Lambda = 0$ to a lower energy phase with broken symmetry. $\Lambda$ is therefore *negative* at all epochs and as $G_{\text{eff}}$ is also negative, $\Omega_\Lambda$ is necessarily positive

$$\Omega_\Lambda = \frac{8\pi G_{\text{eff}}\Lambda}{H^2(t)}. \tag{1.17}$$

A problematic large $|\Lambda|$ is then controlled by coupling to a small $|G_{\text{eff}}|$. The deceleration parameter in conformal gravity

$$q(t) = \frac{\Omega_m}{2} - \Omega_\Lambda \tag{1.18}$$

is also negative for all $t$ as a negative $G_{\text{eff}}$ results in $\Omega_m < 0$. Therefore, a universe governed by conformal gravity is accelerating *at all epochs*. This then removes the need to explain why a decelerating expansion rate would suddenly decide to flip and start accelerating, as is the case under $\Lambda$CDM.

Equation (1.15) dictates how the evolution of a universe over time – quantified by the Hubble parameter – is dependent on the constituent matter densities within the construct of $\Lambda$CDM. However, that equation was simply the $\Lambda$CDM-specific version of the more general case

$$E(z) = \left[\sum_i^n \Omega_i(1+z)^{3+3w_i}\right]^{1/2}, \quad \sum_i^n \Omega_i = 1, \tag{1.19}$$

where $\Omega_i$ are the values at any era determined by $z$. As outlined in §1.1.2, $w$ is the equation of state parameter and within the $\Lambda$CDM model takes the values $w_m = 0$, $w_\Lambda = -1$ and $w_k = -1/3$. The coordinate distance at redshift $z$ is then given by

$$R_0 r = \frac{c}{H_0} \int_0^z \frac{\mathrm{d}z}{E(z)}. \tag{1.20}$$

However, in conformal gravity this quantity can be shown to be dependent only on the current values of $H_0$ and the deceleration parameter $q_0$ [19]

$$R_0 r = -\frac{c(1+z)}{H_0 q_0} \left[ 1 - \left( 1 + q_0 - \frac{q_0}{(1+z)^2} \right)^{1/2} \right].$$ (1.21)

It is therefore possible to probe all epochs of a conformal universe knowing only the present day value of the single model parameter $q_0$.

Conformal gravity predicts that the universe has always been expanding at an ever increasing rate. This contrasts with the suggestion of $\Lambda$CDM that the expansion rate had been slowing down since the Big Bang, only to then start accelerating again in the low-redshift universe. This distinct difference makes conformal gravity an ideal theory to test with high redshift distance indicators. In addition to this, it also provides a simple method to probe the diagnostic power of potential indicators by investigating the constraints they can place on the value of $q_0$. We will carry out such an investigation in Chapter 3.

## 1.3.2   Unified Dark Matter

Alternative theories of gravity are one tactic employed by those seeking a more complete description of the Universe. However, models also exist that are still based on GR but the dynamics have an alternative parameterisation, with different components contributing to the overall density of the Universe. One such model suggests that the two dark components in $\Lambda$CDM are in fact two parts of a single component; within this unified dark matter (UDM) model [21], Equation (1.5) becomes

$$H^2 = \frac{8\pi G}{3} \left( \rho_r + \rho_b + \rho_X \right),$$ (1.22)

where $\rho_{r,b}$ are the standard radiation and baryon energy densities and $\rho_X$ is the energy density of the single dark component. This component is made up of a constant part $\rho_\Lambda$, which plays a similar role to the cosmological constant in $\Lambda$CDM, and an evolving part $\rho_m$ such that the present day value $\rho_{X_0} = \rho_{m_0} + \rho_\Lambda$.

In a bid to avoid an *ad hoc* 'cosmological constant' in this model, the observed accelerating expansion rate of the Universe must be allowed for by some justifiable mechanism. A period of acceleration cannot be fit by baryonic matter alone as

the strong energy condition must be violated i.e. $P_X < -\rho_X/3$. This cannot be achieved by 'normal matter' [22]. A constant, time-independent $w_X$ for a dark component with equation of state $P_X = P_X(\rho_X)$ would satisfy this, as in the case of $\Lambda$CDM. However, this would result in the adiabatic speed of sound in a UDM universe $c_s^2 = \mathrm{d}P_X/\mathrm{d}\rho_X < 0$. Instead, a constant sound speed is assumed such that $\mathrm{d}P_X/\mathrm{d}\rho_X \simeq \alpha$ and the equation of state is then

$$P_X \simeq p_0 + \alpha\rho_X. \tag{1.23}$$

In sofar as one may regard Equation (1.23) as a Taylor expansion to $\mathcal{O}(2)$ of any barotropic equation of state about the current energy density value $\rho_{X_0}$, it is a valid low redshift parameterisation of any dark component. However, UDM assumes that Equation (1.23) is not an approximation and holds at any time and redshift.

The fluid must satisfy the stress conservation equation

$$\dot{\rho}_X = -3H(\rho_X + P_X). \tag{1.24}$$

Therefore, if there exists an energy density $\rho_X = \rho_\Lambda$ where $P_X(\rho_\Lambda) = \rho_\Lambda$ then $\rho_\Lambda$ fulfils the required role of a cosmological constant with $w_\Lambda = -1$ and $\dot{\rho}_\Lambda = 0$. Combining Equations (1.23) and (1.24) under these requirements then yields the evolution with redshift of the unified dark matter density

$$\rho_X(z) = \rho_\Lambda + (\rho_{X_0} - \rho_\Lambda)(1 + z)^{-3(1+\alpha)}, \tag{1.25}$$

with the contribution of the constant $\rho_\Lambda$ and the evolving $\rho_m$ with present value $\rho_{m_0} = \rho_{X_0} - \rho_\Lambda$. From Equation (1.22), the UDM analogue of Equation (1.14) is

$$H(z) = H_0 \left[ \Omega_b(1 + z)^3 + \Omega_\Lambda + (1 - \Omega_\Lambda)(1 + z)^{3(1+\alpha)} \right]^{1/2}. \tag{1.26}$$

The equation of state for this model $w_X = P_X/\rho_X$ is then

$$w_X = -(1 + \alpha)\frac{\rho_\Lambda}{\rho_X} + \alpha. \tag{1.27}$$

In contrast to $w_{\Lambda\text{CDM}}$, $w_X$ is therefore not constant as $\rho_X$ evolves in time.

There are many other parameterisations for an equation of state that evolves in time and we will discuss this issue further in §5.3.

# Chapter 2

# Distance Indicators and Statistical Methods in Cosmology

It is essential to ascertain accurate distances in cosmology. Aside from establishing the physical size of galaxies, clusters and ultimately the Universe as a whole, the parameters of the underlying cosmology can be probed by examining where (and when) sources are measured to be, compared to where a cosmological model suggests they should be. However, measuring distances on cosmological scales is not straightforward and requires a large amount of ingenuity.

## 2.1 The Cosmological Distance Ladder

In order to pinpoint the distance to remote astronomical sources, the cosmological distance ladder consists of physically measurable distances and calibrated distances relying on classes of objects that are believed to be homogeneous across the population. However, in an expanding universe it is important to first define 'distance'.

### 2.1.1 Proper Distance and Luminosity Distance

The distance modulus $\mu$ is commonly used to relate the flux released by a source and what is detected a fixed distance $d$ [Mpc] away, with the fluxes quantified by the absolute $M$ and apparent magnitude $m$, respectively

$$\mu \equiv m - M = 5 \log_{10} d + 25. \tag{2.1}$$

While this relation would appear in any beginners guide to Astronomy, measuring the quantity $d$ becomes difficult over cosmological distances.

The *proper* distance – what we would measure if we had a long enough ruler and fast enough spaceship – is given by

$$d_p = R_0 \int_0^r \frac{\mathrm{d}r}{\sqrt{1 - kr^2}}, \tag{2.2}$$

where $r$ is the comoving radius. The proper distance therefore depends on the curvature of the Universe – $k$ – hence

$$d_p = \begin{cases} r & \text{for } k = 0 \\ \sinh^{-1} r & \text{for } k = -1 \\ \sin^{-1} r & \text{for } k = +1 \end{cases} \tag{2.3}$$

However, as with many situations in cosmology, we cannot directly observe the desired quantity; we must infer the proper distance using quantities that *are* measurable and compare them to what we would expect. The luminosity distance $d_L$ of a galaxy, for example, is defined as the distance at which a galaxy of luminosity $L$ would be detected with flux $F$ in a *Euclidean* Universe i.e.

$$F = \frac{L}{4\pi d_L^2}. \tag{2.4}$$

$d_L$ is then related to the coordinate distance in Equation (1.20) as

$$R_0 r = \frac{d_L}{(1 + z)}. \tag{2.5}$$

For standard GR-based models such as $\Lambda$CDM and UDM discussed in Chapter 1, $d_L$ as a function of redshift and curvature is then given by

$$d_L = \begin{cases} cH_0^{-1}(1+z) \int_0^z \frac{\mathrm{d}z}{E(z)} & \text{for } k = 0 \\[2ex] \frac{cH_0^{-1}(1+z)}{|\Omega_{k_0}|} \sinh\left( |\Omega_{k_0}|^{1/2} \int_0^z \frac{\mathrm{d}z}{E(z)} \right) & \text{for } k = -1 \\[2ex] \frac{cH_0^{-1}(1+z)}{|\Omega_{k_0}|} \sin\left( |\Omega_{k_0}|^{1/2} \int_0^z \frac{\mathrm{d}z}{E(z)} \right) & \text{for } k = +1, \end{cases} \tag{2.6}$$

where $E(z)$ from Equation (1.19) is model dependent as seen in Chapter 1. For a non-GR model such as Conformal Gravity, Equation (2.5) also holds and $d_L$ is given by combining this with Equation (1.21). The luminosity distance then has a functional dependency on the true parameters of the cosmology $(H_0, \Omega_i)$: if the intervening space between the observer and galaxy is *not* Euclidean, Equations (2.4) and (2.1) will not hold. Any discrepancies between the predicted and

measured position can then be used to constrain the correct cosmology, which we discuss in §2.4. However, in order to quantify any deviation we must have some way to ascertain the true luminosity at the source, i.e. $M$.

## 2.1.2 Calibrated Distance Indicators

The initial rung on the cosmological distance scale is provided by primary indicators; these distances are measured directly and do not depend on the physics of the object in question. Examples include radar ranging to define the astronomical unit and parallax measurements of nearby stars. However, beyond this scale direct measurements are no longer possible and calibrations must be found that relate observable properties, such as spectral features, to the intrinsic luminosity of the source.

### Type 1a Supernovae

To date, one of the most widely used distance indicators has been Type 1a Supernovae (SN1a) – the end state of a massive star that releases enough energy to momentarily outshine its host galaxy (A comprehensive review can be found in [23]). The similarity in the observed lightcurves (Figure 2.1) as they decay from maximum light suggests the underlying physics of these events is consistent and varies little from source to source. Type 1 supernovae are distinguished from type 2 through the absence from the spectrum of the hydrogen Balmer lines. Within this classification, type 1 events can then be subdivided further, with type 1a exhibiting a singly-ionised silicon line near maximum light.

The consistency in the maximum energy released is thought to be due to the event being triggered by a carbon-oxygen white dwarf accreting mass from a binary companion until the white dwarf approaches the Chandrasekhar mass limit and electron-degeneracy pressure can no longer support the star. It then undergoes thermonuclear explosion, releasing enough energy to completely unbind the star. As SN1a are triggered by a consistent mechanism, the absolute magnitude can be assumed to be constant. This can be calibrated using nearby (and therefore cosmology-independent) supernovae by measuring the redshift and hence distance of the host galaxy and the apparent magnitude of the event $m$.

See reference in caption for image.

Figure 2.1: The majority of measured Type 1a SN lightcurves are uniform and lie on the yellow band in Box (a). This consistency allows SN to be used as a standard candle. The timescale of a SN event is dependent on its luminosity, with the more energetic events brightening and fading more slowly than dimmer events. Box (b) shows how outliers from the yellow band can be normalised according to their timescale and scaling the brightness accordingly [24].

Equation (2.1) is then used to fix the absolute magnitude $M$. High redshift observations can then be used to probe any deviation in the cosmology compared to the locally-flat calibration conditions as the events would appear dimmer or brighter than expected. However, while this model has been long established and well corroborated [8], high redshift supernovae do show an intrinsic scatter in the maximum absolute magnitude and non-uniformities in lightcurve profiles. These discrepancies suggest SN1a are not perfect standard candles [24]. This is due either to inconsistencies in the events themselves or potential evolution of the progenitors with redshift.

Aside from standard candle observations, recent measurements of the CMBR and baryon acoustic oscillations (BAO) have allowed standard *rulers* to be established. These rulers define an expected characteristic length scale that can then be compared to observations at a given distance for a given cosmology. Any deviation in the measured length of the ruler from the expected value can then be used to constrain the cosmology.

### Cosmic Microwave Background Radiation

The relic light of recombination, redshifted to micro-wavelengths, has been hailed as one of the most important discoveries of modern astronomy. Not only does it lend further weight to the hot big bang model, it also provides an unprecedented snapshot of the Universe at a mere 380,000 years old. The imprint of density fluctuations in the early universe can be seen as fractional temperature fluctuations in the all-sky image and these density fluctuations have seeded the large-scale structure visible today through galaxy redshift surveys.
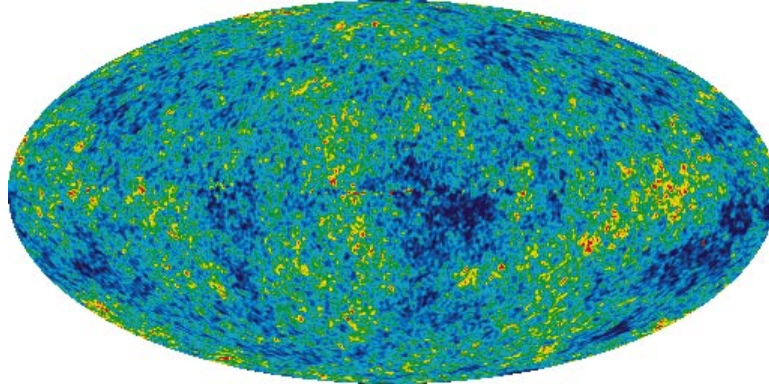


Figure 2.2: Temperature fluctuations in the Cosmic Microwave Background Radiation (CMBR) have been mapped over 5 years by the WMAP project, yielding an unprecedented view of the perturbations present in the Universe only 380,000 years after the Big Bang [15].

The temperature fluctuations can be mapped as a function of angular separation on the sky to produce an angular power spectrum. Correlations between temperature anisotropies and angular scale result in distinct peaks in the power spectrum, as shown in Figure 2.3. The position of these peaks is cosmology-dependent and the power spectrum can therefore be used to place constraints on model parameters.

The key tool for fitting model parameters with the CMBR power spectrum is the shift parameter $R$ [25]

$$R = \sqrt{\Omega_m} H_0 r(z_{CMB}),$$  (2.7)

where $r(z_{CMB})$ is the comoving distance to the surface of recombination at $z = 1089$, given by

$$r(z_{CMB}) = \frac{c}{H_0 \sqrt{|\Omega_k|}} \operatorname{sinn}\left[ \sqrt{|\Omega_k|} \int_0^{z_{CMB}} \frac{\mathrm{d}z'}{E(z')} \right].$$  (2.8)

$E(z)$ is given by Equation (1.15) and $\operatorname{sinn}(x) = \sin(x), x, \sinh(x)$ for $\Omega_k < 0, \Omega_k = 0$ and $\Omega_k > 0$ respectively. The shift parameter $R$ relates the movement of the peaks along the angular size axis as the model parameters are changed. For example, varying $\Omega_\Lambda$ shifts the position $\ell$ of the first peak in the power spectrum to $R\ell$. The 'observed' value of $R$ can be derived from the CMBR data and compared to the value calculated for any selected combination of model parameters using Equations (2.7) and (2.8).
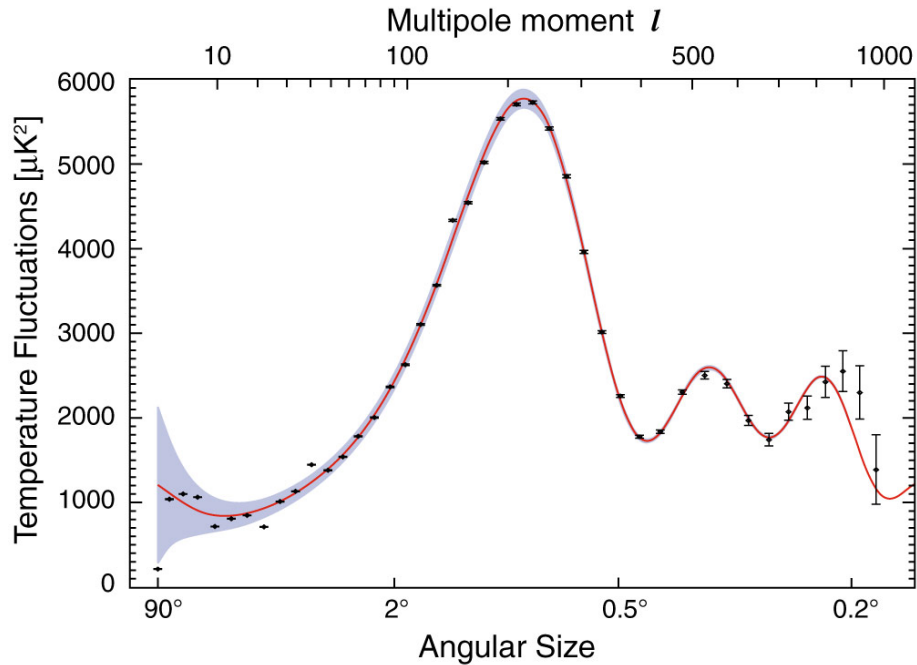


Figure 2.3: The angular power spectrum of the CMBR temperature anisotropies displays distinct peaks. The position of these peaks is related to the underlying cosmology, thus providing an effective constraint on model parameters. The measured positions are shown as points and the best-fit $\Lambda$CDM as a continuous line [15].

**Baryon Acoustic Oscillations**

The acoustic oscillations present in the plasma that subsequently recombined and emitted the CMBR can also expect to be detected in the non-relativistic component of the early universe – the baryonic and dark matter [26], [12].

See reference in caption for image.

Figure 2.4: The baryon acoustic peak measured for luminous red galaxies in the SDSS compared with $\Lambda$CDM models of varying baryon density [27].

Within a $\Lambda$CDM construct, an initial density perturbation in the pre-recombination universe consists of dark matter, hot baryonic plasma, photons and neutrinos. As the neutrinos are only weakly interacting, they escape the perturbation and can be discounted. The dark matter is cold and therefore does not move but simply attracts more matter gravitationally and therefore the initial perturbation grows. As the baryonic matter is hot and ionised, the photons are coupled to this plasma and the excess pressure resulting from the over-density results in an expanding spherical density wave. As the Universe expands and cools, this wave is carried outwards until recombination occurs and the photons and plasma decouple. The photons are now free to propagate and are emitted as the CMBR. The decreasing density of the expanding universe results in a much reduced sound speed, thus the density wave effectively stops expanding, resulting in a dark matter perturbation at the original point of over-density and a shell of baryonic matter a distance away. These perturbations then gravitationally attract one another and

surrounding matter, growing and smoothing out as they do. The baryonic over-density is then left imprinted on the dark matter density a measurable distance from the initial perturbation. As the Universe has also been expanding during this process, the density wave has grown with it, resulting in the radius of the gas shell being $\mathcal{O}(100\text{Mpc})$ [12]. As galaxies are believed to form around over-densities in the background dark matter, there should then be an increase in the number of galaxies found with a spatial separation of $\sim$100Mpc. Figure 2.4 shows the correlation function of luminous red galaxies in the Sloan Digital Sky Survey (SDSS), with the measured peak and several fits for differing baryon densities.

The angular scale parameter of the matter power spectrum of a galaxy survey (analogous to the CMBR shift parameter) is given by [25]

$$A = \frac{\sqrt{\Omega_m}H_0}{cz_{BAO}} \left[ \frac{cz_{BAO}}{H(z_{BAO})} r^2(z_{BAO}) \right]^{1/3}, \tag{2.9}$$

where $r(z_{BAO})$ is again given by Equation (2.8) for $z_{BAO}$ equal to the average redshift of the galaxy survey employed. $A$ measured from a large scale survey of galaxies can then be compared to the value predicted by a cosmological model, in a manner similar to the CMBR shift parameter $R$.

## 2.2 Gravitational Wave Standard Sirens

The electromagnetic spectrum allows many windows of observation and sources that seem otherwise mundane in optical wavelengths have proven to be spectacularly active in others. However, the detection of gravitational waves, a prediction of GR, would provide an entirely new regime for observational astrophysics.

### 2.2.1 Some Basic GR Theory

Following §1.1.1, matter curves otherwise flat spacetime, with the shape encoded in the metric $g_{\mu\nu}$. Far from massive sources in the weak field limit, however, spacetime is nearly flat. We can therefore consider the metric $g_{\mu\nu}$ to consist of the flat Minkowski metric $\eta_{\mu\nu}$ with a small addition due to the weak gravitational field of a distant source i.e.

$$g_{\mu\nu} = \eta_{\mu\nu} + h_{\mu\nu}, \tag{2.10}$$

for $|h_{\mu\nu}| \ll 1$. It can then be shown [28] that the components of $h_{\mu\nu}$ will transform in a similar manner to the metric $g_{\mu\nu}$, thus preserving the original weak field, 'nearly Lorentz' condition of the coordinate system. Therefore, any changes in the components of $h_{\mu\nu}$ will impart a similar change on the metric $g_{\mu\nu}$. In this weak field regime, the Einstein field equations given in Equation (1.2) can then be shown to be a function only of the appropriately scaled perturbations to the spacetime metric, with the solution in the form of a wave equation [28]

$$\left( -\frac{\partial^2}{\partial t^2} + c^2 \nabla^2 \right) \bar{h}_{\mu\nu} = 0, \tag{2.11}$$

where $\bar{h}_{\mu\nu}$ represents the re-scaled perturbations. Equation (2.11) implies that disturbances in spacetime $h_{\mu\nu}$, and hence in the metric $g_{\mu\nu}$, propagate through spacetime as waves with speed $c$. These 'gravitational waves' will then be detectable through their effect on test particles that are otherwise at rest.

The physical implications of any disturbance in spacetime can be shown by considering the proper distance between two test particles initially at rest in a flat spacetime, one at the origin at the other at $x = \epsilon, y = z = 0$. Following Equation (1.1), the proper distance between the two test particles is [28]

$$\Delta l = \int |\mathrm{d}s|^{1/2} = \int |g_{\mu\nu}\mathrm{d}x^\mu \mathrm{d}x^\nu|^{1/2}$$
$$= \int_0^\epsilon |g_{xx}|^{1/2}$$
$$\approx |g_{xx}(x=0)|^{1/2}\epsilon.$$

From Equation (2.10), it then holds that

$$g_{xx}(x=0) = \eta_{xx} + h_{xx}^{TT}(x=0), \tag{2.12}$$

where $h_{xx}^{TT}$ is the perturbation re-scaled to the Transverse-Traceless Lorentz gauge [28]. Recalling that $\eta_{xx} = 1$, the proper distance can then be expressed as

$$\Delta l \approx \left[ 1 + \frac{1}{2}h_{xx}^{TT}(x=0) \right] \epsilon. \tag{2.13}$$

As $h_{xx}^{TT}$ is not identically zero, the proper distance is then a function of the perturbations and will change in time. Gravitational wave detectors, such as LIGO [29] and the forthcoming LISA [30] mission, have been designed to measure this change in separation between test particles. However, the difficulty in

directly detecting this gravitational radiation is due to the cosmological distance between the source and the detector over which the wave must propagate. The amplitude of gravitational radiation drops off directly with distance (analogous to electromagnetic radiation), thus even very large perturbations from a massive source will have reduced in amplitude by a factor approximately equal to the distance from the source. Current gravitational wave detectors are therefore challenged with measuring a relative displacement of $10^{-21}$.

## 2.2.2 Gravitational Wave Sources

It can be shown [28] that gravitational radiation is quadrupole in nature; furthermore, the quadrupole from a spherically symmetric mass distribution is identically zero. Thus associated metric perturbations, such as a star collapsing spherically symmetrically, will not produce gravitational radiation. However, compact object binary inspiral systems will emit gravitational radiation that may be strong enough to be detected at Earth.

See reference in caption for image.

Figure 2.5: The measured decay in orbit of the pulsar binary PSR 1916+13 compared with the expected decay if the energy loss was due to gravitational radiation [31].

The best indirect evidence of gravitational waves comes from the binary pulsar PSR 1913+16, in orbit with a companion star. Precise measurements of the pulsar orbit display not only an advance of perihelion, as predicted by GR, but the gradual inspiral of the binary system [31]. Figure 2.5 shows the measured

decrease in orbital period over several years compared with the decrease predicted by GR. Gravitational waves are therefore a likely candidate to explain the loss of energy from the binary system.

Any binary system will radiate gravitational waves. However, as discussed previously, the technical challenges of detecting this radiation are already great due to the large source distances involved. The most desirable candidates for initial detection and use as standard sirens will therefore be compact object binary systems, consisting of neutron stars and black holes.

### 2.2.3 Utilising Compact Object Inspirals as Gravitational Wave Standard Sirens

As a binary system gradually loses energy in the form of gravitational radiation, the orbital period reduces and the two components spiral inwards towards one another. Eventually, the binary companions will coalesce, emitting very large amounts of electromagnetic and gravitational radiation. However, the physics behind such a merger is very complex and difficult to decipher. The most detailed and important information can be gleaned from the last few hundred orbits of the system, prior to coalescence, as the orbital radius decreases rapidly and the geometry of the system becomes increasingly circular. As this happens, the gravitational luminosity of the source increases as $1/r^5$, where $r$ is the orbital radius and the source can be detected by its distinctive signal, referred to as a 'chirp' [32]. The waveform of this chirp signal of increasing frequency $f$ and amplitude $h$ is directly dependent on the luminosity distance of the source $d_L$ and the 'chirp mass' of the system $\mathcal{M}$ [33], such that

$$h_0(f) \propto \frac{\mathcal{M}^{5/6}}{d_L} f^{-7/6} \exp\left[i\Psi(f)\right], \tag{2.14}$$

where $\Psi(f)$ is the phase and the chirp mass for companion masses $m_1$ and $m_2$ is given by

$$\mathcal{M} = (m_1 m_2)^{3/5} (m_1 + m_2)^{-1/5}. \tag{2.15}$$

Accurate modelling of the detected waveform, an example of which can be seen in Figure 2.6, can therefore allow determination of the luminosity distance of the source. This is then calibrated against the measured redshift of the host

galaxy and standard sirens can then be utilised in a similar fashion to standard candles. However, the significant contrast between these two indicators is the order of magnitude smaller errors associated with a standard siren [33], due to the accuracy with which the source parameters can be measured. In principle, $LISA$ is expected to pinpoint distances to supermassive binary black hole (SMBBH) inspirals with an accuracy of better than 1% [33]. Unfortunately, while the theory underpinning this highly accurate distance indicator is well understood, potential obstacles do exist.

See reference in caption for image.

Figure 2.6: The left panel shows the waveform emitted from a stable binary system prior to the final stages of coalescing. As the orbital period rapidly decreases in the final few hundred orbits, the frequency and amplitude of the emitted waveform increase greatly, resulting in a distinctive 'chirp'.

Aside from relying on electromagnetic observations to pinpoint the redshift of the host galaxy, the gravitational wave signal will be degraded by weak gravitational lensing due to large-scale structure mass density fluctuations. In the short term, this can be avoided by only considering low redshift sources at $z \leq 0.5$. However, the stochastic lensing background must somehow be accounted for if observations at high redshift are to be utilised to their full potential. A full discussion of the effect lensing has on high redshift sirens can be found in [34] and in [35].

Should these obstacles be overcome, standard sirens could be the most accurate distance indicators available. In addition to the high source luminosity and therefore high redshift potential for detection, sirens also by-pass the need for

the cosmological distance ladder. The uncertainties in measurements can there-
fore be directly and reliably quantified and have no dependence on less accurate
sources. We will illustrate the potential diagnostic power of gravitational wave
standard sirens in Chapter 5 after first examining another high redshift candidate
for which a large amount of data already exists.

## 2.3   GRBs as Cosmological Distance Indicators

A GRB event is the most luminous astrophysical phenomenon in the Universe
after the Big Bang, with a peak spectral energy $E_p$ in excess of $10^{43}$ Joules [36].
Although their high luminosity and isotropic distribution across the sky allow for
easy detection, details of their origin remain poorly understood. However, since
the launch of the SWIFT [37] satellite in 2004, dedicated to detecting GRBs,
large amounts of new data (3-4 events per week) has facilitated the development
of plausible mechanisms. These include a massive-star end stage collapse or a
binary merger, both similar to Supernovae [38], but occurring at significantly
higher energies ($\sim 10^3$ greater). While the study of the events themselves poses
many interesting astrophysical questions, it is hoped that GRBs may also be able
to be utilised as an effective high-redshift distance probe [39], [40] and it is the
latter topic that provides the main focus of this thesis.

### 2.3.1   Basic Properties

Discovered serendipitously in the 1960s by the United States Army, GRBs still
prove an enigma to astrophysicists, despite an ever increasing amount of data.
The challenge in finding a coherent progenitor model arises from the large vari-
ation in the properties of each event. Figure 2.7 shows several GRB lightcurves
obtained from the BATSE experiment [41] that formed part of NASA's flag-
ship Compton Gamma-Ray Observatory. Unlike Type 1a Supernovae, these
lightcurves are all unique; the peak energy, burst duration and variability vary
widely from plot to plot. It is therefore necessary to identify trends that may
point to underlying similarities. The main categorisation splits bursts into 2 sub-
sets based on event time – short and long – with the division occurring around

2s, as can be seen in Figure 2.7. Two different progenitors are then postulated: a higher energy, short event arising from a compact object binary merger; and a relatively lower energy, longer burst due to a massive-star end state collapse, similar to a supernova and often dubbed a 'hypernova' [38]. However, it has been postulated that the emission from both subsets of events is highly relativistically beamed in two collimated axial jets [42], in contrast to supernovae that evolve with a spherically expanding shell.

See reference in caption for image.

Figure 2.7: A selection of lightcurves from BATSE (top) and a histogram showing the temporal distribution of events, with an apparent division around 2s (bottom) [41].

To the observer along the jet axis, both these emission geometries can initially appear the same; this occurs for a jet, half-opening angle $\theta$, with a Lorentz factor $\gamma$ larger than $\theta^{-1}$. However, as the fireball evolves over time the afterglow lightcurve will exhibit a break in the decay power law when $\gamma < \theta^{-1}$. This feature is clearly visible in many events. The jet opening angle can then be derived from the jet break time $t_j$ as [43]

$$\theta = 0.163 \left( \frac{t_{j,d}}{1+z} \right)^{3/8} \left( \frac{n_0}{E_{iso,52}} \frac{\eta_\gamma}{1-\eta_\gamma} \right)^{1/8} , \qquad (2.16)$$

where $t_{j,d} = t_j/1\text{day}$ , $E_{iso,52} = E_{iso}/10^{52}\text{ergs}$ and $n_0 = n/1\text{cm}^{-3}$. $E_{iso}$ is the isotropic equivalent energy released in the fireball, assuming it is expanding into a constant circumburst particle density $n$ with a fraction $\eta_\gamma$ of its kinetic energy being converted into prompt gamma rays. Many GRB spectra display a clear break and it is hoped that by being able to standardise events it will be possible to ascertain common properties that may lead to a new standard candle.

See reference in caption for image.

Figure 2.8: The projected redshift distribution of Type 1a SN that may be obtained from SNAP [44] (left) and the current distribution of 76 GRBs with known redshift (right) [45].

If it is possible to utilise GRBs as a high redshift indicator, a whole new epoch will become measurable. The highest recorded redshift of Type 1a Supernovae is at $z \sim 1.7$ and the next reliable point is provided by the CMBR at $z \sim 1089$. Our knowledge of the intervening epochs is rather limited and will remain so if we can only rely on SN1a as they are not intrinsically bright enough to be detected much beyond the current threshold. Figure 2.8 highlights the significantly deeper redshift range over which GRBs are detectable compared with SN1a. However,

while Type 1a SN are considered to be standard (enough) candles, the peak energy $E_p$ and total emitted energy of GRBs varies over several orders of magnitude. This lack of a direct estimate for the absolute magnitude has resulted in several groups seeking a correlation based on directly measurable spectral features. This contrasts with initial attempts to standardise GRBs, such as the 'Amati Relation' [46], which attempted to adopt a true standard candle assumption that the GRB energy is approximately constant.

## 2.3.2 The Ghirlanda Relation

While other potential spectral correlations exist – a comprehensive appraisal can be found in [47] and is reviewed in §3.1.1 – this thesis chiefly addresses what has become known as the 'Ghirlanda Relation' [36]. This is a proposed correlation between the peak energy $E_p$ in the $\nu F_\nu$ spectrum and the collimation-corrected burst energy $E_\gamma$. The peak spectral energy $E_p^{obs}$ is directly observed from the spectrum and redshift-corrected to give $E_p = E_p^{obs}(1+z)$. However, $E_\gamma$ must be inferred from the geometry of the collimated fireball model, outlined in §2.3.1. As the work in this thesis chiefly concerns a critique of the analysis carried out by Xu et al. [43], we follow their derivation of the relation.

The isotropic equivalent emission $E_{iso}$ is estimated from the time-integrated flux – the fluence $S_\gamma$ – received at the detector. For a source at redshift $z$ and at a distance based on this redshift $d_L$ given by Equation (2.6), the isotropic energy released is given by a simple inverse-square law

$$E_{iso} = \frac{4\pi d_L^2 S_\gamma k}{(1+z)},$$
(2.17)

where $k$ is the redshift-dependent $k$-correction factor. The collimated energy released by the GRB jets is then given by

$$E_\gamma = (1 - \cos\theta)E_{iso},$$
(2.18)

where $\theta$ is the jet opening angle and is given by Equation (2.16).

The Ghirlanda Relation proposes that there exists a correlation between $E_p$ and $E_\gamma$, namely

$$\frac{E_\gamma}{10^{50}\text{ergs}} = C\left(\frac{E_p}{100\text{keV}}\right)^a,$$
(2.19)

where $a$ and $C$ are the correlation parameters. Assuming the small angle approximation that $\theta \ll 1$, Equations (2.16), (2.17), (2.18) and (2.19) are then combined to give the luminosity distance of the source based on *observed* quantities

$$d_{L,obs} = 7.575 \frac{(1+z)C^{2/3}\left[E_p/100\text{keV}\right]^{2a/3}}{(kS_\gamma t_{j,d})^{1/2}(n_0\eta_\gamma)^{1/6}} \text{ Mpc.} \tag{2.20}$$

The fractional uncertainty in $E_\gamma$ is given as

$$\left(\frac{\sigma_{E_\gamma}}{E_\gamma}\right)^2 = \left(1 - \sqrt{C_\theta}\right)^2\left[\left(\frac{\sigma_{S_\gamma}}{S_\gamma}\right)^2 + \left(\frac{\sigma_k}{k}\right)^2\right]$$
$$+ C_\theta\left[\left(\frac{3\sigma_{t_j}}{t_j}\right)^2 + \left(\frac{\sigma_{n_0}}{n_0}\right)^2 + \left(\frac{\sigma_{\eta_\gamma}}{\eta_\gamma - \eta_\gamma^2}\right)^2\right], \tag{2.21}$$

where

$$C_\theta = \left(\frac{\theta\sin\theta}{8 - 8\cos\theta}\right)^2. \tag{2.22}$$

This then allows the fractional uncertainty in $d_L$ to be calculated as

$$\left(\frac{\sigma_{d_L}}{d_L}\right)^2 = \frac{1}{4\left(1 - \sqrt{C_\theta}\right)^2}\left[\left(\frac{\sigma_{E_\gamma}}{E_\gamma}\right) + \left(\frac{\sigma_C}{C}\right)^2 + \right.$$
$$\left. \left(a\frac{\sigma_{E_p^{obs}}}{E_p^{obs}}\right)^2 + \left(a\frac{\sigma_a}{a}\ln\frac{E_p}{100}\right)^2\right]. \tag{2.23}$$

Should Equation (2.19) hold, it would allow a predicted and observed luminosity distance to be statistically compared in a bid to further constrain cosmological parameters as outlined in the following section.

## 2.4   Statistical Analysis Methods for Parameter Estimation

The necessity of reliable methods to extract the maximum amount of information from sometimes limited data is further emphasised by our ability to experience only *one* universe; while multiverse scenarios may be considered in similar terms to the canonical ensembles of statistical mechanics, we have no way of making observations outwith our own universe. This affects the way in which we can interpret what the data tell us and how we assign uncertainties to any conclusions drawn.

There exist two main formalisms in the statistics employed across the cosmology literature – Bayesian and frequentist. Each allows us to quantify the probability of a proposed outcome occurring but are unique in their construction and therefore in how they should be interpreted. A frequentist regime is perhaps more intuitive; repeating measurements a theoretically infinite number of times, under identical conditions, and noting the relative frequency of the outcomes of our experiments allows an estimation of how likely a future outcome may be. However, we cannot start another universe and observe if it evolves along a similar trajectory to how we think our current universe has developed.

Bayesian inference instead relies on assessing the evidence that exists from a sample of any given number of observations and assigning a conditional degree of belief for a proposed hypothesis, according to specific rules for combining probabilities. In the context of cosmology, for example, the hypothesis may be that the Universe is flat; evidence can be accumulated through observations and the likelihood that this is true can then be calculated.

These two statistical paradigms are *not* interchangeable and while a frequentist approach has been widely favoured in the past, Bayesian inference is slowly being recognised as arguably the better option. The work in this thesis is also based on a Bayesian framework and as such the main focus of the relevant background will centre around techniques particular to that formalism.

## 2.4.1 Maximum Likelihood and Minimum $\chi^2$

Bayesian inference originates from independent work by Rev. Thomas Bayes and Pierre-Simon Laplace in the 18th Century. Bayes' Theorem is used to compute the posterior probability of a hypothesis given a set of observations, incorporating any prior knowledge of the probability. It is commonly expressed as [48]

$$p(H|D, I) = \frac{p(H|I)p(D|H, I)}{p(D|I)}. \tag{2.24}$$

This states the posterior probability $p(H|D, I)$ of hypothesis $H$ is based on data $D$ and prior information $I$. It is a function of the prior probability $p(H|I)$, the likelihood function $p(D|H, I)$, which expresses the probability of obtaining data $D$ if $H$ and $I$ are true, and the evidence $p(D|I)$, which is a constant (for a given

set of data) for all hypotheses. For a continuous parameter space $x$, the probability distribution function (pdf) tells us the probability of any particular parameter value and is normally peaked at the most likely value $x_0$. In the context of cosmology, the hypothesis is a parameter dependent model and therefore the pdf can be calculated across the parameter space to identify the most likely parameter values for the measured data. This is commonly referred to as *parameter estimation*, although strictly speaking it is the calculation of the full posterior pdf across the whole space and not just its reduction to a single point or set of points. As the integral of the posterior pdf must be unity (the sum of all probabilities in the parameter space must equal 1), the evidence $p(D|I)$, which is independent of $H$, acts as the normalisation constant. Therefore, the posterior probability is simply proportional to the product of the prior and likelihood. If we are fairly ignorant of any previous information regarding our hypothesis, a uniform prior may be applied, which is constant for all parameter values within a specified range. In this case the posterior probability is now simply proportional to the likelihood i.e.

$$p(H|D, I) \propto p(D|H, I). \tag{2.25}$$

Thus evaluating the likelihood is equivalent to evaluating the full posterior probability. As the most probable value is given by the peak in the pdf – $p(x_0|D, I) = p_{max}$ – the maximum can be evaluated at this value $x_0$ as

$$\left.\frac{\mathrm{d}p}{\mathrm{d}x}\right|_{x_0} = 0 \qquad \text{and} \qquad \left.\frac{\mathrm{d}^2 p}{\mathrm{d}x^2}\right|_{x_0} < 0. \tag{2.26}$$

Taylor expansion of the log-posterior probability about $x_0$ gives

$$L(x) \equiv \ln\left[p(x|D, I)\right] = L(x_0) + \frac{1}{2}\left.\frac{\mathrm{d}^2 L}{\mathrm{d}x^2}\right|_{x_0} (x - x_0)^2 + \dots \tag{2.27}$$

Therefore

$$p(x|D, I) = C \exp\left[\frac{1}{2}\left.\frac{\mathrm{d}^2 L}{\mathrm{d}x^2}\right|_{x_0} (x - x_0)^2\right]. \tag{2.28}$$

This is a Gaussian distribution with $C = \dfrac{1}{\sqrt{2\pi}\sigma}$ and $\sigma = \left[-\left.\dfrac{\mathrm{d}^2 L}{\mathrm{d}x^2}\right|_{x_0}\right]^{-1/2}$.

From Equation (2.25), the likelihood, which is a measure of the probability of

the data given the hypothesis and other relevant information, can then be expressed as

$$p(D|H, I) = \frac{1}{\sqrt{2\pi\sigma}} \exp\left[-\frac{1}{2}\chi^2\right], \tag{2.29}$$

where $\chi^2$ is the sum of the squares of the normalised residuals of the expected values for the proposed model (ideal data $\{M_n\}$) compared with the measured data $\{D_n\}$, with errors $\{\sigma_n\}$ i.e.

$$\chi^2 = \sum_{i=1}^{n} \left(\frac{M_i - D_i}{\sigma_i}\right)^2. \tag{2.30}$$

Therefore, under the assumption that the residuals are independently and identically drawn from a normal distribution, minimising $\chi^2$ will identify the position of maximum likelihood in the parameter space, removing the need to calculate the full posterior pdf. This method, also commonly referred to as *least-squares fitting*, results directly from Bayes' Theorem and is one of the most widely used methods in cosmological parameter estimation.

In addition to identifying the location of the most probable parameter values, the overall shape of the likelihood can be examined by assessing what fraction of the total pdf lies within selected limits, allowing an assessment of the spread of the pdf around the central point. The narrower the spread, and hence more peaked the distribution, the more convincing it is that the correct parameter values have been identified. Conversely, a wide spread around the peak in the pdf may not instil such high confidence in the result. The width of the central distribution is quantified in terms of its first and second moments – the mean and mean square, respectively – where the $r^{th}$ moment of a pdf $p(x)$ is defined as

$$< x^r > = \int_{\infty}^{\infty} x^r p(x) \mathrm{d}x. \tag{2.31}$$

The variance is defined as $\mathrm{var}[x] \equiv \sigma^2 = < x^2 > - < x >^2$ and from this we obtain the standard deviation $\sigma$. The spread of the pdf is then quoted in multiples of $\sigma$ e.g. 1, 2 or 3 standard deviations of the maximum. This corresponds to enclosing 68.3%, 95.4% or 99.73% of a Gaussian distribution centred on the most probable value. These boundaries can be represented in the parameter space by contours of constant $\Delta\chi^2$, measured from $\chi^2_{min}$, and are dependent on the number of model

parameters. These values represent confidence levels and are used in a Bayesian context to quantify the degree of belief in the conclusions drawn from the data set. The corresponding values of $\Delta\chi^2$ as a function of confidence level and number of degrees of freedom can be seen in Table 2.1 [49], while an illustrative plot of a Gaussian likelihood with associated contours is shown in Figure 2.9.

| p | $\nu$ | | | | | |
|---|---|---|---|---|---|---|
| | 1 | 2 | 3 | 4 | 5 | 6 |
| 68.3% | 1.00 | 2.30 | 3.53 | 4.72 | 5.89 | 7.04 |
| 90% | 2.71 | 4.61 | 6.25 | 7.78 | 9.24 | 10.6 |
| 95.4% | 4.00 | 6.17 | 8.02 | 9.70 | 11.3 | 12.8 |
| 99% | 6.63 | 9.21 | 11.3 | 13.3 | 15.1 | 16.8 |
| 99.73% | 9.00 | 11.8 | 14.2 | 16.3 | 18.2 | 20.1 |
| 99.99% | 15.1 | 18.4 | 21.1 | 23.5 | 25.7 | 27.8 |

Table 2.1: $\Delta\chi^2$ as a function of Confidence Level and Degrees of Freedom $\nu$ for a multivariate normal pdf.
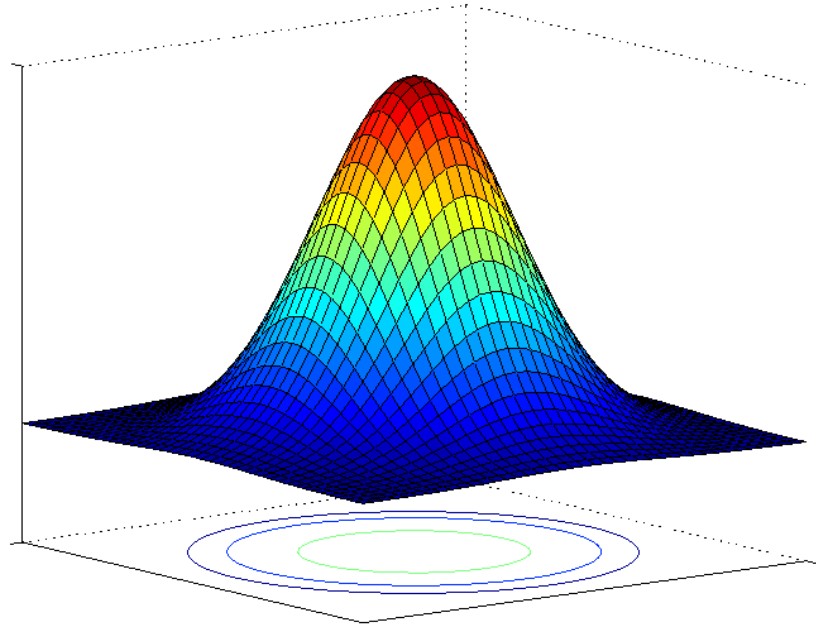


Figure 2.9: A Gaussian likelihood function with associated contours enclosing 68.3%, 95.4% and 99.73% of the total area. These limits are standard levels at which to draw confidence regions and correspond to significance levels of 1, 2 and $3\sigma$, respectively.

Least-squares fitting provides a simple and illustrative way to report new constraints on cosmological parameter values with each additional data set obtained. By measuring the observed distance modulus $\mu_{obs}$ and associated errors $\sigma_{\mu_{obs}}$ and

comparing this to the predicted value $\mu_{pred}$, as outlined in §2.1, the $\chi^2$-statistic can be constructed and minimised to identify the most probable parameter values. Equation (2.30) then becomes

$$\chi^2 = \sum_{i=1}^{n} \left( \frac{\mu_{pred} - \mu_{obs}}{\sigma_{\mu_{obs}}} \right)^2. \tag{2.32}$$

However, the confidence regions defined in Table 2.1 are only applicable when the errors are Gaussian, as we will go on to demonstrate in Chapter 3. It is therefore desirable to have an alternative method for evaluating the likelihood function.

## 2.4.2 Markov Chain Monte Carlo

Calculating the full posterior pdf can be computationally time-consuming, especially for models with a large number of parameters. Markov Chain Monte Carlo (MCMC) is a simple yet powerful tool for evaluating a multi-dimensional integral. The method uses a Metropolis-Hastings algorithm to construct a Markov chain in order to identify the maximum of the function and map out the shape of its neighbourhood in the defined parameter space [48]. Instead of drawing many independent samples from the posterior pdf $p(H|D, I)$, a Metropolis-Hastings algorithm constructs a random walk through the parameter space, with the probability of sampling any particular area of the desired pdf being proportional to the value of $p(H|D, I)$ in that region i.e. a Markov chain will take more samples from an area of high probability and waste less computation time sampling areas of low probability. The resulting chain then provides a fully representative sample of the $p(H|D, I)$, while greatly reducing the computational time required to evaluate the integral.

The Markov chain samples points from the parameter space and accepts or rejects them as the next point in the chain based on a pre-defined acceptance criterion. For illustrative purposes consider a Gaussian pdf $L$ with 2 parameters $(a, b)$ required to fit a straight line to data $\{x, y\}$

$$L(a, b) = \frac{1}{\sqrt{2\pi}\sigma} \exp \left[ -\frac{1}{2} \left( \frac{y - (ax + b)}{\sigma} \right)^2 \right]. \tag{2.33}$$

Figure 2.10: The proposal density $Q(x)$ is drawn around the sample point $x^{(1)}$ with the step size $\epsilon$ dictated by $\sigma_a$ and $\sigma_b$ from Equation (2.34). $L$ defines the longest length scale within the probable region and $\epsilon$ is chosen to be short relative to $L$ [50].

The initial point $P_1 = (a, b)$ is sampled such that $a_1 \sim \mathrm{U}[0, 1]$ and $b_1 \sim \mathrm{U}[0, 1]$. A tentative subsequent point $P' = (a', b')$ is then sampled from a *proposal density* $Q$ centred on $P_1$, as illustrated in Figure 2.10, where

$$Q(a, b) = \frac{1}{\sqrt{2\pi}\sigma_a} \exp\left[\frac{1}{2\sigma_a^2}(a' - a_1)^2\right] \times \frac{1}{\sqrt{2\pi}\sigma_b} \exp\left[\frac{1}{2\sigma_b^2}(b' - b_1)^2\right], \quad (2.34)$$

where $\sigma_a$ and $\sigma_b$ can be adjusted to sample more efficiently. The acceptance criterion is then based on the ratio of likelihoods of these two points

$$R = \frac{L(a', b')}{L(a_1, b_1)}. \quad (2.35)$$

If $R > 1$ then we accept $P'$ as the next point in the chain such that $P_2 = P'$. However, for $R < 1$ we accept $P'$ with probability $R$. This can in turn be achieved by sampling a random variable $x \sim \mathrm{U}[0, 1]$; we accept $P'$ only if $x < R$ and reject $P'$ if $x > R$, in which case $P_2 = P_1$. This sequence of points $\{P_1, P_2, P_3, \ldots, P_n\}$ is now a representative sample of $L(a, b)$. In addition to identifying the point in this chain where $L$ is a maximum, we can again define regions that contain a required fraction of the sample, and hence underlying distribution. For a sufficiently large sample size we order the likelihoods of the random sample $\underbrace{\{L_1, \ldots, L_n\}}_{largest...smallest}$ and select the point that contains 68.3%, 95.4% or 99% of these values as a good estimator of the 68.3, 95.4 or 99 percentile of the underlying likelihood function.

MCMC provides a remarkably simple method for investigating the properties of a probability distribution. Although the illustrative case presented here

contains only 2 parameters, the true power of MCMC becomes apparent for higher-dimensional problems when it is no longer computationally viable to solve the full posterior integral. However, the following work relies more heavily on MCMC due to it allowing the identification of confidence regions even when the errors are correlated and non-Gaussian. In the following chapters we show the inaccuracies introduced into statistical analysis if these criteria are not met.

# Chapter 3

# Limitations of Current GRB Data

The ongoing success of the SWIFT mission continues to provide unprecedented data on new GRB events. However, in order to utilise a GRB as a distance indicator it is essential to have a reliable optical counterpart – the host galaxy – from which to obtain the source redshift. Unfortunately, the high redshift nature of these events that makes them of interest to cosmologists renders pinpointing the host galaxy difficult. Subsequently, of the hundreds of GRBs detected to date [37], frustratingly few have been assigned reliable redshifts due to the difficulty in identifying an electromagnetic counterpart. Moreover, measurement of the observed source properties required to implement the Ghirlanda Relation outlined in §2.3.2 is also hampered, resulting in data being published with large measurement errors and source parameters being assigned fiducial values. In addition to this, a lack of low redshift events prevents GRBs being calibrated in a manner similar to Type 1a Supernovae, resulting in a cosmology-dependent circularity arising in the Ghirlanda Relation that must be resolved if any meaningful constraints are to be place on cosmological models and associated parameters.

In this chapter we begin with an overview of proposed spectral parameter correlations and discuss the previously identified shortcomings, based on an extensive appraisal by Friedman and Bloom [47]. We then perform a simple test to highlight the limitations in diagnostic power of a small data set with large errors. We directly compare the concordance model with an analogous Conformal Gravity parameterisation in order to illustrate and emphasise that GRBs can

currently add very little to the ongoing debate surrounding cosmological parameter estimation. We then go on to discuss the issues caused by circularity within the calibration of the Ghirlanda Relation and the steps required to overcome this problem. By constructing a simple statistical model we demonstrate the bias which can arise in the estimation of model parameters and identification of confidence intervals when employing incorrect statistical methods, such as those which undermine current analyses of the Ghirlanda relation. This chapter is based in part on work contained in Speirits et al. (2007) [51].

## 3.1 What Can Current GRB Data Tell Us?

Initial attempts to utilise GRBs as cosmological distance indicators were unfruitful due to a poor understanding of the nature of the events. Assuming that GRBs were similar to Supernovae, preliminary efforts focussed on relating the isotropic energy $E_{iso}$ to the luminosity (see [52], for example). However, the discovery that GRB emission is in fact jetted led to an essential geometry correction, given by Equation (2.18). This discovery paved the way for several proposed correlations between observed and derived spectral parameters, one of which, the so-called 'Ghirlanda Relation', is the main focus of this and the following chapter.

### 3.1.1 The Effect of Data Selection on the $E_p - E_\gamma$ Relation

GRB events have been detected and followed up by many different satellites. As such, not all the necessary data for each burst is available from a single source. While homogeneously acquired data would be desirable, in practice data sets must be compiled from all available published information. However, Friedman and Bloom [47] seek to construct as uniform and reliable a data set as possible and explicitly state their guidelines for data selection.

All events with missing redshift $z$, peak energy $E_p$ or jet break time $t_j$ are discarded as these parameters are essential in fitting any spectral correlation. All other parameters are selected on the criteria of completeness in value and accompanying errors, with the earliest available spectral data with the smallest best-fit errors taking precedence. Where noncritical parameter values are not available

in the published literature, a single value and associated error is adopted for all events, with the percentage error being indicative of those bursts with reported errors. Friedman and Bloom's assumptions include 10% errors for fluence $S_\gamma$ measurements and 20% errors on observed peak energy $E_p$ values. While an estimate of the circumburst medium density $n$ is commonly unavailable, and in these cases is assumed to be $n = 10 \pm 5$ cm$^{-3}$, there is no measure of the efficiency of the $\gamma$-ray emission mechanism and, citing earlier work by Frail et al. [53], Friedmann and Bloom fix this value at $\eta = 0.2$, a value repeated throughout the literature. However, the authors are the first to admit that assumptions regarding the circumburst density $n$ and efficiency $\eta$ greatly affect the analysis of the GRB data.

By comparing the 15 bursts that are common to both their selected data set and the events used in the original work by Ghirlanda et al. [36], Friedman and Bloom quantify the sensitivity of the analysis to different assumed values of circumburst density $n$ and associated errors. They conclude that the lowest values of $n_{min} \sim 1 - 2$ cm$^{-3}$ from a range of $n = 1 - 10$ cm$^{-3}$, with the highest fractional error $\sigma_n = 125\%$ yields the best fit of the $E_p - E_\gamma$ 'Ghirlanda' relation. Perhaps unsurprisingly, the original work reporting this potential correlation by Ghirlanda et al. utilises a value of $n = 3 \pm 3.74$ cm$^{-3}$ in order to achieve their reported goodness of fit, with reduced $\chi_\nu^2 = 1.27$. This contrasts with Friedman and Bloom's attempts to fit the $E_p - E_\gamma$ relation employing Ghirlanda et al.'s assumptions to their own data set, which differs slightly in the selected GRBs, resulting in a conflicting fit of $\chi_\nu^2 = 2.45$. Friedmann and Bloom cite discrepancies such as these for justifying their conclusions that the spectral correlation is highly sensitive to selection criteria from the literature and input assumptions. This sensitivity can be seen in their fits to their own and Ghirlanda et al.'s data sets in Figure 3.1.

Having justified their data selection criteria, Friedman and Bloom proceed to assess the cosmology-dependence of the relation. Prior to accounting for the cosmology-dependence of the $E_p - E_\gamma$ relation, the reported fit to the 19 GRBs constituting their own data set, under their own assumptions for a standard

See reference in caption for image.

Figure 3.1: Friedman and Bloom's fits to their data set (A) and Ghirlanda et al.'s data set (G and G*). G* denotes Ghirlanda et al.'s data set but Friedman and Bloom's assumptions for percentage errors. As is evident from the plots, the fit to the Ghirlanda Relation varies over a large range of $\chi^2$ values, depending on the assumed value for the circumburst density $n$ and its associated error $\sigma_n$ [47].

cosmology of $(\Omega_m, \Omega_\Lambda) = (0.3, 0.7)$ is $\chi^2_\nu = 3.71$, and is described as 'poor'. They find that the slope of the relation changes by no more than 25% across the parameter space and by around $5 - 10\%$ around the area of most relevance to the concordance model. Accounting for this parameter-dependence by fitting the relation for each pair of $(\Omega_m, \Omega_\Lambda)$ values does not significantly improve the fit.

In contrast to the conclusions of Ghirlanda et al. [36] and Xu et al. [43], Friedman and Bloom conclude that although the Ghirlanda Relation is an improvement on previous attempts at standardising GRB spectra, it provides no significant improvement in the constraints on cosmological parameters. In their view, this is mainly due to the currently small number of GRB calibrators, including the lack of low-redshift GRBs. Contributions to the uncertainty also arise from the sensitivity to data selection choices and to the values and ranges assumed for the number density of the surrounding medium $n$ and the efficiency of each event $\eta$. Friedman and Bloom provide a critical summary of previous attempts

to use GRBs for cosmography and caution that a much greater understanding of the events and the physical justification for potential spectral correlations is required before GRBs can realistically be used as reliable distance indicators.

In order to convey the uncertainty that these irregularities bring to cosmological applications of GRBs, we now proceed by quantifying the constraints GRBs can place on comparable cosmological models in the form of the concordance model and Conformal Gravity.

### 3.1.2 ΛCDM vs. Conformal Gravity

Cosmological models are commonly represented by their Hubble Diagram – a plot of distance modulus $\mu$ at a given redshift $z$, as outlined in §2.1.1. The measured distance moduli of observed sources can then be compared to this theoretical prediction and any differences quantified by the $\chi^2$ statistic outlined in §2.4.1. A value for the reduced $\chi^2$ per degree of freedom close to 1 suggests a good fit to the model, while a significant deviation from this indicates a poorer fit.
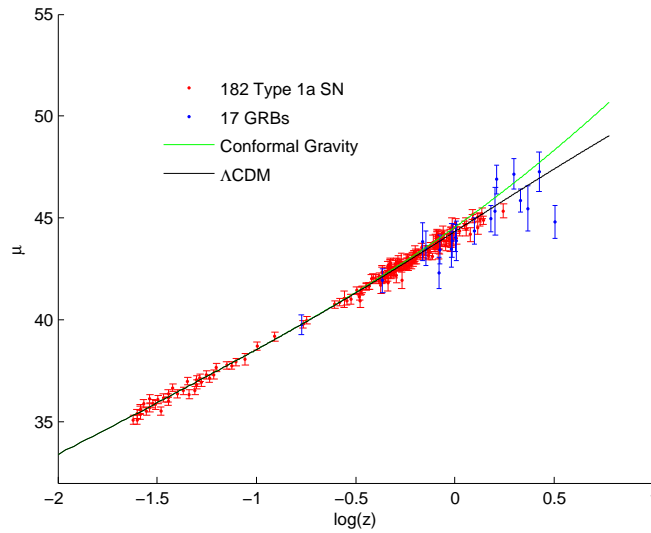


Figure 3.2: Hubble Diagrams for ΛCDM with $(\Omega_m, \Omega_\Lambda) = (0.3, 0.7)$ (Black) and Conformal Gravity with $q_0 = -0.55$ (Green) with 182 Type 1a SN (Red) and 19 GRBs (Blue). The deviation of the cosmological models can be seen to be insignificant at low redshift, emphasising the need for an accurate high redshift distance indicator.

Figure 3.2 shows the Hubble Diagrams for both ΛCDM and Conformal Gravity. The challenge in differentiating between them is apparent as they only diverge

significantly at redshift $z >> 1$. This has provided the motivation for developing a reliable high redshift distance indicator.

In order to quantify the issues raised in §3.1.1, we have selected directly comparable models in the form of $\Lambda$CDM with $(\Omega_m, \Omega_\Lambda) = (0.3, 0.7)$ and Conformal Gravity with $q_0 = -0.55$, as per Equation (1.18). We fit these models to 182 'Gold' Type 1a SN [11] and two separate GRB data sets, with $H_0 = 71$ km s$^{-1}$ Mpc$^{-1}$. The SN data provide a low-redshift indicator with a range of $0.024 < z < 1.755$, the lower bound having been imposed [11] to remove the adverse effect of peculiar velocities, which strongly distort the Hubble diagram on small scales. Figure 3.3 shows the large scatter of these low redshift SN around the Hubble diagram for $\Lambda$CDM with $(\Omega_m, \Omega_\Lambda) = (0.3, 0.7)$.
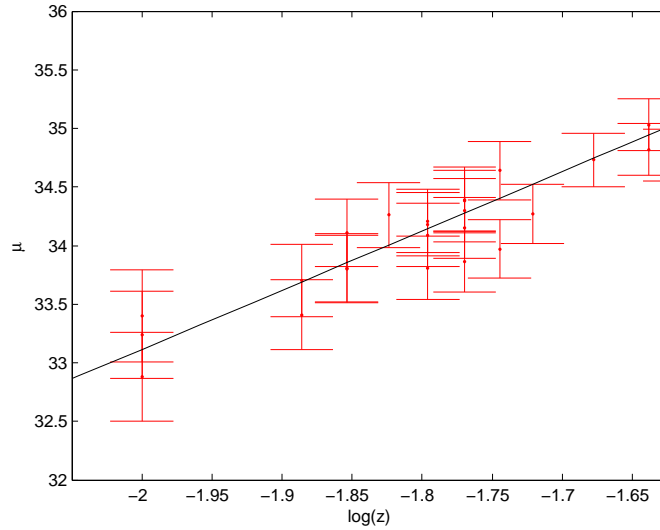


Figure 3.3: The 22 low redshift Supernovae with $z < 0.024$ that are removed from the 'Gold' sample [11] to avoid introducing a bias due to peculiar velocities. The black line is the Hubble diagram for $\Lambda$CDM with $(\Omega_m, \Omega_\Lambda) = (0.3, 0.7)$, included to illustrate that the low-$z$ SN are scattered randomly, as opposed to the a systematic over- or underestimation of the distance modulus. The digitisation of the data along the x-axis is simply an effect due to the scale and has no bearing on the utilised cut criterion.

The GRB data sets span the range $1.685 < z < 3.198$, thus providing a significantly deeper probe of the relationship between redshift and luminosity distance. The first set consists of 19 GRBs compiled by Friedman and Bloom [47] and the second is a subset containing 17 of these GRBs and utilised in Xu et al. [43]. These data sets are given in Tables 3.1 and 3.2, respectively.

| GRB | $z$ | $E_p(\sigma_{E_p})$ (keV) | $S_\gamma\ (\sigma_{S_\gamma})$ ($10^{-6}$ergs cm$^{-2}$) | $t_j(\sigma_{t_j})$ | $n(\sigma_n)$ | $\eta$ |
|---|---|---|---|---|---|---|
| 970508 | 0.8349 | 79.0(23.0) | 1.8(0.3) | 25.0(5.0) | 10.0(5.0) | 0.2 |
| 970828 | 0.9578 | 297.7(59.5) | 96.0[9.6] | 2.2(0.4) | 10(5) | 0.2 |
| 980703 | 0.966 | 254.0(51.0) | 22.6[2.26] | 3.4(0.5) | 28.0(10.0) | 0.2 |
| 990123 | 1.600 | 781.0(62.0) | 300.0(40.0) | 2.04(0.46) | 10(5) | 0.2 |
| 990510 | 1.619 | 161.5(16.0) | 19.0(2.0) | 1.57(0.03) | 0.29(0.14) | 0.2 |
| 990705 | 0.8424 | 188.8(15.2) | 75(8.0) | 1.0(0.2) | 10(5) | 0.2 |
| 990712 | 0.4331 | 65.0(10.5) | 11.0(0.3) | 1.6(0.2) | 10(5) | 0.2 |
| 991216 | 1.020 | 317.3(63.4) | 194.0[19.4] | 1.2(0.4) | 4.7(2.8) | 0.2 |
| 011211 | 2.140 | 59.2(7.6) | 5.0[0.5] | 1.56(0.02) | 10(5) | 0.2 |
| 020124 | 3.200 | 120.0(22.6) | 8.1[0.81] | 3.0(0.4) | 10(5) | 0.2 |
| 020405 | 0.69 | 192.5(53.8) | 74.0[0.7] | 1.67(0.52) | 10(5) | 0.2 |
| 020813 | 1.255 | 212.0(42.0) | 97.87(1.27) | 0.43(0.06) | 10(5) | 0.2 |
| 021004 | 2.332 | 79.8(30.0) | 2.55(0.6) | 4.74(0.14) | 30.0(27.0) | 0.2 |
| 021211 | 1.006 | 46.8(5.5) | 3.53(0.21) | 1.4(0.5) | 10(5) | 0.2 |
| 030226 | 1.986 | 97.1(20.0) | 5.61(0.65) | 1.04(0.12) | 10(5) | 0.2 |
| 030328 | 1.520 | 126.3(13.5) | 36.95(1.4) | 0.8(0.1) | 10(5) | 0.2 |
| 030329 | 0.1685 | 67.9(2.2) | 163.0(1.35) | 0.48(0.03) | 1.0(0.11) | 0.2 |
| 030429 | 2.658 | 35.0(9.0) | 0.85(0.14) | 1.77(1.0) | 10(5) | 0.2 |
| 041006 | 0.7160 | 63.0(13.0) | 7.0[0.7] | 1.56(0.09) | 10.0(5.0) | 0.2 |

Table 3.1: Data for 19 GRBs utilised by Friedmann and Bloom [47]. The fractional uncertainties are set by Friedmann and Bloom at 10% for $\sigma_{S_\gamma}$ and $n$ at $10.0 \pm 5$ cm$^{-3}$ if not otherwise reported in the literature. These instances are marked with square brackets.

| GRB | $z$ | $E_p(\sigma_{E_p})$ (keV) | $S_\gamma\ (\sigma_{S_\gamma})$ ($10^{-6}$ergs cm$^{-2}$) | $t_j(\sigma_{t_j})$ | $n(\sigma_n)$ | $\eta$ |
|---|---|---|---|---|---|---|
| 970828 | 0.9578 | 297.7[59.5] | 96.0[9.6] | 2.2(0.4) | 3.0[2.4] | 0.2 |
| 980703 | 0.966 | 254.0[51.0] | 22.6[2.26] | 3.4(0.5) | 28.0(10.0) | 0.2 |
| 990123 | 1.600 | 781.0(62.0) | 300.0(40.0) | 2.04(0.46) | 3.0[2.4] | 0.2 |
| 990510 | 1.619 | 161.5(16.0) | 19.0(2.0) | 1.57(0.03) | 0.29(0.14) | 0.2 |
| 990705 | 0.8424 | 188.8(15.2) | 75(8.0) | 1.0(0.2) | 3.0[2.4] | 0.2 |
| 990712 | 0.4331 | 65.0(10.5) | 6.5(0.3) | 1.6(0.2) | 3.0[2.4] | 0.2 |
| 991216 | 1.020 | 317.3[63.4] | 194.0[19.4] | 1.2(0.4) | 4.7(2.8) | 0.2 |
| 011211 | 2.140 | 59.2(7.6) | 5.0[0.5] | 1.56(0.02) | 3.0[2.4] | 0.2 |
| 020124 | 3.200 | 120.0(22.6) | 6.8[0.68] | 3.0(0.4) | 3.0[2.4] | 0.2 |
| 020405 | 0.69 | 192.5(53.8) | 74.0(0.7) | 1.67(0.52) | 3.0[2.4] | 0.2 |
| 020813 | 1.255 | 212.0(42.0) | 102.0[10.2] | 0.43(0.06) | 3.0[2.4] | 0.2 |
| 021004 | 2.332 | 79.8(30.0) | 2.55(0.6) | 4.74(0.14) | 30.0(27.0) | 0.2 |
| 021211 | 1.006 | 46.8(5.5) | 2.17(0.15) | 1.4(0.5) | 3.0[2.4] | 0.2 |
| 030226 | 1.986 | 97.1(20.0) | 5.61(0.65) | 1.04(0.12) | 3.0[2.4] | 0.2 |
| 030328 | 1.520 | 126.3(13.5) | 36.95(1.4) | 0.8(0.1) | 3.0[2.4] | 0.2 |
| 030329 | 0.1685 | 67.9(2.2) | 110.0(10.0) | 0.48(0.03) | 1.0(0.11) | 0.2 |
| 030429 | 2.658 | 35.0(9.0) | 0.8540(0.14) | 1.77(1.0) | 3.0[2.4] | 0.2 |

Table 3.2: Data for 17 GRBs utilised by Xu et al. [43]. Square brackets round an error quantity indicate the value was not published in the original GRB data. In these cases, Xu et al. have fixed the fractional uncertainties at 20% for $E_p$ and 10% for $\sigma_{S_\gamma}$. Likewise, Xu et al. have fixed the circumburst densities $n$ at $3.0 \pm 2.4$ cm$^{-3}$ if not otherwise reported.

In addition to discarding 2 events, GRB041006 and GRB970508, in the second compilation estimates of $n$ and its associated error $\sigma_n$ have been reduced from $10 \pm 5$ cm$^{-3}$ to $3 \pm 2.4$ cm$^{-3}$. Xu et al. justify this assumption by citing earlier similar assumptions by Ghirlanda et al. [36] and references therein that suggest a range for the circumburst density of $n \sim 1 - 10$ cm$^{-3}$. Changing $n$ by this degree results in a reduction $\mathcal{O}(15\%)$ of the jet opening angle $\theta$, given by Equation (2.16), a not insignificant difference and a small insight into the sensitivity of the relation to input parameter assumptions discussed in §3.1.1.

| | $\chi^2_{\mathrm{SN+GRB}}$ | $\chi^2_{\mathrm{GRB}}$ | $\chi^2_{\mathrm{GRB}}/d.o.f.$ |
|---|---|---|---|
| $\Lambda$CDM | 183.31 | 21.45 | 1.13 |
| CG | 266.72 | 25.90 | 1.36 |

| | $\chi^2_{\mathrm{SN+GRB}}$ | $\chi^2_{\mathrm{GRB}}$ | $\chi^2_{\mathrm{GRB}}/d.o.f.$ |
|---|---|---|---|
| $\Lambda$CDM | 170.62 | 8.76 | 0.52 |
| CG | 250.93 | 10.12 | 0.59 |

Table 3.3: $\chi^2$ values for $\Lambda$CDM and Conformal Gravity (CG), evaluated with Friedman and Bloom's 19 GRBs (left), Xu et al.'s 17 GRBs (right) and 182 'Gold' Type 1a SN.

Table 3.3 shows the results of evaluating the $\chi^2$ statistic for $\Lambda$CDM and Conformal Gravity with each of these data sets, both combined with and independently of the SN data. We also include the reduced $\chi^2$ per degree of freedom for standard comparison with both data sets. It should be noted that the SN distance modulus data must be scaled in accordance with the selection of $H_0$ [11].

### 3.1.3 Conclusions

The original motivation behind this work was an investigation into the viability of an alternative to the concordance model in the shape of Conformal Gravity. In order to do this it was essential to implement a new class of distance indicator at significantly higher redshifts than current Type 1a SN data. The specific prediction of the Conformal Gravity model that the Universe did not undergo a deceleration phase cannot be ruled out by the results presented in §3.1.2, as can be seen from the similar reduced $\chi^2$ values for both models. However, these results highlight two more important issues regarding the efficacy of GRBs as distance indicators.

The first is evident from the similar reduced $\chi^2$ values for both models. The GRB data are neither accurate enough nor numerous enough to discriminate

between models which accelerate and decelerate above $z = 1$. Indeed, until the significant errors in measured values are reduced and fewer estimates of non-measured values are made, it would appear that GRBs can add very little to a direct model comparison analysis. The second caveat concerns data selection and results obtained with data sets that may have been compiled in order to support the model in question. It is easy to justify including or discarding events from a data set that is already acknowledged as flawed. On comparing the reduced $\chi^2$ values between the two data sets presented in §3.1.2 it is clear that many GRB events may either be too inaccurate to be of use or do not fit the Ghirlanda Relation and have subsequently been discarded. Indeed, from several hundred currently detected GRB events, to utilise less than 20 of these suggests major shortcomings in the data.

Should the data improve in the future and the Ghirlanda Relation be consistently supported, it may be possible to use GRBs to constrain cosmological parameters. However, the current lack of reliable data is only one cause for concern. We now go on to describe in detail another.

## 3.2   Calibration Issues

In early work based on the Ghirlanda Relation [36], the correlation parameters $a$ and $C$ appearing in Equation (2.19) were globally constrained for a given data set by selecting the values that minimised the scatter in the $E_p - E_\gamma$ relation. However, a fixed cosmological model was used when evaluating the collimation-corrected burst energy $E_\gamma$ for each GRB i.e. the luminosity distance $d_L$ in Equation (2.17) was calculated *assuming* $(\Omega_m, \Omega_\Lambda) = (0.3, 0.7)$. As highlighted in many subsequent publications on this issue (see for example [47]), and as will be discussed further below, no meaningful conclusions can then be drawn on other combinations of $(\Omega_m, \Omega_\Lambda)$. This issue has subsequently been addressed in later work [54], [55], [43] by re-calibrating the relation by obtaining the best-fit Ghirlanda Relation parameters $a$ and $C$ for each combination of $(\Omega_m, \Omega_\Lambda)$. However, we have identified another source of systematic bias within the construct of the Ghirlanda Relation.

### 3.2.1 When Maximum Likelihood Does Not Equal Minimum $\chi^2$

As outlined in §2.4.1, cosmological parameter estimation techniques generally involve calculating the goodness of fit of a data set to a given model. This is achieved by identifying the position in the parameter space at which the likelihood is maximal – in ordinary circumstances, as outlined in §2.4.1, this is coincident with minimising the $\chi^2$-statistic, given by Equation (2.30). More specifically, the positions of minimum $\chi^2$ and maximum likelihood will be coincident provided that the likelihood is a normal distribution. However, in the case of GRB data this assumption is not valid because the error $\sigma_{E_\gamma}$, given by Equation (2.21), is dependent on the cosmological parameters through $\theta$, $E_{iso}$ and hence the predicted luminosity distance $d_L$. The likelihood function $L$ is therefore a function of the observed and predicted distance moduli and hence underlying cosmological parameters $(\Omega_m, \Omega_\Lambda)$, and can be expressed as

$$L(\Omega_m, \Omega_\Lambda) = \prod_{i=1}^{n} \frac{1}{\sqrt{2\pi}\sigma_i(\Omega_m, \Omega_\Lambda)} \exp\left[-\frac{1}{2}\chi^2(\Omega_m, \Omega_\Lambda)\right]. \qquad (3.1)$$

The effect of this parameter dependence can then be seen most clearly by examining the log-likelihood, noting the dependence of $\sigma(\Omega_m, \Omega_\Lambda)$

$$\ln L(\Omega_m, \Omega_\Lambda) = -\frac{n}{2}\ln(2\pi) - \sum_{i=1}^{n} \ln \sigma_i(\Omega_m, \Omega_\Lambda) - \frac{1}{2}\chi^2. \qquad (3.2)$$

The presence of the second term on the right hand side results in the location of $\chi^2_{min}$ no longer being coincident with $L_{max}$ in the parameter space. In addition to this, the shape of the likelihood across the $(\Omega_m, \Omega_\Lambda)$ plane will be altered. This will result in standard confidence intervals, computed under the assumption of normality as discussed in §2.4.1, also being misidentified. This is because the selection criteria of $\Delta\chi^2 = 2.3, 6.17, 11.8$ no longer containing 68%, 95% and 99% of the likelihood function, as discussed in §2.4.1.

### 3.2.2 Construction of a Toy Model

The neglect of the parameter dependence of the 'observed' distance modulus errors when obtaining 'best-fit' cosmological parameters can be illustrated with

a toy model that is representative of the issue in question – i.e. a two-parameter model with errors on the 'observed' quantity also dependent on the parameters being estimated. Consider a simple model characterised by two parameters $a$ and $b$, such that $\sigma_{obs} = \sigma_{obs}(a, b)$. We take the degree of variation in $\sigma_{obs}$ across the $(a, b)$-parameter space to be of a similar level to the case of the real GRB data from Xu et al. [43], shown in Fig. 3.4 and Table 3.4.
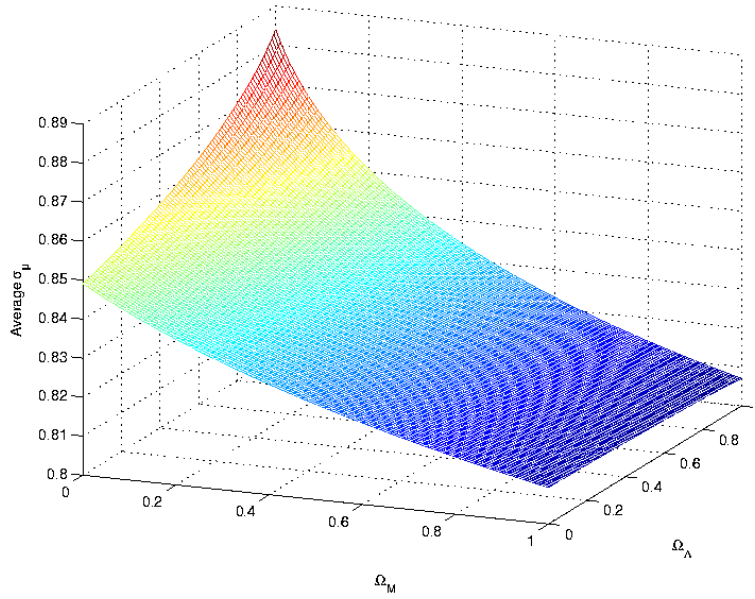


Figure 3.4: Variation in the average value of $\sigma_\mu$ for the 17 GRBs published in Xu et al. across the $(\Omega_m, \Omega_\Lambda)$ plane, as a fraction of $\sigma_\mu^{max}$.

The data are constructed by initially fixing the parameter values $(a_{true}, b_{true})$ and generating 'observed' values such that

$$y_i^{obs} = y_i^{pred} + \epsilon_i \qquad \text{where} \qquad \epsilon_i \sim \mathrm{N}[0, \underbrace{\sigma(a_{true}, b_{true})}_{\sigma_{true}}]. \qquad (3.3)$$

The 'predicted' values are also model dependent: $y_i^{pred} = ax_i + b$ and $x_i \sim \mathrm{N}[0, 1]$ and the 'observational' error in $y_i^{pred}$ is modelled as a combination of the known 'true' value and an additional term that is parameter-dependent

$$\sigma(a, b) = \sigma_{true} + \Delta\sigma; \qquad \Delta\sigma = \kappa\sqrt{(a - a_{true})^2 + (b - b_{true})^2}. \qquad (3.4)$$

The degree of dependence on $(a, b)$ can then be scaled by choosing $\kappa$. We pick $\kappa = 0.1$ as $\sigma(\Omega_m, \Omega_\Lambda)$ varies by $\sim 10\%$, evident in Fig. 3.4.

| GRB    | $\sigma_{\mu_{max}}$ | $\sigma_{\mu_{min}}$ |
|--------|----------|----------|
| 970828 | 0.853    | 0.922    |
| 980703 | 0.773    | 0.849    |
| 990123 | 1.083    | 1.102    |
| 990510 | 0.640    | 0.668    |
| 990705 | 0.668    | 0.687    |
| 990712 | 0.587    | 0.649    |
| 991216 | 0.902    | 0.968    |
| 011211 | 0.575    | 0.618    |
| 020124 | 0.802    | 0.868    |
| 020405 | 0.891    | 1.010    |
| 020813 | 0.804    | 0.875    |
| 021004 | 0.100    | 1.184    |
| 021211 | 0.653    | 0.685    |
| 030226 | 0.730    | 0.812    |
| 030328 | 0.638    | 0.668    |
| 030329 | 0.392    | 0.400    |
| 030429 | 0.954    | 1.049    |

Table 3.4: Maximum and minimum values of $\sigma_\mu$ for each of the 17 GRBs in Xu et al.'s compilation [43]. $\sigma_\mu$ is dependent on the cosmological parameters and varies across the $(\Omega_m, \Omega_\Lambda)$ plane, as shown in Figure 3.4.

Therefore, we can now compare the parameter values calculated by both minimising $\chi^2$ and maximising $L$ and any discrepancy between these values vindicates our concerns about neglecting the parameter dependence of the errors associated with the model. In addition to this, it is also possible to illustrate the incorrect coverage of the confidence intervals that would be calculated by naïvely using the standard formula expressing them as a function of $\Delta\chi^2$.

### 3.2.3  Results

Within a *Frequentist* interpretation, the confidence intervals quoted with a result tell you how often, over many repeated measurements, you would expect the true parameter value(s) to lie within a certain interval. For example, over 100 data sets, we can expect that the parameter values will fall within the 99% confidence interval 99 times. The sample mean standard deviation $\sigma_m$ is calculated as [48]

$$\sigma_m = \frac{\sigma}{\sqrt{n}}, \tag{3.5}$$

where $n$ is the number of measurements in each sample drawn from the distribution and $\sigma$ is the standard deviation related to the confidence interval e.g. 68%

corresponds to a $1\sigma$ confidence interval. Figure 3.5 illustrates the 68% ($1\sigma$) confidence intervals on 20 independent samples of 10 measurements drawn from a Gaussian distribution of mean $\mu = 5$ and standard deviation $\sigma = 1$. For 20 samples, 13.6 (68%) of the intervals would be expected to include the value of the true mean. This is vindicated in Figure 3.5, where 13 of the intervals can be seen to encompass the true mean.
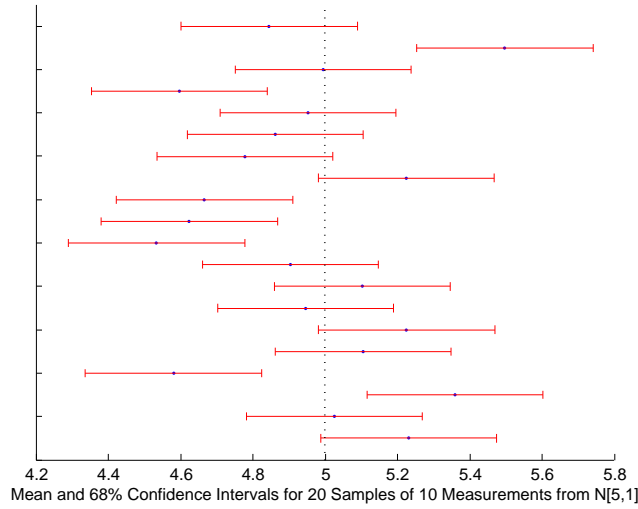


Figure 3.5: The mean and associated 68% ($1\sigma$) confidence intervals for 20 samples, each consisting of 10 measurements, drawn from a Gaussian distribution of mean $\mu = 5$ and standard deviation $\sigma = 1$ [48]. The 68% ($1\sigma$) confidence intervals are calculated as $\sigma_m = \sigma/\sqrt{n}$, where $n$ is the number of measurements. 13 of 20 intervals contain the true mean $\mu = 5$, with 13.6 the expected value.

Contrastingly, in a *Bayesian* framework, the credible regions describe a degree of belief about the values estimated using 1 data set e.g. to compute the 99% credible region for a parameter means that we compute the region for which our degree of belief is 99% that the parameter lies within – i.e. the region within which 99% of the posterior likelihood lies. This allows us to calculate the actual coverage of the incorrectly calibrated credible regions for our toy model by MCMC sampling the posterior pdf that has been calculated incorrectly through neglecting the full likelihood calculation, as outlined in §2.4.2. Furthermore, the *correct* credible regions can be evaluated by sampling the full likelihood function that correctly accounts for the parameter dependence of the errors in the construction of the toy model.
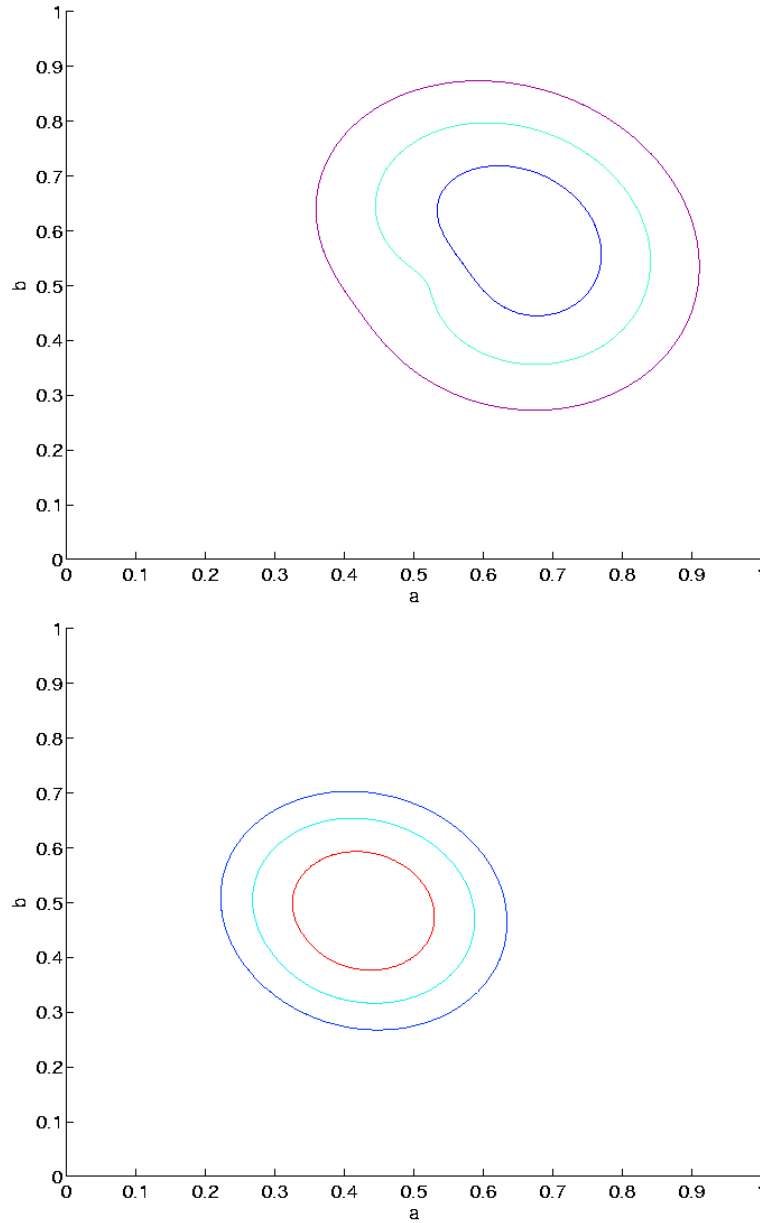
Figure 3.6: Incorrect $\Delta\chi^2$ contours (top) with associated covering factors of 0.15, 0.71 and 0.96. The correct maximum likelihood contours (bottom) by definition contain 68%, 95% and 99% of the likelihood function. The 'true' parameter values are $(a_{true}, b_{true}) = (0.5, 0.5)$ and the likelihood has been MCMC sampled 1000 times.

Figure 3.6 shows contour levels puportedly at 68%, 95% and 99%, calculated by minimising $\chi^2$, with associated coverage factors of 0.15, 0.71 and 0.96, strong evidence that these have been incorrectly identified when compared to expected values of 0.68, 0.95 and 0.99. The best fit parameter values have also been incorrectly identified as $(a, b) = 0.68, 0.57$ for $(a_{true}, b_{true}) = (0.5, 0.5)$. The bias can be seen more clearly in Figure 3.7, which shows the deviation of the minimum $\chi^2$ and maximum likelihood estimates from the true parameter val-
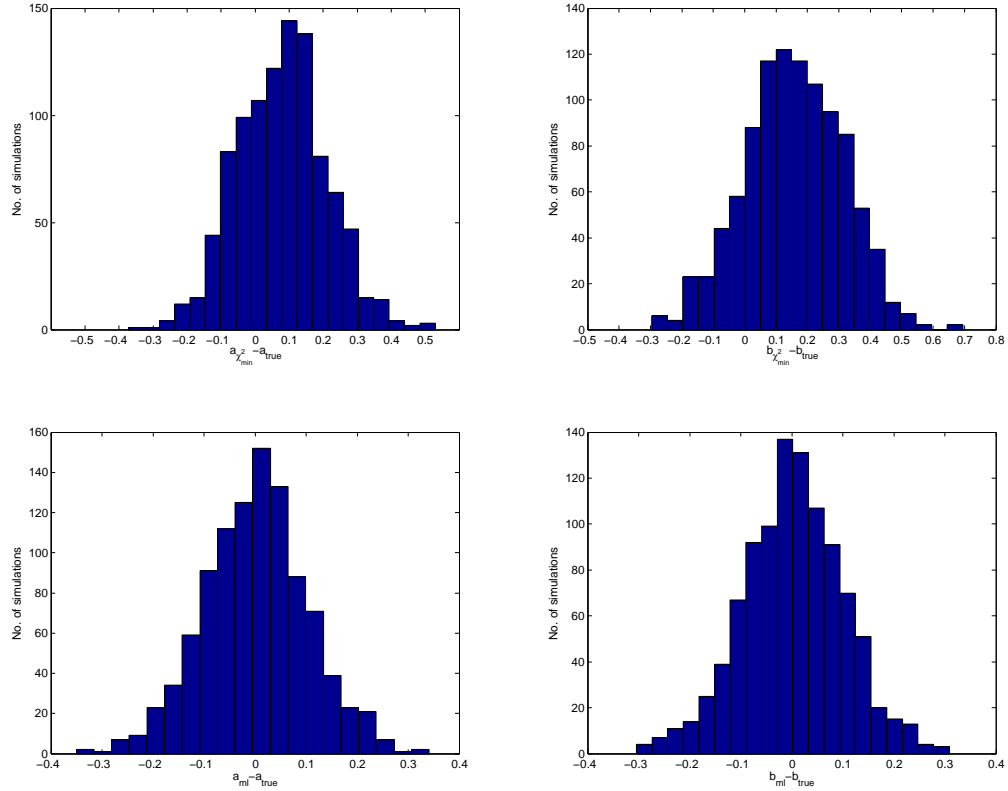
Figure 3.7: Histograms of 1000 MCMC simulations, showing the bias in estimating $(a_{true}, b_{true}) = (0.5, 0.5)$ introduced when only considering the $\chi^2_{min}$ criterion (top) compared with sampling the full likelihood (bottom). The bias from an expected deviation of 0 is $(a_{true}, b_{true}) - (a_{\chi^2_{min}}, b_{\chi^2_{min}}) = (0.113, 0.1569)$.

ues, over 1000 MCMC samples. Using the maximum likelihood method yields an estimation of the parameter values with no bias, in contrast with the $\chi^2_{min}$ method, which has a consistent bias, shown by a non-zero mean deviation of $(a_{true}, b_{true}) - (a_{\chi^2_{min}}, b_{\chi^2_{min}}) = (0.113, 0.1569)$.

The incorrect shape of the contour levels is also apparent when compared to those obtained by sampling the full likelihood, as can be seen by the slightly smaller and tighter correct credible regions.

### 3.2.4 Conclusions

Close examination of the statistical background of parameter estimation has brought to light a previously overlooked subtlety. The commonly relied upon assumption that the parameter combination yielding the minimum $\chi^2$ value is coincident with the maximum of the full likelihood breaks down when the error

term appearing in the likelihood calculation is dependent on the parameters being evaluated. Disregarding this fact leads to misidentification of both the favoured best-fit values of the parameters and the shape and location of the confidence intervals commonly invoked to lend support to any conclusions drawn from the analysis. Moreover, this misidentification will result in confidence intervals that do not have the correct frequentist coverage.

In the next chapter we go on to investigate the effect this oversight has on current GRB analysis in the literature and identify further cases of misapplication of statistical techniques. We will show that there is a distinct limit to what GRBs can lend to cosmological parameter estimation and demonstrate that so-called 'Bayesian' analysis techniques developed in recent literature are in fact incorrect.

# Chapter 4

# Current Statistical Techniques for Analysing GRB Data– What's Wrong, Why and How Should It Be Done?

When constructing and evaluating a statistic such as a goodness of fit test, it is advantageous to have as large a data set with as small errors as possible. However, as we have discussed previously, GRB data of this quality is not currently available. As such, it is essential to extract as much information as possible from the data of limited quality that is available. However, there are limits to what information any data set can yield and it is crucial to understand what these limits are. Further manipulation of the data beyond these limits can in fact result in misleading and incorrect results.

This chapter begins with a detailed examination of the statistical techniques that have been used in the current literature to calibrate GRBs as cosmological distance indicators, and a demonstration that these techniques are erroneous. We calculate the (frequentist) covering factors of the confidence regions obtained by following the published methodology and show that these do not agree with expected values. Having drawn a line under the maximum analysis one can perform with a data set subject to the specific limitations that afflict current GRB observations, we then go on to examine what might be achieved with GRBs in the future, should the data quality and quantity both improve and the specific circularity problem be overcome.

We present two methods for generating mock GRB data. The first provides

statistically similar data to that which is currently available in order to MCMC sample the likelihood function and calculate covering factors. The second method draws a required number of GRBs from a realistic redshift distribution [56] in order to illustrate the contribution GRBs *could* make, should the parameter-dependent errors be calibrated in the near future.

## 4.1 Incorrect Bayesian Analysis

The outline of the Ghirlanda Relation in §2.3.2 follows Xu et al.'s attempts to constrain cosmological parameters with 17 GRBs [43] and the initial stages of their analysis closely follows similar work by the instigators of the Ghirlanda Relation [36]. However, Xu et al. go on to present two additional algorithms for further constraining initial estimates of $(\Omega_m, \Omega_\Lambda)$, with reference to one similar method proposed by Firmani et al. [55]. Both of these algorithms build on an incorrect foundation, by wrongly assuming the coincidence in the parameter plane of $\chi^2_{min}$ and $L_{max}$, as previously illustrated in Chapter 3. However, even if the fundamental flaw of Method 1 was corrected by evaluating the full likelihood function, both Method 2 and Method 3 are inherently flawed due to a fundamental misuse of Bayesian inference methodology and should not be used as methods to estimate cosmological parameters.

### 4.1.1 Pulling Yourself Up By Your Own Bootstraps

As stated above, Xu et al. [43] outline three methods to constrain cosmological parameters using GRBs, each one 'improving' on the last. Figure 4.1 shows the published results for each of these methods.

The 'No Big Bang' area of the $(\Omega_m, \Omega_\Lambda)$ parameter space shown in Xu et al.'s results is a common prior included in estimations of cosmological parameters. The results we present in this section also include this restriction in the parameter space. The boundary marks all values of $(\Omega_m, \Omega_\Lambda)$ for which numerically integrating the Friedmann Equations (1.5) and (1.6) backwards in time does not result in the scale factor $R = 0$ (the Big Bang) or $dR/dt = 0$ (implying an oscillating universe), at some finite time in the past.

See reference in caption for image.

Figure 4.1: Xu et al.'s published constraints on $(\Omega_m, \Omega_\Lambda)$ for Methods 1, 2 and 3 respectively [43]. In all cases, the 68.3%, 90% and 99% contours have been incorrectly computed since the likelihood function has effectively been assumed to be Gaussian, ignoring the dependence of the 'observed' distance moduli and their quoted errors on $\Omega_m$ and $\Omega_\Lambda$. Methods 2 and 3 make further incorrect assumptions, as discussed in the text.

**Method 1**

The initial analysis method adopted by Xu et al. [43] is a straightforward $\chi^2$ goodness of fit test, accounting for the cosmology-dependent calibration of the Ghirlanda Relation by re-fitting $a$ and $C$ for each pair of parameters $(\Omega_m, \Omega_\Lambda)$. A

theoretical distance modulus for each GRB is compared with a derived observed value, both calculated for the same cosmology, following Equation (2.30)

$$\chi^2 = \sum_{i=1}^{n} \left( \frac{\mu_{pred,i} - \mu_{obs,i}}{\sigma_{\mu_{obs,i}}} \right)^2.$$  (4.1)

Xu et al. express this method as

$$P(\Omega_i) = P(\Omega_i | \Omega_i),$$  (4.2)

where $\Omega_i$ represents a given combination of $(\Omega_m, \Omega_\Lambda)$. This probability is evaluated across the whole parameter space, for all cosmologies.

However, this procedure that is commonly accepted and correctly utilised when using Supernovae as a distance indicator fails in the case of GRBs because currently the 'observed' distance moduli and their errors, as fitted from the GRB data, are also dependent on the cosmology, as outlined in Chapter 3. As was also shown in Chapter 3, this failure can however be corrected by evaluating the full posterior likelihood function, properly accounting for the fact that it will not be Gaussian, as was effectively assumed by Xu et al. [43].

**Method 2**

Xu et al. go on to propose what is (in their view) a Bayesian approach to defining a new distance indicator by attempting to construct a likelihood for the cosmological model $\Omega_j$ that is a weighted sum of likelihoods over the all other cosmologies $\Omega_i$. Xu et al. express this (confusingly) as

$$P(\Omega_j) = \sum_i P(\Omega_j | \Omega_i).$$  (4.3)

So, to be more specific, in this case Method 1 is applied over the parameter space to give a posterior probability for each cosmology $\Omega_j$. However, each of these probabilities $P(\Omega_j)$ is then in turn compared with every other $P(\Omega_i)$ by constructing a pseudo-$\chi^2$ statistic that is summed both over the data set for each $\Omega_j$ and the entire parameter space for each $\Omega_i$

$$\chi^2(\Omega_j) = \sum_i \frac{\mu_{pred}(\Omega_j) - \mu_{obs}(\Omega_i)}{\sigma_{\mu_{obs}}(\Omega_i)}.$$  (4.4)

Xu et al. argue that summing over all $\Omega_i$ for each $\Omega_j$, the conditional probability $P(\Omega_j|\Omega_i) \propto \exp\left[-\chi^2(\Omega_j|\Omega_i)/2\right]$ is marginalised to $P(\Omega_j) \propto \sigma_i \exp\left[-\chi^2(\Omega_j|\Omega_i)/2\right]$. The supposed $\chi^2$ statistic in Equation (4.4) is ill-posed as it does not compare like-for-like: data for cosmology $\Omega_i$ is fitted to a model $\Omega_j$. It certainly does not follow, therefore, that the expectation value of $\chi^2(\Omega_j)$ will equal the number of data points $n_{GRB}$, as it should if this pseudo-$\chi^2$ were to be interpreted in the normal way. Indeed, this is a similar problem to the original issue surrounding the need to re-calibrate the Ghirlanda Relation for each cosmology: 'observed' distance moduli obtained by assuming a fixed cosmology were being fitted to predicted distance moduli for varying cosmologies.

**Method 3**

In an attempt to further improve on Method 2, Xu et al. continue their misapplication of Bayesian inference by assigning a prior to Method 2. This prior is initially uniform across all pairs of values $(\Omega_m, \Omega_\Lambda)$ and is 'updated' after each iteration of Method 2 i.e. the posterior for iteration $n$ is implemented as the prior for iteration $(n+1)$ until the probability converges "after tens of cycles", such that

$$P^{(n+1)}(\Omega_j) = \sum P(\Omega_j|\Omega_i)P^{(n)}(\Omega_i). \tag{4.5}$$

In Bayesian terms, Method 3 amounts to calculating a posterior probability (via Methods 1 and 2) but then applying that posterior as a new prior to the original likelihood function *without adding any new data*. In this way, one might say that Xu et al. are trying to "pull themselves up by their own bootstraps". The result of this iterative procedure will always produce a tighter constraint on the original best fit parameters obtained from the first iteration, as the new prior will already favour that model.

It is straightforward to demonstrate that sequential updating of a posterior is acceptable, provided at least one new datum is added upon each iteration. Indeed, the final result is (and must be) the same for sequential analysis of data compared with computing the posterior for the whole data set in a single step. This is best illustrated by considering the straightforward analysis of sequential coin tosses, in a bid to determine if there is any bias [57].

Consider $N$ flips of a coin, the results of which are data set $\{D_k\}$, where $k = 1, \ldots, N$. We can construct the posterior pdf for the bias $H$, where $H \in [0, 1]$ and $H = 0.5$ indicates an unbiased coin, from Bayes' Theorem given in Equation (2.24), as

$$p(H|\{D_k\}, I) \propto p(\{D_k\}|H, I) \times p(H|I) \qquad (4.6)$$

For a data set of 2 data points, for example, Equation (4.6) would be

$$p(H|D_2, D_1, I) \propto p(D_2, D_1|H, I) \times p(H|I) \qquad (4.7)$$

However, if the data were instead analysed sequentially, the result of the first coin toss would become 'prior information' and the posterior pdf after the second coin toss would be

$$p(H|D_2, D_1, I) \propto p(D_2|H, D_1, I) \times p(H|D_1, I) \qquad (4.8)$$

However, assuming the data are independent – given $H$, the outcome of any coin toss does not influence subsequent results – the likelihood $p(D_2|H, D_1, I)$ is in fact independent of $D_1$ i.e.

$$p(D_2|H, D_1, I) = p(D_2|H, I) \qquad (4.9)$$

Equation (4.8) is therefore identical to Equation (4.7). This holds for all $\{D_k\}$ and shows that the posterior pdf can indeed be utilised as a prior for further analysis on the condition that *new data are added*. However, Xu et al. use the same data each time, hence violating this condition.

The effect of this misapplication of Bayes' Theorem is illustrated in Figure 4.2. A uniform prior is combined with a Gaussian likelihood function to produce the correct posterior distribution. The likelihood in the second iteration is the same as in the first, as it originates from the same data set. The posterior from the first step is then applied as a prior on this same likelihood function, which can only serve to tighten the constraint on the original posterior. Subsequent iterations would only serve to further compound the misuse of Bayesian methods and renders any published results employing any of these methods completely incorrect.
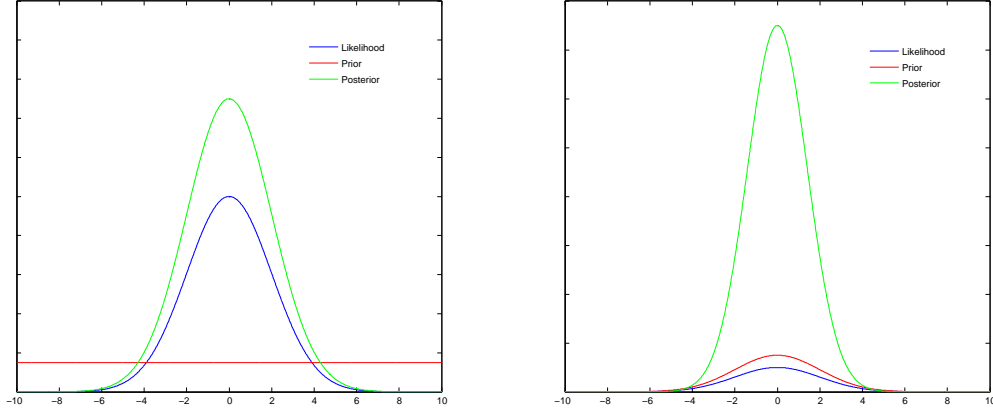
Figure 4.2: The posterior is calculated from the product of the prior and likelihood functions. The correct result for a Gaussian likelihood and uniform prior (left) contrasts with the incorrect second iteration, using the previously calculated posterior as the new prior without the addition of any new data (right).

## 4.2 Generating Statistically Similar GRB Data

As we have previously demonstrated, calculating the correct covering factors and identifying correctly defined confidence regions requires evaluation of the full likelihood, which can be accomplished using MCMC sampling. However, as outlined in §2.4.2, we require a sufficiently large number of maximum likelihood evaluations in order provide a representative sample of the posterior distribution. As a single data set provides a single maximum likelihood estimate of the model parameters, we therefore require many data sets. Unfortunately, we are provided with only one Universe and one set of GRB data. In order to investigate the statistical properties of Xu et al.'s procedures for generating confidence intervals, it is therefore necessary to generate samples that statistically mimic the real GRB data based on the observables and their uncertainties published in the literature. We now describe a method for generating 'mock' GRB samples for this purpose.

### 4.2.1 MCMC Sampling Observables

For each GRB observed, there are four relevant observables: the redshift $z$, jet-break time $t_j$, peak spectral energy $E_p$ and fluence $S_\gamma$. The more observables that are fixed, the closer the MCMC sample will mimic the real data. However, if all four observables were fixed, we would recover exactly the same $\mu_{obs}$ values as those

inferred for the real GRB data, thus negating the exercise. Some randomness must therefore be introduced to at least one of these four observables, and possibly to all of them. Providing our statistical model for the scatter in each observable is correct, the resultant MCMC samples will be statistically equivalent. Samples can be generated straightforwardly with the same intrinsic scatter in the $E_p - E_\gamma$ relation, which means that our mock GRB distance estimates should have the same precision as the real GRB data. However, data can also be generated for an $E_p - E_\gamma$ with smaller scatter. This will allow us to quantify the improvement that a possible future Ghirlanda Relation with a smaller intrinsic scatter might bring to constraining cosmological parameters.

## Case 1: Sampling With the $E_p - E_\gamma$ Scatter Equal to the Real Scatter

The minimal level of randomness that can be introduced is by generating mock data for only one observable and fixing the other mock observables as equal to their real observed values. We consider here the case where that observable is the fluence $S_\gamma$. For each GRB, our model for the scatter on $S_\gamma^{obs}$ is Gaussian, with standard deviation $\sigma_{S_\gamma}$ equal to the value published for that GRB. For each mock GRB we can then generate a value for $S_\gamma^{MC}$ drawn from a Gaussian distribution of mean $S_\gamma^{obs}$ and variance $\sigma_{S_\gamma}^2$ such that

$$S_\gamma^{MC} \sim \mathrm{N}\left[S_\gamma^{obs}, \sigma_{S_\gamma}^2\right],$$

and the other 3 variables $z$, $t_j$ and $E_p$ are set to be equal to their observed values in the real GRB data set. Alternatively, Gaussian noise can also be added to $t_j$ and $E_p$ such that

$$t_j^{MC} \sim \mathrm{N}\left[t_j^{obs}, \sigma_{t_j}\right]$$
$$E_p^{MC} \sim \mathrm{N}\left[E_p^{obs}, \sigma_{E_p}\right].$$

In either case, the mock data are then fitted to obtain a slope and zero point for the Ghirlanda Relation as outlined in §2.3.2. The fitted Ghirlanda Relation for the mock data can then be used to infer $\mu_{obs}$ exactly as before. As the redshift is independent of the event and is ascertained from the host galaxy, usually with

very small observational error, the redshift value for each mock GRB is kept equal to its corresponding real value.

This basic procedure can then be used to generate as many different, but statistically similar, data sets as required. Our MCMC sampling procedure can then be applied to these mock data sets in order to identify the correct Bayesian credible regions, taking proper account of the full likelihood function. However, as the likelihood function is not Gaussian, these Bayesian credible regions will still not correspond to the frequentist covering factors, as we go on to illustrate in §4.3.2.

### Case 2: Varying the $E_p - E_\gamma$ Scatter

Data sets with a reduced scatter around the best fit Ghirlanda Relation can also be obtained while keeping the slope and zero-point equal to those derived from the real data. This is achieved by calculating the 'observed' fluence values that would produce a specified $E_p - E_\gamma$ relation of given scatter, effectively backward-engineering the problem. Central to this method is first selecting a cosmology from which to draw the mock data. As a consequence, the best-fit parameter values are pre-determined and the principal outcome of interest is the effect on the confidence regions resulting from reducing the $E_p - E_\gamma$ scatter.

The Ghirlanda Relation can be calibrated for any selected cosmology, identifying the best-fit values for $a$ and $C$ in Equation (2.19). Following Xu et al. [43], and utilising the Numerical Recipes *'fitexy'* program [49], adopting a flat universe with $(\Omega_m, \Omega_\Lambda) = (0.27, 0.73)$ yields values of the gradient and intercept $a = 1.53 \pm 0.0765$ and $\log C = 0.97 \pm 0.0776$ respectively. Alternatively, the best-fit values can be calculated from the real data for any other selected cosmology.

Given the best-fit values for $a$ and $C$, a predicted $\log E_\gamma$ is then calculated for each GRB from this best fit line, using the published value of $E_p$. The desired intrinsic scatter in the $E_p - E_\gamma$ relation can then be simulated by adding Gaussian noise to the predicted value of $E_\gamma$. The scatter in the Ghirlanda Relation inferred for the real data can be recreated by generating a mock value $E_\gamma^{MC} \sim \mathrm{N}\left[E_\gamma^{\mathrm{PRED}}, \sigma_{E_\gamma}\right]$, where $\sigma_{E_\gamma}$ is given by Equation (2.21). Alternatively, a smaller value of $\sigma_{E_\gamma}$ can be adopted, which allows us to investigate the influence that

better data would have on the cosmological fits.

Rearranging Equation (2.18) and using the small-angle approximation $\cos\theta \simeq 1 - \theta^2/2$ (for $\theta \ll 1$) yields an expression for $E_\gamma$ as a function of $E_{iso}$ and $\theta$

$$E_{iso} = \frac{E_\gamma}{(\theta^2/2)}. \tag{4.10}$$

Combining this equation with the original expression for $\theta$ given in Equation (2.16) yields an expression for $\theta$ that is independent of $E_{iso}$

$$\theta = \left[0.163 \left(\frac{t_j}{1+z}\right)^{3/8} \left(\frac{n_0 \times 10^{52}}{2E_\gamma}\right)^{1/8} \left(\frac{\eta_\gamma}{1-\eta_\gamma}\right)^{1/8}\right]^{4/3}. \tag{4.11}$$

Then $E_{iso}^{\mathrm{TRUE}} \simeq 2E_\gamma^{\mathrm{TRUE}}/\theta^2$. The fluence value that our mock GRB would have, assuming the 'true' cosmological model that we have adopted, is then calculated from Equation (2.17) such that

$$S_\gamma^{\mathrm{TRUE}} = \frac{E_{iso}(1+z)}{4\pi d_L^2}, \tag{4.12}$$

where $d_L^2$ is the 'true' luminosity distance given from the observed redshift and Equation (2.6) as before.

We now have a list of observables $z$, $t_j$, $E_p$ and $S_\gamma$ for one data set that will give any desired best fit Ghirlanda Relation, with an arbitrarily specified scatter, for a known cosmology. Therefore, in order to produce many statistically similar data sets, suitable for e.g. MCMC sampling, $S_\gamma^{MC} \sim \left[S_\gamma^{\mathrm{TRUE}}, \sigma_{S_\gamma}\right]$ can be generated as previously outlined in Case 1.

## 4.3   Results

Although it has been important to outline the methodological flaws behind Xu et al.'s and other published analysis of GRB data, it is perhaps more illustrative to quantify the effect of these inaccuracies on the published numbers, and to then apply correct Bayesian methods to the data.

### 4.3.1   Incorrect Covering Factors

In order to investigate systematic biases in the reported best fit values of the cosmological parameters, and the confidence regions in the $(\Omega_m, \Omega_\Lambda)$ plane, pub-

| CF       | 0.683 | 0.954 | 0.9973 |
|----------|-------|-------|--------|
| Method 1 | 0.372 | 0.781 | 0.9749 |
| Method 2 | 0.151 | 0.663 | 0.9890 |

Table 4.1: Actual covering factors for Methods 1 and 2, for 10000 MCMC samples of the incorrect likelihood function. These differ greatly from the expected values defined by 1, 2 and $3\sigma$ of 0.683, 0.954 and 0.9973 respectively, hence revealing the inaccuracies in the so-called Bayesian analysis of Xu et al.

lished by Xu et al. it is instructive to calculate the actual covering factors for each of Methods 1 and 2.

We have not included covering factors for Method 3 as it is a subjective decision as to how many iterations to perform, thus the results will vary every time. Table 4.1 lists the actual values in comparison to the theoretical values one would expect to get if the method was truly Bayesian.

## 4.3.2   Correct Method 1 Results

It is straightforward to correct Method 1 – recalibrate the Ghirlanda Relation for each cosmology and account for the full likelihood instead of just evaluating the $\chi^2$ statistic and computing confidence regions on the incorrect assumption that the likelihood is Gaussian. Following this correct procedure produces the contours shown in Figure 4.3 for 10000 MCMC samples. However, no further information can be extracted from the data and thus Method 1 is the limit of meaningful analysis.

It is instructive to also calculate the covering factors for the correctly defined Bayesian credible regions that have been calculated by sampling the full posterior likelihood function, as it illustrates an important difference between Bayesian and frequentist interpretations of coverage.

| CF                | 0.683 | 0.954 | 0.9973 |
|-------------------|-------|-------|--------|
| Corrected Method 1 | 0.549 | 0.893 | 0.9912 |

Table 4.2: Frequentist covering factors for 68%, 95.4% and 99.73% Bayesian credible regions of the posterior likelihood function. As the likelihood function is non-Gaussian, the frequentist confidence intervals and the Bayesian credible regions will not be equal.

Frequentist contours are drawn at levels of equal $\Delta\chi^2$ away from $\chi^2_{min}$. However, as we have demonstrated in §4.3.1, when the likelihood function is non-
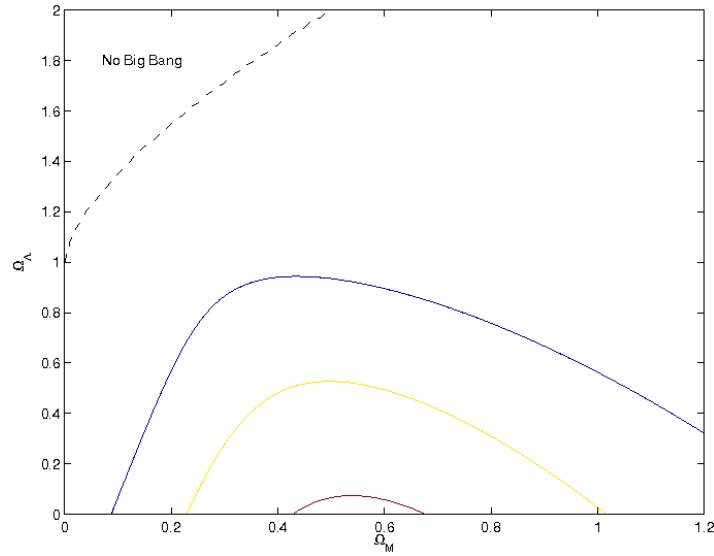
Figure 4.3: Contours at 68%, 95.4% and 99.73% plotted by calculating and MCMC sampling the full likelihood function for the 17 GRBs from Xu et al. [43]. It is clear that this data cannot provide meaningful constraints on cosmological parameters.

Gaussian these frequentist confidence regions are no longer consistent with the Bayesian interpretation of a credible region, which should contain a designated percentage of the likelihood function. By generating many data sets and counting the number of times the best-fit parameter values lie within the frequentist boundaries of confidence regions, we can calculate the discrepancy introduced between Bayesian and frequentist interpretations caused by non-Gaussian likelihood functions.

While the regions enclosed in Figure 4.3 do indeed contain 68%, 95.4% and 99.73% of the sampled likelihood, the frequentist covering factors, also shown in Table 4.2, are calculated as 0.549, 0.893 and 0.9912 – again showing deviations from the expected values. This further emphasises the incompatibility of frequentist and Bayesian interpretations. Indeed, we should never expect these different interpretations to provide the same results, except under the condition that there is a wide, uniform prior applied to a Gaussian likelihood [48]. The inclusion of the 'No Big Bang' prior and the likelihood function not being fully contained within the considered parameter space both serve to render the likelihood non-Gaussian before even considering the circularity issues [1].

---

[1]This has not been such a considerable concern for Type 1a Supernovae analysis as the area in the $(\Omega_m, \Omega_\Lambda)$ plane identified by the SN – and hence the likelihood function – is well contained within the parameter space.

### 4.3.3 Reducing the Scatter in the $E_p - E_\gamma$ Relation

As discussed in §4.2.1, it is of interest to investigate the constraints GRBs could place on cosmological parameters if the scatter in the Ghirlanda Relation could be reduced. As outlined in Case 2 of §4.2.1, the fake data is generated based on an assumed cosmology, thus the results should support the fiducial model. Figure 4.4 shows the constraints that could be achieved for a scatter equal to 75% of the current errors for data drawn from the Concordance cosmology of $(\Omega_m, \Omega_\Lambda) = (0.3, 0.7)$, with the contours being visibly tighter and closer to the true parameter values.
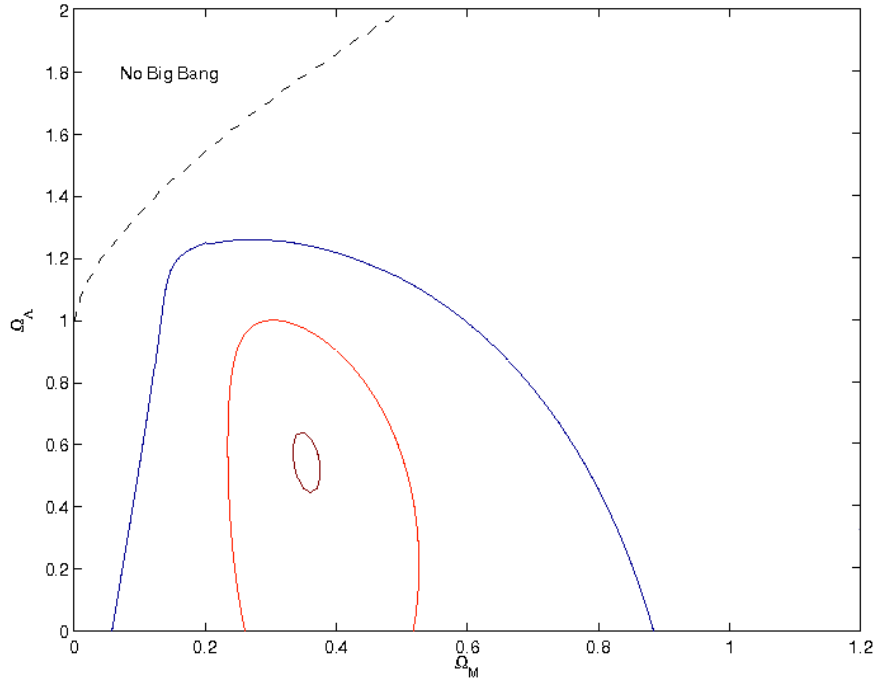


Figure 4.4: Constraints on $(\Omega_m, \Omega_\Lambda)$ for data drawn from a cosmology of $(\Omega_m, \Omega_\Lambda) = (0.3, 0.7)$, with the scatter in the Ghirlanda Relation reduced by 25%. By assuming a cosmology from which to draw mock data, the best-fit parameters are clearly pre-determined and identified accordingly. However, what is of interest is the tighter confidence regions due to the reduced scatter in the $E_p - E_\gamma$ relation.

### 4.3.4 Caveats and Conclusions

It is clear from Figure 4.3 that the constraints on $(\Omega_m, \Omega_\Lambda)$ obtained via our correct implementation of Method 1 are significantly different when compared with those published by Xu et al., shown in Figure 4.1. It also evident that current

GRB data, even when analysed correctly, do not provide a significant constraint on cosmological parameters. Indeed, although GRBs extend the existing Hubble Diagram of Type 1a Supernovae to significantly higher redshifts, the large published errors in the GRB data currently prevent any improvement in the parameter constraints provided by Supernovae. However, should issues with the Ghirlanda Relation be resolved in the near future, along with improvements in the data, Figure 4.4 shows what may be achieved.

Several issues regarding the misapplication of Bayesian statistics are raised in this work, such as mistakenly including frequentist interpretations within so-called Bayesian analysis. Drawing a contour at an interval $\Delta\chi^2$ from the minimum value of $\chi^2$ will only define a region that contains a percentage of the likelihood function *defined within that parameter range*. A truly representative Bayesian credible region can only be calculated by sampling the full likelihood and drawing boundaries that contain the required percentage of the posterior pdf.

As with all Bayesian statistics, there are many considerations that a frequentist may deem pedantic. However, the statistical regime of choice is increasingly turning towards Bayesian methods and one almost forms the impression that the term is often name-dropped in order to lend statistical gravitas to results. In this case, it is essential to ensure that the statistics employed are truly Bayesian, otherwise Bayesian Inference may come to be no longer be regarded with such high esteem.

## 4.4 Fiducial Models Using Mock GRB Data Sets

We have previously demonstrated in Chapter 3 that current data are neither accurate nor numerous enough to render GRBs as effective standard rulers. However, the volume and accuracy of the data is only going to increase, so one might hope that the situation will improve. In particular, it is hoped that sufficient nearby events will be detected so that the calibration issues previously discussed can be solved. These low redshift events would allow the determination of the intrinsic luminosity of a GRB event to be ascertained without having to consider the underlying cosmology, in a manner similar to Type 1a Supernovae. It is therefore

instructive to investigate the limitations of potential future data sets obtained over the remainder of the SWIFT mission.

### 4.4.1 Generating Mock GRB Redshift Data

When generating mock data sets it is necessary to reproduce a sample with a rate of detection representative of what would be expected in both the temporal and spatial distributions. Detection rate is dependent on several parameters, including the GRB event rate (linked to star formation rate), redshift range and detector efficiency and flux limit. Following Bertolami and Silva (2006) and references therein, the rate of GRBs observed with peak flux $P$ greater than flux limit $P_1$ in redshift range $(z, z + \mathrm{d}z)$ is

$$\mathrm{d}N(P \geq P_1) = \mathrm{d}z \frac{\mathrm{d}V(z)}{\mathrm{d}z} \frac{R_{GRB}(z)}{(1+z)} \int_{L(P_1,z)}^{\infty} \mathrm{d}L' \psi(L') \epsilon(P_1), \qquad (4.13)$$

where $\dfrac{\mathrm{d}V}{\mathrm{d}z}$ is the comoving volume of a shell per unit time in redshift range $(z, z + \mathrm{d}z)$, $R_{GRB}(z)$ is the number of GRBs per unit comoving volume per unit time in redshift range $(z, z + \mathrm{d}z)$, $\psi(L')$ is the luminosity function defined in Equation (4.21) and the integral over luminosity $L$ accounts for the fraction of occurring GRBs that are detectable, with $\epsilon(P_1) = 1$ representing an assumed 100% detector efficiency and $P_1 = 0.04$ photons cm$^{-2}$ s$^{-1}$ for SWIFT. This then allows us to compute the fraction of observed GRBs within the aforementioned limits as

$$\phi(z; P \geq P_1) = \frac{\frac{\mathrm{d}N}{\mathrm{d}z}(z; P \geq P_1)}{\int_0^{\infty} \frac{\mathrm{d}N}{\mathrm{d}z}(z; P \geq P_1)\mathrm{d}z}. \qquad (4.14)$$

The comoving volume [58] is given by

$$\frac{\mathrm{d}V_c}{\mathrm{d}z} = \frac{4\pi c}{H_0} \frac{(1+z)^2 D_A^2(z)}{E(z)}. \qquad (4.15)$$

The angular diameter distance $D_A(z) = D_M/(1+z)$ where

$$D_M(z) = \begin{cases} \frac{c}{H_0 \sqrt{\Omega_k}} \sinh\left(\sqrt{\Omega_k} \int_0^z \frac{\mathrm{d}z'}{E(z')}\right) & \text{for } \Omega_k > 0 \\ \frac{c}{H_0} \int_0^z \frac{\mathrm{d}z'}{E(z')} & \text{for } \Omega_k = 0 \\ \frac{c}{H_0 \sqrt{\Omega_k}} \sin\left(\sqrt{\Omega_k} \int_0^z \frac{\mathrm{d}z'}{E(z')}\right) & \text{for } \Omega_k < 0. \end{cases} \qquad (4.16)$$

We assume that the event rate $R_{GRB}(z)$ is proportional to the star formation rate $R_{SF}(z)$ where we take [56]

$$R_{SF}(z) = 0.15 \frac{H_0}{65} \frac{\exp(3.4z)}{\exp(3.4z) + 22} \ \mathrm{M}_\odot \mathrm{yr}^{-1}\mathrm{Mpc}^{-1}. \qquad (4.17)$$

The star formation rate in Equation (4.17) is calculated for an Einstein-de Sitter Universe, with $(\Omega_m, \Omega_\Lambda, H_0) = (1, 0, 65)$. Therefore, a conversion factor is required when considering other cosmologies

$$R_{GRB} \propto \frac{H(z|\Omega_m, \Omega_\Lambda, H_0)}{H(z|1, 0, 65)} R_{SF}, \qquad (4.18)$$

with non $z$-dependent terms dropping out as constants of proportionality. $H(z)$, the Hubble Constant at a given redshift and hence epoch, is given for an arbitrary Friedmann model by Equation (1.14).

Finally, we compute the fraction of detectable GRBs as a function of peak flux $P$ and redshift $z$ by integrating the normalised GRB Luminosity Function

$$L(P, z) = 4\pi D_c^2 P \frac{\int_{30}^{2000} E N(E) \mathrm{d}E}{\int_{E_L(1+z)}^{E_U(1+z)} N(E) \mathrm{d}E}, \qquad (4.19)$$

where $P$ is the peak flux observed in a band with lower and upper energies $E_L$ and $E_U$, scaled from the source to observer rest frame by $(1 + z)$, $D_C(z)$ is the comoving radial distance at redshift $z$ given by

$$D_C(z) = \frac{c}{H_0} \int_0^z \frac{\mathrm{d}z'}{E(z')}, \qquad (4.20)$$

and $N(E) = N_0 E^{-2.5}$ is the source spectral shape between $30 - 2000$ keV. The luminosity function appearing in the integral in Equation (4.13) is [56]

$$\psi(L) \propto \left(\frac{L}{L_0}\right)^\gamma \exp\left(-\frac{L_0}{L}\right), \qquad (4.21)$$

with $\gamma = -2.9$ and $L_0 = 7 \times 10^{51} (H_0/65)^{-2} \mathrm{erg \ s^{-1}}$. Thus, with an appropriate change to dimensionless variables of $l \equiv (L/L_0)$, the rate of observed GRBs can be calculated as

$$\frac{\mathrm{d}N}{\mathrm{d}z} \propto \frac{(D_M(z))^2}{E(z)} \frac{H(z|\Omega_m, \Omega_\Lambda, H_0)}{H(z|1, 0, 65)} \frac{1}{(1+z)} \int_{\Delta(P_1, z)}^\infty \mathrm{d}l \ l^\gamma \ e^{-1/l}. \qquad (4.22)$$

This allows us to construct the probability distribution function (pdf) to be sampled, given by Equation (4.14). The pdf is sampled by first constructing the corresponding cumulative distribution function (cdf)

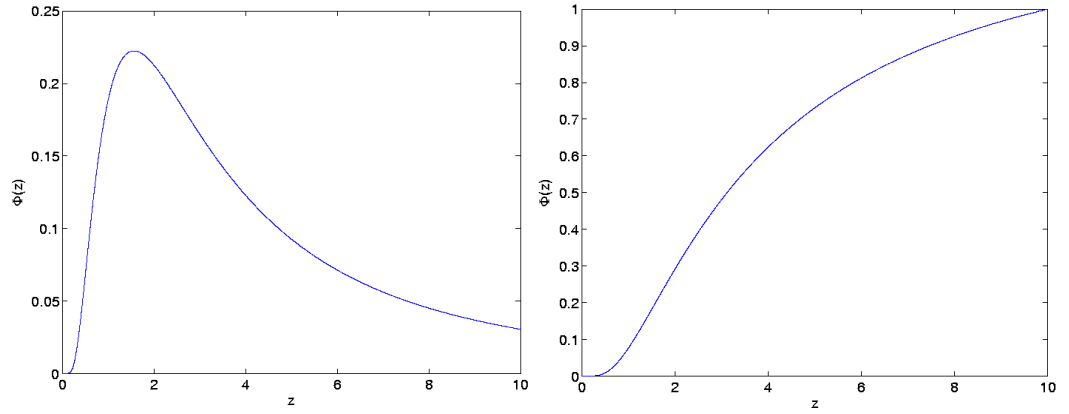$$\Phi(z) = \int_0^z \phi(z') \mathrm{d}z'. \qquad (4.23)$$

Figure 4.5: The analytical pdf $\phi$ (left) and corresponding cdf $\Phi$ (right) of the GRB redshift distribution, calculated for the redshift range $z \leq 10$ following Bertolami and Silva (2006).

The cdf is sampled by generating another random variable drawn from a uniform distribution i.e. $y \sim \mathrm{U}[0, 1]$ and determining the value $x$ satisfying $x = P^{-1}(y)$, thus the required sample is obtained, since $x \sim p(x)$ [49]. This approach allows a flexible sample to be generated of arbitrary size and redshift range. As an illustration, Figure 4.5 shows the analytical pdf and corresponding cdf with a histogram of a sample of 200 observable GRBs from redshift range $z \leq 10$ shown in Figure 4.6.
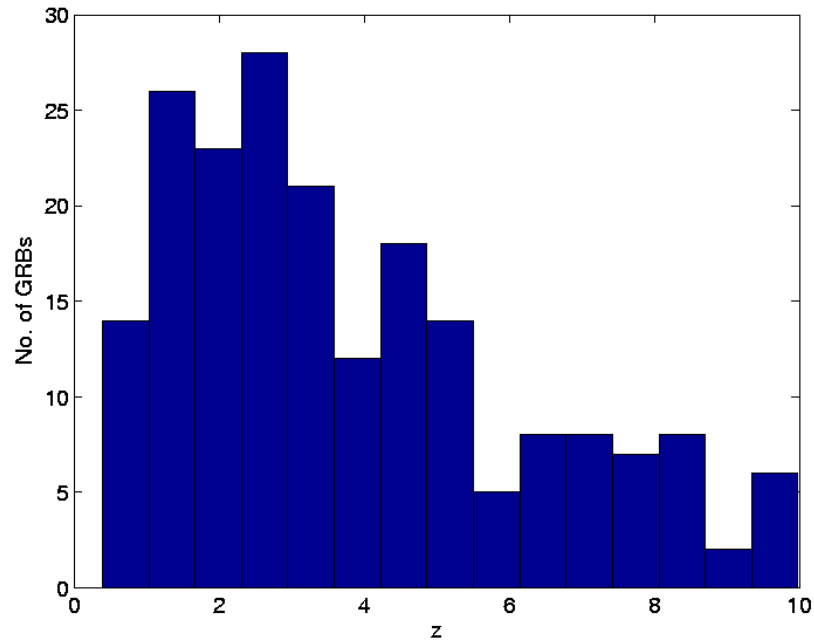


Figure 4.6: A sample histogram for 200 observable mock GRBs with redshift $z \leq 10$, drawn from the pdf outlined in Bertolami and Silva (2006).

## 4.4.2   The Fiducial Method for Model Comparisons

While we do not currently have detections of sufficiently low redshift GRBs to reliably calibrate any relations that could be used for the purpose of distance estimation, it is still useful to compare the viability of cosmological models using mock GRB data sets generated in the assumption that the distance modulus errors are fixed and no longer dependent on the cosmology. This is the main short-term goal for the field as a whole and it is therefore instructive to predict the potential impact reliable GRB data will have on cosmological model selection.

A simple and widely used method for evaluating the number of data points required to rule out a particular model involves comparing the desired model to a fiducial model and calculating the associated $\Delta\chi^2$-statistic

$$\Delta\chi^2 = \sum_i^{n_{grb}} \left[ \frac{\mu(z_i, \mathbf{p}_{\mathrm{fid}}) - \mu(z_i, \mathbf{p})}{\sigma_\mu} \right]^2, \tag{4.24}$$

where the parameter vector $\mathbf{p}_{\mathrm{fid}}$ defines the fiducial model and $\mathbf{p}$ defines the model with which we are comparing it. It should be noted that this is not a true $\chi^2$-statistic, as it involves model predictions and not actual data. It is a relative comparison of two models and can therefore only be used as a relative measure and cannot place absolute constraints on the associated model parameter values.

As $\Delta\chi^2$ in Equation (4.24) is calculated with respect to the fiducial model, $\Delta\chi^2(\mathbf{p}_{\mathrm{fid}}) = 0$. The comparison model can then be ruled out at e.g. a 1, 2 or $3\sigma$ level of significance in those regions of the comparison model parameter space for which $\Delta\chi^2$ yields a value greater than the corresponding threshold value for the associated number of parameters, listed in Table 2.1. The key point of this method is the necessity of fixing $\sigma_\mu$, as we are using a $\chi^2$ statistic, otherwise we would fall into the trap we are warning against in Chapter 3.

Although current correlations in GRB spectral parameters are not currently calibrated with low-redshift data, Bertolami and Silva [56] have constructed mock low-$z$ data sets and used them to assess several existing correlations in order to obtain a plausible value for $\sigma_\mu$. For a sample of 40 GRBs, Bertolami and Silva report an error in the observed distance modulus $\sigma_\mu = 0.68$, with a decrease to $\sigma_\mu = 0.66$ for an observable sample of 100 mock GRBs.

### 4.4.3   How Useful Could GRBs Be?

In this section we illustrate one potential future application of GRBs. Selecting the Concordance Model $(\Omega_m, \Omega_\Lambda)$=(0.3,0.7) as our fiducial model, we have calculated the number of GRBs detected within certain redshift ranges necessary to rule out Conformal Gravity [20] at significance levels of 1, 2 and $3\sigma$. It should be noted that Conformal Gravity is a 1-parameter model and subsequently $\Delta\chi^2 = 1, 4, 9$ for 1, 2 and $3\sigma$ significance levels, respectively. The potential for this method can be seen in Fig 4.7. While 161 GRBs with $z_{max} = 1$ are required to rule out Conformal Gravity at a significance level of $3\sigma$, this drops rapidly as $z_{max}$ increases. For $z_{max} = 2$, 23 GRBs are required and for a mock data set drawn from Bertolami and Silva's GRB distribution outlined in §4.4.1 with $z_{max} = 5$, only 5 mock GRBs are needed to rule out Conformal Gravity at a $3\sigma$ significance level. This simple fiducial method highlights the impact that reliable high-redshift GRB data will have on cosmological model selection and parameter estimation.
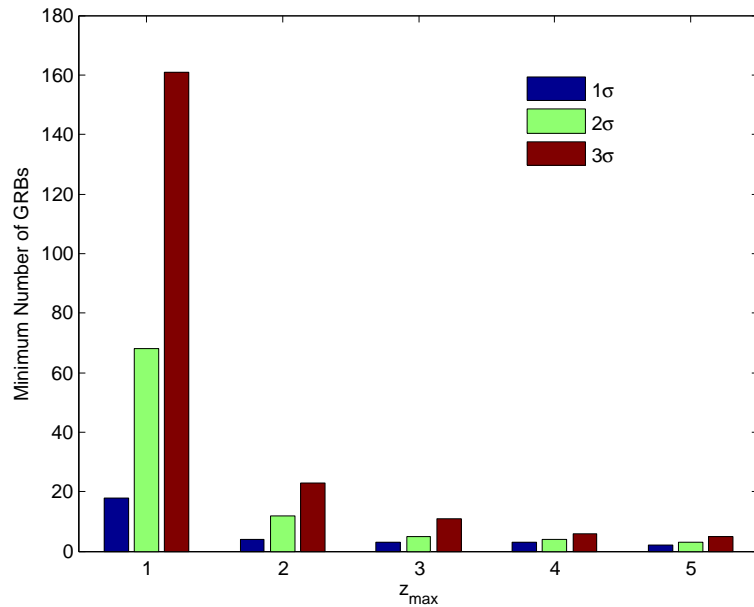


Figure 4.7: A histogram of the number of observable mock GRBs drawn from the representative redshift distribution of §4.4.1 with $z \leq z_{max}$ that are required to rule out Conformal Gravity at a significance level of 1, 2 and $3\sigma$.

### 4.4.4 Conclusions

The ability to generate mock data sets with a realistic redshift distribution and compare cosmological models without requiring low-redshift calibrators will facilitate further investigation of the potential use of GRBs as distance indicators in the hope that future data are more numerous and accurate. This potential improvement in both the progenitor models and necessary assumptions regarding the circumburst density and associated errors will undoubtedly refine the cosmological application of GRBs. Heeding our own caveat regarding the shortfalls of current GRB data outlined in Chapter 3, the analysis in §4.4 has been carried out for a fixed, cosmology-independent value of $\sigma_\mu$. It can be seen from Figure 4.7 that even small numbers of more accurate, high redshift GRBs would provide a significant contribution to cosmological model comparison.

In the following chapter we investigate the potential of another proposed high redshift distance indicator in the form of gravitational wave standard sirens. Through Bayesian model selection of competing cosmological models, we illustrate the significantly stronger diagnostic power of these highly accurate sources compared with current SN data.

# Chapter 5

# Cosmological Model Comparisons Using Standard Sirens

The detection of gravitational waves will be the last major vindication of Einstein's Theory of General Relativity. While the discovery itself will be momentous, it is just the first step towards opening a new window of observation in astronomy. As discussed in §2.2, gravitational wave standard sirens may provide the most accurate information on the evolution of the Universe to date. In this chapter we utilise predicted standard siren data to investigate their ability to differentiate between competing cosmological models through Bayesian model selection. The potential astronomy achievable with these remarkable sources is evident through direct comparison of their diagnostic power with that of Type 1a Supernovae, the Cosmic Microwave Background and Baryon Acoustic Oscillations.

## 5.1   Bayesian Model Selection

Bayesian parameter estimation is concerned with assigning the most probable values based on the peak in the posterior likelihood function across the whole parameter space. However, it is also important to account for the number of free parameters considered in the model, even though including more parameters may force a better fit to the data. Bayesian model selection provides a succinct method for choosing between two possible models by explicitly accounting for both the associated likelihood functions and the number of parameters involved.

### 5.1.1  Odds Ratio

In a Bayesian context, the comparison of two competing models $M_1$ and $M_2$ is achieved by evaluating the ratio of posterior probabilities, commonly referred to as the odds ratio

$$\frac{p(M_1|D,I)}{p(M_2|D,I)}, \tag{5.1}$$

where the data $D$ and other prior information $I$ are assumed to be the same for both models. Following Bayes' Theorem, given by Equation (2.24), each posterior probability can be expressed as

$$p(M_i|D,I) = \frac{p(D|M_i,I)p(M_i|I)}{p(D|I)}. \tag{5.2}$$

If we have no reason to favour one model over the other *a priori*, we assign equal priors to both models and hence $p(M_1|I) = p(M_2|I)$. The evidence $p(D|I)$ is also model independent as both posterior probabilities must be evaluated using the same data, hence the odds ratio is now simplified to

$$\frac{p(M_1|D,I)}{p(M_2|D,I)} = \frac{p(D|M_1,I)}{p(D|M_2,I)}, \tag{5.3}$$

which is simply the ratio of likelihoods for the two models. The likelihood of model $M_i$ is explicitly related to the set of model parameters $\theta_i$ and is calculated by marginalising the joint probability $p(D,\theta_i|M_i,I)$ over $\theta_i$, i.e.

$$p(D|M_i,I) = \int p(D,\theta_i|M_i,I)\mathrm{d}\theta_i. \tag{5.4}$$

In order to simplify this expression, we invoke the Product Rule, which states [57]

$$p(X,Y|I) = p(X|Y,I) \times p(Y|I), \tag{5.5}$$

where $p(X,Y|I)$ is the joint probability that both proposal $X$ and $Y$ are true, $p(X|Y,I)$ is the probability that proposal $X$ is true given that $Y$ is true and $p(Y|I)$ is the probability that proposal $Y$ is true, all for given information $I$.

This then allows us to express Equation (5.4) as

$$p(D|M_i,I) = \int p(D|\theta_i,M_i,I)p(\theta_i|M_i,I)\mathrm{d}\theta_i, \tag{5.6}$$

where the first term of the integrand is the likelihood, dependent on the parameter values for model $M_i$, and the second term is the prior for those parameters.

Therefore, the odds ratio of posterior probabilities in Equation (5.1) has been simplified to the ratio of likelihoods marginalised over the respective parameter set for each model. A data set can then be said to favour model 1 if the odds ratio is greater than the ratio of the parameter priors and to favour model 2 if the odds ratio is less than this threshold.

## 5.1.2 Priors

Bayesian Inference relies heavily on the selection of suitable priors. If computational cost was not an issue, a uniform prior could be assumed for all likelihood calculations, thus avoiding much debate over what could be argued as a subjective choice. However, it is not always appropriate, nor instructive, to integrate over the entire parameter space and thus a well chosen prior should be imposed. The parameter priors are utilised to reduce the range of values over which the likelihood must be computed and it is intuitive to use previous estimates of parameter values and other relevant background physical information in order to impose a likely range. For example, in assigning a prior on $\Omega_m$ it might be appropriate to consult previous constraints and define a range around the commonly accepted value, while also considering the physical constraint that $\Omega_m \geq 0$.

In practical terms, Equation (5.6) will be dominated by the likelihood if the model is supported by the evidence for any sensible choice of prior. If the evidence points against the model, the prior will dominate and this will be evident from the final value of the odds ratio. This is illustrated in Figure 5.1 [48].

A simple prior that assigns a uniform probability to a parameter $\lambda$ within a given range $\lambda_{min} \leq \lambda \leq \lambda_{max}$ is given by [57]

$$p(\lambda|M_i, I) = \frac{1}{\lambda_{max} - \lambda_{min}}. \tag{5.7}$$

If this uniform prior is commonly applied to all parameters within the set $\theta$, the joint prior for an $n$ parameter model is simply

$$p(\theta|M, I) = \prod_{i=1}^{n} \frac{1}{\lambda_{max}^i - \lambda_{min}^i}. \tag{5.8}$$

As the assigned priors are now independent of the model parameters, the odds

ratio can be written as

$$\frac{p(D|M_1, I)}{p(D|M_2, I)} = \frac{p(\theta_1|M_1, I)}{p(\theta_2|M_2, I)} \times \frac{\int p(D|\theta_1, M_1, I)\mathrm{d}\theta_1}{\int p(D|\theta_2, M_2, I)\mathrm{d}\theta_2}, \tag{5.9}$$

with the integration performed over the chosen parameter range.

The ratio of priors in Equation (5.9) encapsulates the concept of Occam's Razor, which states *"it is vain to do with more what can be done with fewer"*. This Occam factor will act to penalise a model with a greater number of parameters, ensuring that the model is only favoured if the likelihood is strongly supported and thus disregards the influence of the prior. Equation (5.9) now provides the necessary tools with which to compare any models of interest.
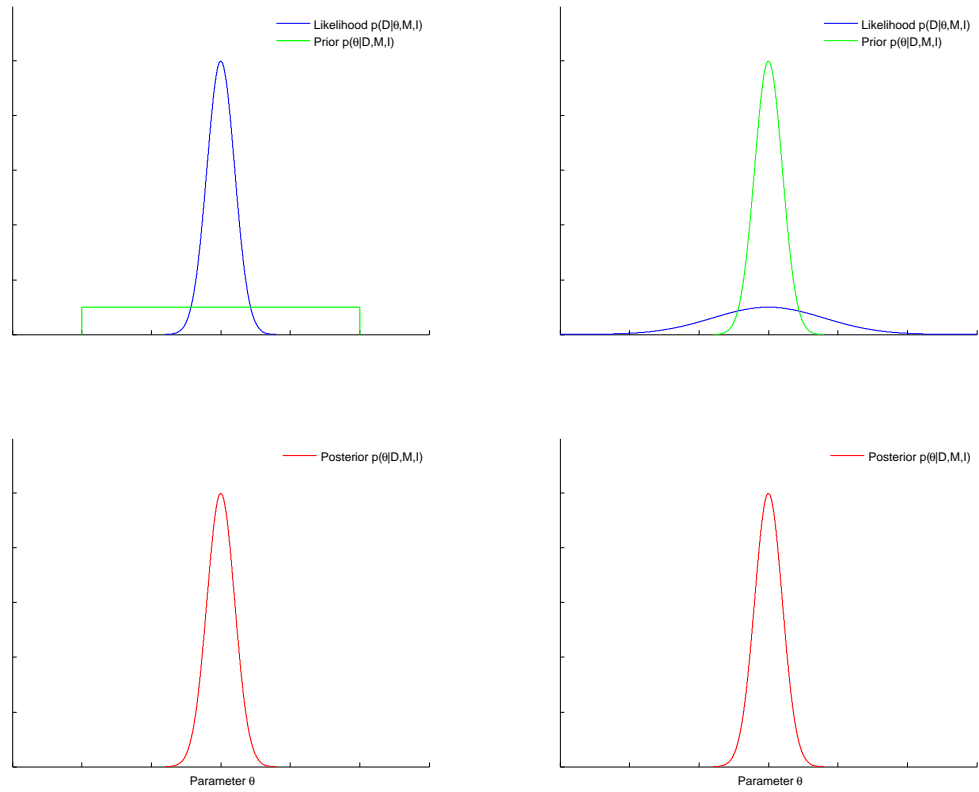


Figure 5.1: The posterior pdf for a parameter $\theta$ will be dominated by the likelihood if the data proves a good fit to the model, regardless of the prior (left). However, the prior will dominate the posterior pdf if the likelihood suggests a poor fit of the data to the model (right) [48].

## 5.2   Standard Sirens and Unified Dark Matter

As outlined in §1.3.2, the Unified Dark Matter (UDM) model of Balbi et al. [21] proposes that the two dark components arising in $\Lambda$CDM are two faces of a single component, parameterised by $\Omega_\Lambda$ and $\alpha$. The motivation for applying standard sirens to investigate the UDM model is two-fold: firstly, it is instructive to see whether standard sirens can further constrain the current limits on $\Omega_\Lambda$ and $\alpha$; secondly, it allows a direct model comparison between a model with a fixed value of $\alpha$ and a model in which the value of $\alpha$ may have been different in an earlier epoch, in order to highlight the diagnostic power of standard sirens.

### 5.2.1   UDM with Constant $\alpha$

Constraints on $\Omega_\Lambda$ and $\alpha$ have been published by Balbi et al. using 182 Type 1a Supernovae [11], baryon acoustic oscillations, and the CMBR [21] and these results are reproduced in Figure 5.2. They took the value of the measured BAO parameter $A$ as published in the SDSS luminous red galaxy survey [12] as $A = 0.496 \pm 0.017$ and they calculated the CMBR shift parameter $R$ by MCMC analysis of WMAP data [15] as $R = 1.71 \pm 0.03$.



Figure 5.2: UDM likelihood contours reproduced from Balbi et al. (2007), showing 68%, 95% and 99% confidence levels in the $\alpha$-$\Omega_\Lambda$ plane for SN, BAO and CMBR data (left) and the combined contours (right).

Balbi et al. concluded that the combined data supported a non-zero $\alpha = 0.01$, indicating a small but significant deviation from a flat $\Lambda$CDM model, for which

$\alpha = 0$. However, we can see from Figure 5.2 that although $\alpha = 0.01$ is identified as the best fit value, $\alpha = 0$ cannot be ruled out at even the $1\sigma$ level. We have therefore applied standard sirens to the UDM model to ascertain at what level, if any, they could rule out $\alpha = 0$. It should be noted that there is not currently an accepted predicted redshift distribution for gravitational wave sources. However, as discussed in §2.2, typical errors on well-localised super-massive binary black hole (SMBBH) inspirals have projected errors $< 1\%$, even at redshifts in the range $z = 1$ to 3 [33].
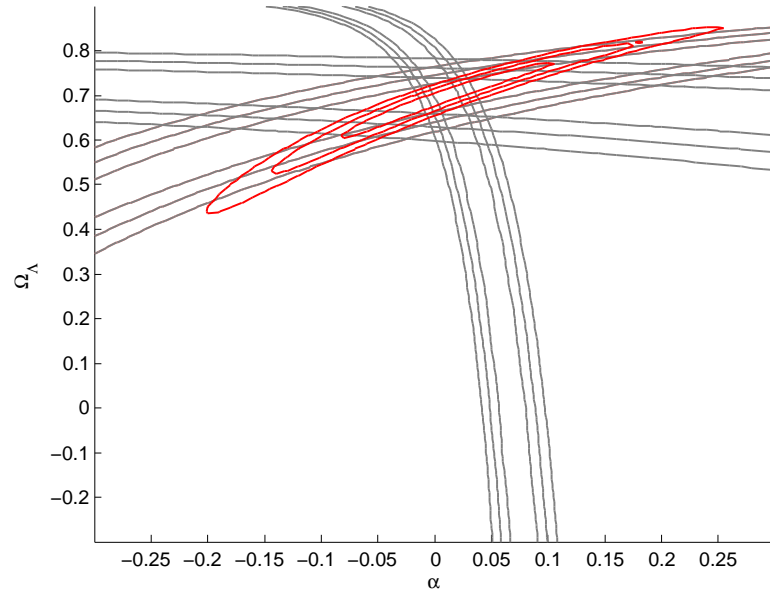


Figure 5.3: UDM likelihood contours for 2 standard sirens at $z = 0.5, 4$ are shown in red. The grey contours for SN, BAO and CMBR data are reproduced following Balbi et al. (2007) and can also be seen in Figure 5.2.

Figure 5.3 shows the constraints placed on $\Omega_\Lambda$ and $\alpha$ by adding only 2 standard siren sources at $z = 0.5, 4$, with no measurement error assumed, to the original analysis by Balbi et al. The combined contours for these standard siren sources can be seen in Figure 5.4, along with combined contours for 10 sources uniformly distributed in the redshift range $0.1 \leq z < 2$. While the standard siren contours in Figure 5.3 are significantly tighter than those of the Supernovae, and offer greater constraint on $\Omega_\Lambda$, standard sirens still provide only a small improvement on constraining $\alpha$. This is seen further in the combined contours of Figure 5.4,

where increasing the number of mock standard sirens from 2 to 10 adds only a little extra constraint across the $\alpha$ parameter space, where $\alpha = 0$ is ruled out at a significance level of only $1\sigma$.
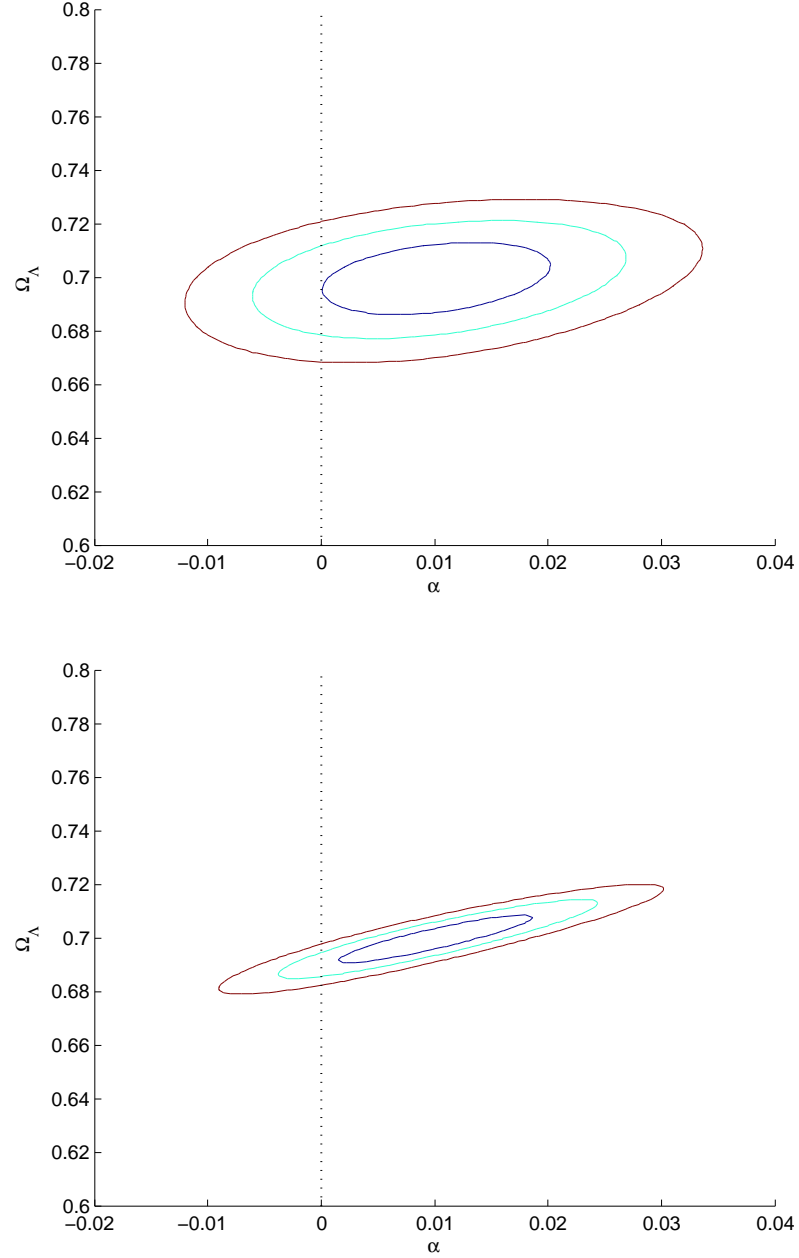


Figure 5.4: UDM likelihood contours for combined SN, BAO and CMBR, reproduced from Balbi et al. (2007), with the addition of 2 standard sirens z=0.5,4 (top) and 10 sirens distributed uniformly with $z \in [0.1, 2]$ (bottom).

### 5.2.2 Model Comparison for Non-constant $\alpha$

UDM is an attractive alternative to the concordance model as the 2 parameter equation of state is locally defined and therefore independent of redshift $z$. This is in contrast to the popular 2 parameter equation of state for evolving dark energy in the concordance model that introduces an evolutionary $z$ dependence, in the form of a first order approximation of a Taylor expansion

$$w = w_0 + w_1 z. \tag{5.10}$$

However, this advantage over other models would be negated if $\alpha$ was to be shown to be redshift dependent after all. Current SN observations may not be accurate enough to provide conclusive evidence of a non-constant equation of state; however, it may be the case that standard sirens could provide a stringent enough test. To this end, we construct a simple Bayesian model comparison, following the method outlined in §5.1, with which to test this hypothesis. We define models 1 and 2 as follows:

$$\text{MODEL 1}: \quad \alpha = \alpha_1 \neq 0 \qquad \text{for} \qquad 0 \leq z \leq 10$$
$$\text{MODEL 2}: \begin{cases} \alpha = \alpha_1 \neq 0 & \text{for} \quad 0 \leq z \leq z_{crit} \\ \alpha = \alpha_2 \neq 0 & \text{for} \quad z_{crit} \leq z \leq 10, \end{cases}$$

where $z_{crit}$ is some arbitrary critical redshift limit. While this arbitrary limit may seem unjustified, it is analogous to the frequently invoked kick-in of Dark Energy in the concordance model above redshift $z \sim 1$, as discussed in §1.2.1.

We test this hypothesis by generating fake data for both Type 1a SN and only 2 standard sirens. The 182 fake SN are drawn from the same redshift distribution as the 'Gold' data used in previous analysis [11], while the sirens are uniformly distributed around $z_{crit}$, with fractional observed luminosity distance errors of 1%, as discussed in §2.2. Both the SN and standard sirens are generated based on Model 2 – i.e. we fix $\alpha_1 = 0.01$ for the low redshift value of $\alpha$, as suggested by the best fit result in Balbi et al., and pick a value for $\alpha_2 \in [0.02, 0.3]$, with a fixed value for $\Omega_\Lambda = 0.7$. As the data are drawn from a universe that adheres to Model 2, we would expect a reliable indicator to favour that model in the odds ratio for all values of $\alpha_2$ and a $z_{crit}$ that lies within the redshift range of the data

set. An unreliable indicator may favour the incorrect model or may not strongly favour either model, particularly for $\alpha_2 \simeq \alpha_1$.
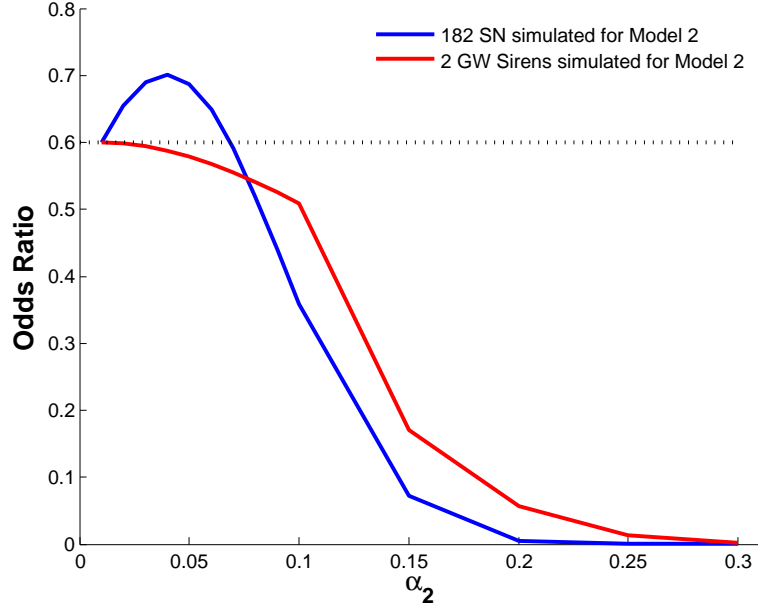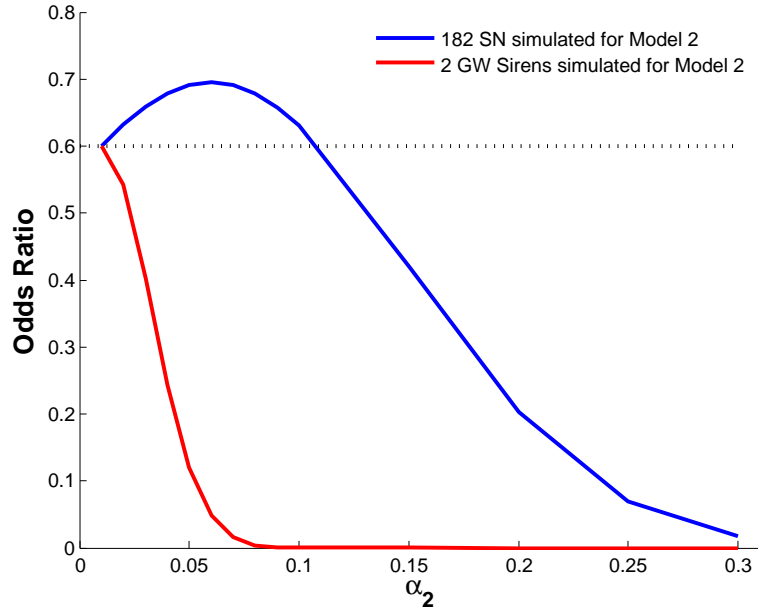


(a) $z_{crit} = 0.25$



(b) $z_{crit} = 1$

Figure 5.5: Odds ratios for $z_{crit} = 0.25$ and $z_{crit} = 1$. These are calculated for discrete values of $\alpha_2 = 0.01, 0.02, \ldots, 0.1, 0.15, \ldots, 0.3$. 182 'Gold' SN (blue) have been compared with 2 standard sirens (red). A result above the threshold value of 0.6 supports Model 1, while an odds ratio below indicates Model 2 is more likely.

The odds ratio, given by Equation (5.9) is calculated by marginalising over $\alpha_{1,2} \in [-0.3, 0.3]$, as in the analysis for a constant $\alpha$. This range then provides the parameter priors for Equation (5.8), giving $\frac{10}{6}$ and $\frac{25}{9}$ for Models 1 and 2 respectively. The ratio of priors appearing in Equation (5.9) is then 0.6; an odds ratio greater than this threshold would suggest that the data supports Model 1, while Model 2 is favoured for any value below this cut off. Figure 5.5 shows the calculated odds ratios for varying values of $z_{crit}$ and $\alpha_2$.

It is evident from Figure 5.5 that while the standard sirens are accurate enough to select the correct model, even for $\alpha_2 \simeq \alpha_1$, the 182 SN only favour the correct model in the more extreme cases. Type 1a Supernovae are therefore not currently accurate enough to place constraints on a redshift dependent $\alpha$. These results also highlight and illustrate the significantly improved accuracy and diagnostic power that standard sirens will bring to cosmological model selection.

### 5.2.3 Conclusions

We have presented 2 examples of the potential contribution of standard sirens in cosmological model selection, based upon an alternative to $\Lambda$CDM in the form of Unified Dark Matter. The results in §5.2.1 and §5.2.2 illustrate the significant improvement that standard sirens will make over current indicators such as Type 1a SN. It should be noted that these are perhaps best case scenarios – see the discussion in §2.1.2 regarding gravitational lensing and detection rates – however, the issues surrounding corrections for background gravitational lensing are currently being tackled (for example [59]). It is therefore hopeful that by the time there exist reliable detections of gravitational wave sources, many of the issues associated with potential systematic errors will have been resolved.

While UDM is an interesting alternative to $\Lambda$CDM, any model could have been used as a test case to explore the diagnostic ability of standard sirens. Having established that they are indeed significantly more sensitive than current distance indicators for the specific case of the UDM model, we go on to apply them to a currently heated debate regarding Dark Energy and intrinsic curvature.

## 5.3   Dark Energy vs. Curvature

Simplifications and assumptions are often a necessary part of data analysis, particularly when degeneracies in a model would otherwise render progress very difficult. However, there is a growing realisation that invoking Occam's Razor as a justification for these simplifications may result in important information being lost and and conclusions being inherently wrong. Much of the literature surrounding the nature of dark energy and attempts to constrain the equation of state of dark energy $w(z)$ is split: the equation of state is constant with $w = -1$ and this allows probing of the intrinsic curvature; the flip side probes dynamical dark energy but generally includes the assumption that $\Omega_k = 0$. However, there is a growing concern (for example [60] and references therein) that intrinsic curvature may masquerade as dynamical dark energy if $\Omega_k$ is not also allowed to vary as a free parameter. Some current attempts at resolving this issue have focussed on quantifying the errors in measured parameters that would result from making these assumptions [60], [61]. The approach in this work instead focuses on determining the quality of data that will be required to render such simplifying assumptions unnecessary. In other words, by constructing the problem as one of Bayesian model selection, we can quantify the diagnostic power of standard sirens compared with existing distance indicators, such as SN, BAO and the CMBR, in a similar vein to §5.2.

### 5.3.1   Curvature and Evolving Dark Energy Model Comparison

The equation of state of dark energy has several common parameterisations to include evolution over time. All are somewhat arbitrary and all have their merits and disadvantages. For the purposes of the model comparison example presented here we use the parameterisation given in Equation (5.10)

$$w = w_0 + w_1 z.$$

The general expression for the Hubble parameter defined in Equation (1.14) is then

$$E(z) = \left[\Omega_m(1 + z)^3 + \Omega_\Lambda \left((1 + z)^{3(1+w_0+w_1)}e^{(-3w_1 z)}\right) + \Omega_k(1 + z)^2\right]^{1/2}, \quad (5.11)$$

which simplifies to the standard expression for $\Lambda$CDM, given in Equation (1.15), for constant $w$. Again, two models are defined:

$$\text{MODEL 1}: \; \Omega_k \neq 0, \, w = -1$$
$$\text{MODEL 2}: \; \Omega_k = 0, \, w(z) = w_0 + w_1 z.$$

Mock SN, BAO, CMBR and siren data are then generated for a universe adhering to Model 1, again ensuring the expected answer is known. We choose to marginalise Model 1 over the range $\Omega_k \in [-0.1, 0.1]$, while Model 2 is marginalised over $w_1 \in [-1.5, 1.5]$, in line with commonly used parameter spaces [60], [61]. Priors are calculated as outlined in §5.1.2, which yields the ratio of priors, and hence the threshold for the odds ratio favouring Model 1 or 2, as 15. In order to quantify how much of an improvement sirens could make to the contribution of SN, BAO and the CMBR, we calculate the odds ratio of Model 1 vs. Model 2 for SN + BAO + CMBR and then compare that with the added siren data.

As discussed in §2.2, it is hoped that standard sirens will be accurate to $\sim 1\%$ in luminosity distance $d_L$. However, this may not be achievable with initial detections. It is therefore instructive to compare a range of predicted errors in order to ascertain any reduction in efficacy, should the ideal scenario elude us. It also enables a fairer comparison with current observations of SN, CMBR and BAO data as these indicators will undoubtedly improve in accuracy within the timescale of standard siren detection. As such, we consider errors in $d_L$ for the sirens of 1%, 2% and 5% when comparing with the SN, BAO and CMBR data.

Figure 5.6 shows the odds ratios for these data sets for a universe with a range of intrinsic curvatures. It is evident that without the siren data, intrinsic curvature and dynamical dark energy can be easily confused. SN, BAO and CMBR data cannot correctly identify an intrinsic curvature in the range $-0.015 < \Omega_k < 0.05$, with the odds ratio instead favouring dynamical dark energy. However, the addition of even a small number of standard sirens with an optimum error of 1% can contribute a great deal to the problem. Adding 2 sirens at $z = 0.25, 3$ narrows the region of uncertainty slightly, while including 10 sirens drawn uniformly from $z \sim \mathrm{U}\,[0, 4]$ only selects the incorrect model for $-0.01 < \Omega_k < 0.025$.
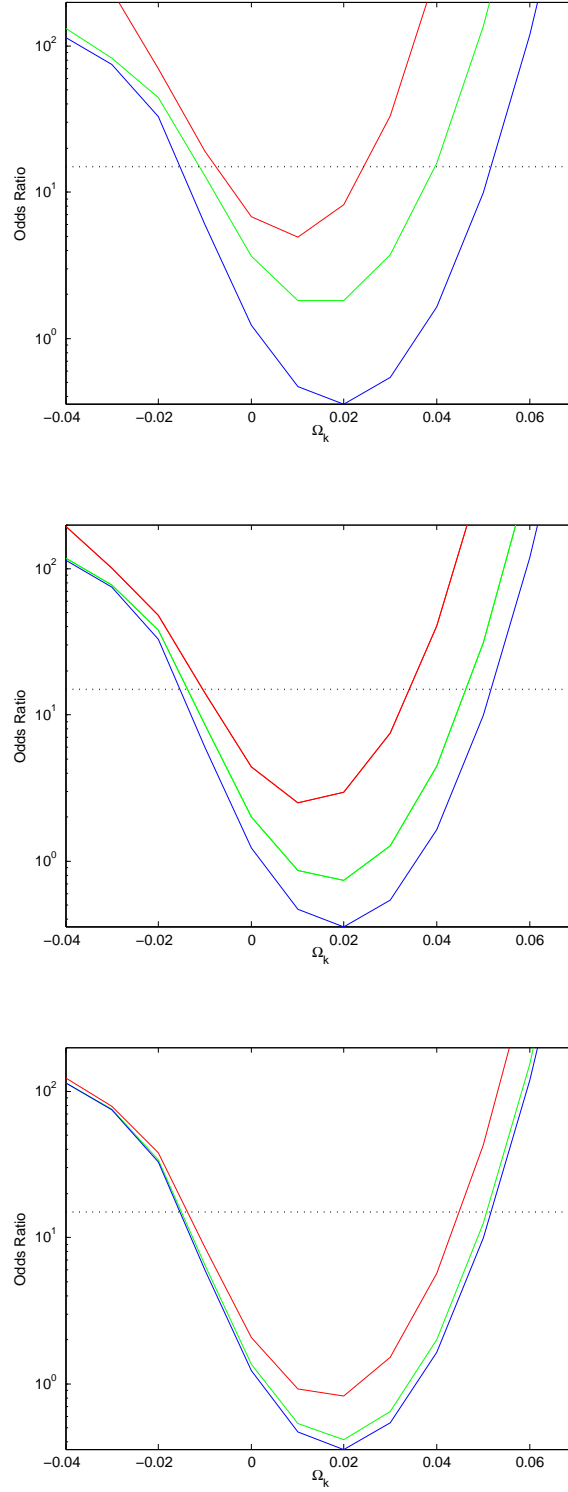
Figure 5.6: Odds ratios for SN + BAO + CMBR (blue) compared with SN + BAO + CMBR + 2 sirens at $z = 0.25, 3$ (green) and SN + BAO + CMBR + 10 sirens at $z \sim \mathrm{U}\,[0, 4]$ (red). Estimated errors in the measured luminosity distance for the standard sirens are $\sigma_{d_L} = 1\%$ (top), $\sigma_{d_L} = 2\%$ (middle) and $\sigma_{d_L} = 5\%$ (bottom). The dotted line is the ratio of priors $P_1/P_2 = 15$, above which Model 1 is correctly identified and below which the indicators confuse dynamical dark energy with curvature.

Figure 5.6 also shows that should the luminosity distances for sirens not be as well constrained as $\sigma_{d_L} = 1\%$, their contribution to this problem is greatly reduced. For $\sigma_{d_L} = 2\%$, 2 sirens afford little improvement to current distance indicators, while 10 sirens narrow the range of uncertainty to $-0.01 < \Omega_k < 0.035$. However, should the error estimates only be constrained to $\sigma_{d_L} = 5\%$, even 10 sirens add little more diagnostic power to the current data, as can be seen by the proximity of the odds ratios in the bottom plot of Figure 5.6. While a larger number of standard sirens would undoubtedly improve this situation, initial data sets will consist of only a small number of sirens with reliable redshift estimates, due to the aforementioned difficulty of identifying an optical counterpart. These results therefore reinforce the necessity of addressing the issue of weak lensing prior to the first gravitational wave detections.

## 5.3.2 Conclusions

Differentiating between dynamical dark energy and intrinsic curvature is a very subtle problem. At more extreme levels of curvature, sirens are not required as is evident from the large odds ratio in favour of Model 1. As Model 1 approaches Model 2 however, the currently established indicators cannot reliably identify the correct model and even 2 sirens with a best-case accuracy of $\sigma_{d_L} = 1\%$ add extra diagnostic power at this level. However, at very small levels of intrinsic curvature $\Omega_k \sim 0 - 0.02$, or larger measured distance errors in the siren data, even 10 very accurate sirens cannot lend enough support to distinguish clearly between Model 1 and 2. As discussed previously in §1.2.2, the currently reported values of $\Omega_k$ lie within this range of confusion. On the one hand this would suggest that sirens will not contribute greatly to attempts to solve this problem. However, these results serve to highlight the difficulty in accurately determining the true value of $\Omega_k$ and how easily dynamical dark energy models could be confused with models that include intrinsic curvature. Small intrinsic curvature, as a model, is of comparable acceptability to an evolving dark energy, but accurate siren data could significantly narrow the range within which this confusion exists. Outside that range, the correct model is identified.

## 5.4   Conformal Gravity Revisited

Many of the conclusions proffered in this thesis have concerned the current limitations of GRB data and the potentially unprecedented contribution that standard sirens could make. To finish in this vein and come full circle, we return to Conformal Gravity and the potential link between short GRBs and gravitational wave sources.

### 5.4.1   Mock Siren Data

In previous sections of this chapter, random redshifts have been allocated to sirens for illustrative purposes as an established redshift distribution akin to that presented in §4.4.1 for GRBs has not yet been derived. However, as discussed in §2.3.1, the progenitor for short, hard GRBs is thought to be a compact object binary merger. These events are a primary target for ground-based gravitational wave detection. Of the 21 well-localised short, hard bursts (SHB) detected by SWIFT to date [62], 13 have reliable optical counterpart redshifts. These potential standard siren progenitors populate the range $0.089 \leq z \leq 1.131$ and are listed in Table 5.1.

| GRB | $z$ |
|--------|-------|
| 050509 | 0.225 |
| 050709 | 0.161 |
| 050724 | 0.258 |
| 051221 | 0.546 |
| 060502 | 0.287 |
| 060505 | 0.089 |
| 060614 | 0.125 |
| 060801 | 1.131 |
| 061006 | 0.438 |
| 061201 | 0.111 |
| 061210 | 0.410 |
| 061217 | 0.827 |
| 070724 | 0.457 |

Table 5.1: Redshift data for 13 short, hard GRBs used as potential standard siren events, with a fractional error on the fiducial luminosity distance of 1% [62].

We therefore apply these mock sirens, again with fractional luminosity distance errors of 1%, 2% and 5%, to a similar fiducial analysis as described in §4.4.2. By calculating $\Delta\chi^2$ from Equation (4.24), with respect to a selected fidu-

cial model, we can establish the number of mock standard sirens that return a value of $\Delta\chi^2 > 1, 4, 9$, thus ruling out Conformal Gravity at a significance level of 1, 2 and $3\sigma$, respectively.
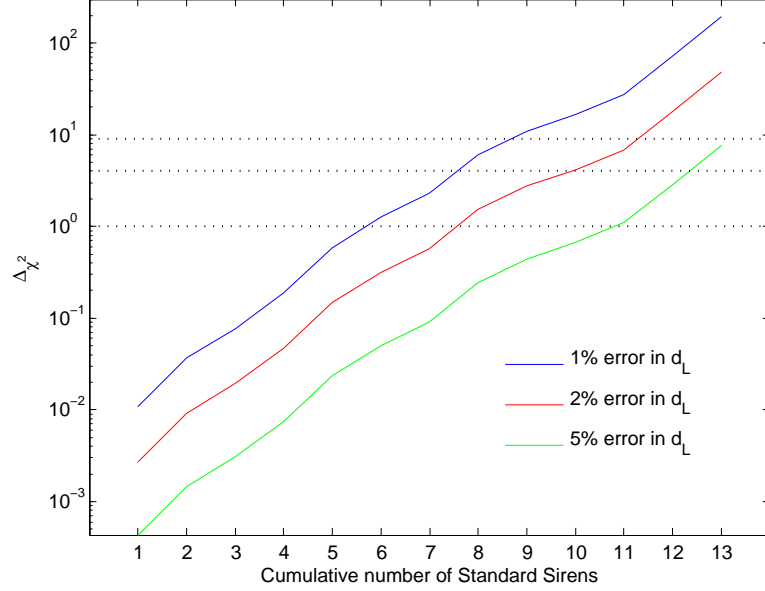


Figure 5.7: The cumulative $\Delta\chi^2$ value for Conformal Gravity (CG) fitted to 13 potential standard sirens with redshift $0.089 \leq z \leq 1.131$. Estimated errors in the measured luminosity distance of the sirens are included as 1% (blue), 2% (red) and 5% (green). A value of $\Delta\chi^2$ above the dotted lines at $\Delta\chi^2 = 1, 4, 9$ would signify that the standard siren data rules out CG at a significance level of 1, 2 and $3\sigma$, respectively.

Figure 5.7 shows the cumulative $\Delta\chi^2$ values for the data set from low to high redshift. Again, for $\sigma_{d_L} = 1\%$, sirens are shown to be effective, accurate distance indicators; the nearest 9 sirens, with a range of only $0.089 \leq z \leq 0.483$ are already sufficient to rule out Conformal Gravity at $3\sigma$. Indeed, the highest redshift siren at $z = 1.131$ returns $\Delta\chi^2 = 119.8$ alone. It is evident that only a handful of local sirens could be sufficient to differentiate between and potentially rule out many of the proposed alternatives to the Concordance Model. The increased errors again serve to reduce the diagnostic power of the standard siren data, with 13 sirens unable to rule out Conformal Gravity at a significance level of $3\sigma$. However, the lower redshift sirens in this data set will be less affected by weak lensing, resulting in Figure 5.7 being an over-cautious estimate of the effect of larger luminosity distance errors.

### 5.4.2 Conclusions

The selection of a suitable redshift distribution for standard siren sources will continue to be contentious until the first confirmed detections and the associated redshifts are obtained from a reliable electromagnetic counterpart. However, this work makes no attempt to investigate the physics of standard siren progenitors and is concerned only with what may be achieved from potential future data. The redshifts selected have therefore been merely illustrative of the potential diagnostic power of sirens. Allowing for that, we have shown that gravitational wave standard sirens could contribute an unprecedented level of accuracy to cosmological parameter estimation. We have done this by extending recent examples of non-standard cosmological models, such as the Unified Dark Matter model [21], Conformal Gravity [19] and the increasingly high profile issue of intrinsic curvature and evolving dark energy, to which sirens will bring important insight and diagnostic power. Many of the sirens used in the Conformal Gravity analysis are also at sufficiently low redshift that issues of systematic biases resulting from weak gravitational lensing will also be negligible. These encouraging projections should emphasise the important role that gravitational wave detection and analysis will play in future astronomical advances.

# Chapter 6

# Discussion and Future Work

## 6.1   Gamma Ray Bursts

The initial flurry of excitement surrounding the early proposals of potential correlations in GRB spectral parameters has subsided during the time span of this thesis. This may be in part due to the realisation that utilising GRB data is not as straightforward as, for example, Type 1a Supernova data. There have also been questions widely raised regarding the reliability of proposed spectral correlations and accuracy of the data, as previously discussed in this work with reference to Friedman and Bloom's extensive appraisal [47]. However, any new results published still implement incorrect procedure and sometimes questionable data selection. As such, the relevance of the work presented in this thesis is continually justified.

The focus of the work presented here relating to GRBs has been concerned with the methodological flaws in current GRB data analysis, and in particular the misapplication of Bayesian statistical methods when implementing the much-reported Ghirlanda Relation. We have demonstrated that current data are not accurate or numerous enough to differentiate convincingly between competing cosmological models. We have also shown that currently published results utilising the standard goodness-of-fit $\chi^2$ statistic to construct confidence regions do not accurately represent the full Bayesian posterior likelihood. This is because these methods neglect the dependence on the cosmological parameters of both the 'observed' GRB luminosity distances and their errors, due to the cosmology dependence of the best-fit Ghirlanda Relation. This subtlety renders invalid

a widely-used simplification: the integrated likelihood function is no longer a simple, monotonic function of the $\chi^2$ statistic. Subsequently, both the best-fit parameter values and confidence intervals are systematically misidentified. Inappropriate, pseudo-Bayesian methods have then been proposed that not only build on this incorrect foundation, but are in themselves statistically incorrect. It is essential to be rigorous in the use of Bayesian inference terms and procedures, and we have shown that algorithms that may appear to be robustly Bayesian in their construction are in fact simply wrong and cannot be utilised at all.

Having issued several caveats and reprimands towards would-be Bayesian analysts, we have also considered the potential of GRBs as high redshift distance indicators, assuming that the calibration and methodological issues we have identified could be overcome. Our projections show that the addition of GRBs to the cosmological Hubble diagram will add a powerful diagnostic in the bid to place stronger constraints on cosmological models and their associated parameters. However, this will only be possible if the quality of data improves and either nearby calibrators are found to remove the doubt surrounding spectral correlations or the underlying physics of GRB progenitors is better understood. On a positive note however, GRB-cosmology is a very new area of research. The continuing acquisition of data via the dedicated SWIFT mission and increasing profile of the field can only be of benefit to the cause.

Gamma ray bursts will undoubtedly continue to play a major role in attempts to probe the high redshift universe. However, the accuracy of any data used and statistical techniques implemented is and will continue to be paramount.

## 6.2 Gravitational Wave Standard Sirens

Should gravitational waves be detected, the potential benefits to astronomy are immeasurable. Within cosmology, standard sirens could prove to be the most accurate distance indicators to date. This stems from the well-understood and relatively simple physics behind the signal, a stark contrast to GRBs and to a lesser extent Type 1a Supernovae. We have presented several illustrations of what standard siren data could add to cosmological model selection in the context of

a widely applicable Bayesian framework. Although we have focused on specific models – the Concordance model, Conformal Gravity, Unified Dark Matter and the issue surrounding dark energy and intrinsic curvature – the analysis we have presented here is transferable to any model of choice. We have shown that, should gravitational wave sources be detected and the estimates on the accuracy of the data be vindicated, just a handful of standard sirens can out-perform all the currently utilised distance indicators. Obviously though, it is not a choice between the old and the new: standard sirens will complement and add to the current SN, GRB, BAO and CMBR data, furthering confidence in any constraints drawn from the ever-increasing amount of data available.

As with all future projections, there is a tendency to err on the optimistic side. The reported errors in siren data may not be as small as we have assumed. This will be due mainly to the currently unanswered issue arising from stochastic gravitational lensing. This effect may act to smear out the signal and greatly increase the uncertainty in the data. However, with such great interest surrounding the search for gravitational waves and future projections highlighting how useful the data could be, an increasing focus is being placed on solving this problem.

While accurate GRB data may provide a shorter term improvement in cosmological analysis, the addition of gravitational wave standard sirens will undoubtedly catapult cosmologists' understanding of the Universe onto an entirely new and unprecedented level.

## 6.3   Further Work

The physics underpinning the proposed spectral parameter correlations for GRBs is currently poorly understood and further attempts to improve these existing relations could be seen as futile. Focus should instead be placed upon understanding the progenitors of GRBs and potential selection effects in their detection that will lead to bias in any future cosmological studies that may utilise high redshift events.

While gravitational wave standard sirens may seem the more attractive high redshift distance indicator compared with gamma ray bursts, a great deal of work

is still required to understand and account for the systematic errors that will be introduced due to weak gravitational lensing. We have shown what could be achieved in a best case scenario and it is now vital to develop the tools to make these projections viable. It would be misguided to await the first detection of a gravitational wave source before attempting to solve the problems that stochastic lensing will introduce.

In addition to detecting the gravitational wave signature of a potential standard siren, of equal import is the need to reliably identify an EM counterpart in order to establish the source redshift. This need for a multimessenger approach in combining gravitational wave and electromagnetic observations necessitates the development and implementation of EM telescopes that will be capable of probing the Universe deeper than ever before.

# Bibliography

[1] D. Adams. *The Hitchhiker's Guide to the Galaxy*. ISBN 0 330 25864 8, 1979.

[2] K. Vonnegut. *Timequake*. ISBN 0 425 16434 9, 1997.

[3] E. L. Wright. Ned Wright's Cosmology Tutorial
`http://www.astro.ucla.edu/~wright/cosmo_01.htm`.

[4] 2dF Galaxy Redshift Survey. `http://magnum.anu.edu.au/~TDFgg/`.

[5] C. Mastropietro and A. Burkert. Simulating the Bullet Cluster. *Monthly Notices of the Royal Astronomical Society*, 389:967–988, September 2008.

[6] A. Banerjee and C. J. Jog. The Flattened Dark Matter Halo of M31 as Deduced from the Observed H I Scale Heights. *Astrophysical Journal*, 685:254–260, September 2008.

[7] The Virgo Consortium Millenium Simulation                     .
`http://www.virgo.dur.ac.uk/new/index.php?subject=millennium`.

[8] A. G. Riess et al. Observational Evidence from Supernovae for an Accelerating Universe and a Cosmological Constant. *Astron. J.*, 116:1009–1038, September 1998.

[9] R. Massey et al. Dark matter maps reveal cosmic scaffolding. *Nature*, 445:286–290, January 2007.

[10] A. G. Riess et al. Type Ia Supernova Discoveries at z>1 from the Hubble Space Telescope: Evidence for Past Deceleration and Constraints on Dark Energy Evolution. *Astrophys. J.*, 607:665–687, June 2004.

[11] A. G. Riess et al. New Hubble Space Telescope Discoveries of Type Ia Supernovae at z≥1: Narrowing Constraints on the Early Behavior of Dark Energy. *Astrophysical Journal*, 659:98–121, April 2007.

[12] D. J. Eisenstein et al. Detection of the Baryon Acoustic Peak in the Large-Scale Correlation Function of SDSS Luminous Red Galaxies. *Astrophysical Journal*, 633:560–574, November 2005.

[13] M. Tegmark et al. Cosmological constraints from the SDSS luminous red galaxies. *Physical Review D*, 74(12):123507–+, December 2006.

[14] S. Cole, S. Hatton, D. H. Weinberg, and C. S. Frenk. Mock 2dF and SDSS galaxy redshift surveys. *Monthly Notices of the Royal Astronomical Society*, 300:945–966, November 1998.

[15] Wilkinson Microwave Anisotropy Probe. `http://map.gsfc.nasa.gov/`.

[16] G. Hinshaw et al. Five-Year Wilkinson Microwave Anisotropy Probe (WMAP) Observations: Data Processing, Sky Maps, and Basic Results. *ArXiv e-prints*, March 2008.

[17] X. Yang et al. Populating dark matter haloes with galaxies: comparing the 2dFGRS with mock galaxy redshift surveys. *Monthly Notices of the Royal Astronomical Society*, 350:1153–1173, June 2004.

[18] I. L. Shapiro and J. Solà. Cosmological constant problems and the renormalization group. *Journal of Physics A Mathematical General*, 40:6583–6593, June 2007.

[19] P. D. Mannheim. Cosmic Acceleration as the Solution to the Cosmological Constant Problem. *Astrophysical Journal*, 561:1–12, November 2001.

[20] P. D. Mannheim. Options for cosmology at redshifts above one. In B. N. Kursunoglu, M. Camcigil, S. L. Mintz, and A. Perlmutter, editors, *AIP Conf. Proc. 672: Short Distance Behavior of Fundamental Interactions*, pages 47–64, June 2003.

[21] A. Balbi, M. Bruni, and C. Quercellini. $\Lambda\alpha$DM: Observational constraints on unified dark matter with constant speed of sound. *Physical Review D*, 76(10):103519–+, November 2007.

[22] M. Visser. Energy conditions in the epoch of galaxy formation. *Science*, 276:88–90, April 1997.

[23] P. Ruiz-Lapuente. Cosmology with Supernovae: The Road from Galactic Supernovae to the edge of the Universe. *Astrophysics and Space Science*, 290:43–59, February 2004.

[24] S. Perlmutter. Supernovae, Dark Energy, and the Accelerating Universe. *Physics Today*, April 2003.

[25] Y. Wang and P. Mukherjee. Observational constraints on dark energy and cosmic curvature. *Physical Review D*, 76(10):103533–+, November 2007.

[26] B. A. Bassett, B. Nichol, and D. J. Eisenstein. WFMOS: Sounding the dark cosmos. *Astronomy and Geophysics*, 46(5):050000–5, October 2005.

[27] C. L. Bennett. Cosmology from start to finish. *Nature*, 440:1126–1131, April 2006.

[28] B. F. Schutz. *A First Course in General Relativity*. ISBN 0521277035. Cambridge University Press, February 1985.

[29] Laser Interferometer Gravitational-Wave Observatory . `http://www.ligo.caltech.edu/`.

[30] Laser Interfometer Space Antenna. `http://lisa.nasa.gov/`.

[31] J. M. Weisberg, J. H. Taylor, and L. A. Fowler. Gravitational waves from an orbiting pulsar. *Scientific American*, 245:74–82, October 1981.

[32] M. Hendry and G. Woan. Gravitational astrophysics. *Astronomy and Geophysics*, 48(1):010000–1, February 2007.

[33] N. Dalal, D. E. Holz, S. A. Hughes, and B. Jain. Short GRB and binary black hole standard sirens as a probe of dark energy. *Physical Review D*, 74(6):063006–+, September 2006.

[34] D. E. Holz and E. V. Linder. Safety in Numbers: Gravitational Lensing Degradation of the Luminosity Distance-Redshift Relation. *Astrophysical Journal*, 631:678–688, October 2005.

[35] N. Dalal, D. E. Holz, X. Chen, and J. A. Frieman. Corrective Lenses for High-Redshift Supernovae. *Astrophysical Journal, Letters*, 585:L11–L14, March 2003.

[36] G. Ghirlanda, G. Ghisellini, and D. Lazzati. The Collimation-corrected Gamma-Ray Burst Energies Correlate with the Peak Energy of Their $\nu F_\nu$ Spectrum. *Astrophys. J.*, 616:331–338, November 2004.

[37] Gamma Ray Burst Mission . `http://swift.gsfc.nasa.gov/docs/swift/swiftsc.html`.

[38] S. E. Woosley and J. S. Bloom. The Supernova-Gamma Ray Burst Connection. *ARA&A*, 44:507–556, September 2006.

[39] Z. G. Dai, E. W. Liang, and D. Xu. Constraining $\Omega_M$ and Dark Energy with Gamma-Ray Bursts. *Astrophys. J. Lett.*, 612:L101–L104, September 2004.

[40] D. Lazzati et al. Long Gamma-Ray Bursts as standard candles. In S. S. Holt, N. Gehrels, and J. A. Nousek, editors, *AIP Conf. Proc. 838: Gamma-Ray Bursts in the Swift Era*, pages 513–521, May 2006.

[41] BATSE. http://www.batse.msfc.nasa.gov/batse/.

[42] R. Sari, T. Piran, and J. P. Halpern. Jets in Gamma-Ray Bursts. *Astrophys. J. Lett.*, 519:L17–L20, July 1999.

[43] D. Xu, Z. G. Dai, and E. W. Liang. Can Gamma-Ray Bursts Be Used to Measure Cosmology? A Further Analysis. *Astrophys. J.*, 633:603–610, November 2005.

[44] B. F. Gerke and G. Efstathiou. Probing quintessence: reconstruction and parameter estimation from supernovae. *Monthly Notices of the Royal Astronomical Society*, 335:33–43, September 2002.

[45] D. Kocevski and N. Butler. Gamma-Ray Burst Energetics in the Swift Era. *Astrophysical Journal*, 680:531–538, June 2008.

[46] L. Amati et al. Intrinsic spectra and energetics of BeppoSAX Gamma-Ray Bursts with known redshifts. *Astronomy and Astrophysics*, 390:81–89, July 2002.

[47] A. S. Friedman and J. S. Bloom. Toward a More Standardized Candle Using Gamma-Ray Burst Energetics and Spectra. *Astrophys. J.*, 627:1–25, July 2005.

[48] P. C. Gregory. *Bayesian Logical Data Analysis for the Physical Sciences: A Comparative Approach with 'Mathematica' Support*. Edited by P. C. Gregory. ISBN 0 521 84150 X (hardback); QA279.5.G74 2005 519.5'42 – dc22; 200445930. Published by Cambridge University Press, Cambridge, UK, 2005., 2005.

[49] W. H. Press. Numerical Recipes in C. *Science*, 259:1931–+, March 1993.

[50] D. J. C. MacKay. *Information Theory, Inference and Learning Algorithms*. ISBN 0521642981 . Cambridge, UK: Cambridge University Press, 2003.

[51] F. C. Speirits, M. A. Hendry, and A. Gonzalez. Gamma Ray Bursts: Cosmic Rulers for the High-Redshift Universe? *Phil. Trans. R. Soc. A*, 365:1395–1397, May 2007.

[52] C. D. Dermer. Statistics of cosmological gamma-ray bursts. *Physical Review Letters*, 68:1799–1802, March 1992.

[53] D. A. Frail et al. Beaming in Gamma-Ray Bursts: Evidence for a Standard Energy Reservoir. *Astrophysical Journal, Letters*, 562:L55–L58, November 2001.

[54] C. Firmani, G. Ghisellini, V. Avila-Reese, and G. Ghirlanda. Discovery of a tight correlation among the prompt emission properties of long gamma-ray bursts. *Mon. Not. R. Astron. Soc.*, 370:185–197, July 2006.

[55] C. Firmani, V. Avila-Reese, G. Ghisellini, and G. Ghirlanda. The Hubble diagram extended to z>>1: the gamma-ray properties of gamma-ray bursts confirm the $\Lambda$ cold dark matter model. *Mon. Not. R. Astron. Soc.*, pages L83+, September 2006.

[56] O. Bertolami and P. T. Silva. Gamma-ray bursts as dark energy-matter probes in the context of the generalized Chaplygin gas model. *Mon. Not. R. Astron. Soc.*, 365:1149–1159, February 2006.

[57] D. S. Sivia and J. Skilling. *Data Analysis: A Bayesian Tutorial*. ISBN 0 198 56831 2, 2006.

[58] D. W. Hogg. Distance Measures in Cosmology. *astro-ph/9905116*, 2000.

[59] D. E. Holz and E. V. Linder. Safety in Numbers: Gravitational Lensing Degradation of the Luminosity Distance-Redshift Relation. *Astrophysical Journal*, 631:678–688, October 2005.

[60] C. Clarkson, M. Cortês, and B. Bassett. Dynamical dark energy or simply cosmic curvature? *Journal of Cosmology and Astro-Particle Physics*, 8:11–+, August 2007.

[61] J. Virey et al. On the determination of curvature and dynamical Dark Energy. *ArXiv e-prints*, 802, February 2008.

[62] E. Troja, A. R. King, P. T. O'Brien, N. Lyons, and G. Cusumano. Different progenitors of short hard gamma-ray bursts. *Monthly Notices of the Royal Astronomical Society*, 385:L10–L14, March 2008.